A STUDY OF LOCALIZED FAILURE MODES IN BRITTLE MATERIALS

by

B B Burger

A thesis submitted in partial fulfilment of the requirements for the degree of Master of Science in Engineering

Department of Civil Engineering

University of Cape Town

September 1987

DECLARATION

This is to certify that the results, calculations and other work presented in this thesis are essentially my own work, and that no part of it has been submitted for a degree at any other university.

Signed by candidate

Signature Removed

B B Burger

September 1987

DEDICATION

I would like to dedicate this thesis to my parents for their encouragement and patience, as well as to my friends for their support.

ACKNOWLEDGEMENTS

I acknowledge, and greatly appreciate, the help of the following people :

Professor John Martin*, for providing me with both the opportunity and the motivation to do this work.

Dr Luis Resende**, for his enthusiastic and energetic guidance.

My AMRU colleagues for their willing assistance.

Val Atkinson and Shirley Breed for the typing of this document.

Cheryl Wright for the preparation of the figures.

The Foundation for Research and Development (FRD) for their financial assistance.

---

* Dean of Engineering

** Senior Research Officer, now at Hibbitt, Karlsson and Sorensen, Inc., Providence, Rhode Island.

ABSTRACT

Localization studies arise from the need to accurately model the behaviour of materials which exhibit instabilities due to strain softening or geometric effects. Localization in finite element modelling of brittle materials such as concrete and rock is a relatively unexplored area in computational mechanics, and this work applies current concepts to an isotropic damage model. The onset of localization is characterised by a bifurcation, where spatially uniform deformation is replaced by highly localized bands of large strain. Simple bifurcation analysis techniques are used, and are shown to extend the present predictive capability of the damage model and to indicate the direction of further refinement. Numerical studies of localization in concrete and norite are presented, together with boundary value problems of importance in mining applications. It is shown that qualitative agreement is obtained with experimental results.

TABLE OF CONTENTS

NOMENCLATURE

This is a list of the main symbols used in the main text of this thesis.

Special Symbols

$\cdot$	the differential with respect to a time scale
$\sim$	a vector or matrix
[ ]	a matrix
⟦ ⟧	a jump or discontinuity
| |	the absolute value of
T (superscript)	the transpose of a vector or matrix
-1 (superscript)	the inverse of a matrix
∇	the gradient of a vector
det	the determinant
Δ	the discriminant (determinant)
+ (superscript)	plus side of discontinuity
- (superscript)	minus side of discontinuity

Characters pertaining to the Localization Theory

(i) Lower case

a_0 to a_4	localization polynomial coefficients
f	localization condition
$\underset{\sim}{g}$	displacement vector within band
$\underset{\sim}{m}$, m_i	displacement direction vector within band

$\underset{\sim}{n}$, n_i — normal to localization band

$\underset{\sim}{s}$ — orientation of discontinuity plane

$\underset{\sim}{t}$, t_i — a traction

$\underset{\sim}{u}$, u_i — displacement field

$x = \tan \theta$ — orientation of $\underset{\sim}{n}$

(ii) Upper case

$\underset{\sim}{A}$ — localization matrix

$\underset{\sim}{D}$, $D_{ijk\ell}$ — tangent stiffness compliances

(iii) Greek

$\underset{\sim}{\epsilon}$ — strain tensor

λ_o — initial Lamé constant

μ_o — initial Lamé constant

ϕ — orientation of localized failure band with respect to σ_1

Ψ — nature of localized failure band

$\underset{\sim}{\sigma}$ — stress tensor

Σ — discontinuity plane

Characters pertaining to the Damage Theory

(i) Lower case

$a_1 - a_5, a_1^*$ — material constants

$a_{11}, a_{12}, a_{21}, a_{22}$ — constitutive coefficients

$b_1 - b_3$ — material constants

$c_1 - c_3$ — material constants

d_1 — material constant

e	effective shear strain
$\underset{\sim}{e}$	deviator strain vector
e_{ij}	deviator strain tensor
s	second invariant of deviator shear stress
$\underset{\sim}{s}$,	deviator stress vector
s_{ij}	deviator stress tensor
$\underset{\sim}{u}$	displacement vector

(ii) Upper case

A	shear damage term
B	hydrostatic tension damage term
$\underset{\sim}{B}$	strain-displacement matrix
$\underset{\sim}{C}$	transformation matrix
$\underset{\sim}{\hat{C}}$	transformation matrix
D	material constant
$\underset{\sim}{D}$	constitutive matrix
$\underset{\sim}{D}^{*}$	constitutive matrix
$D_{ikj\ell}$	elasticity tensor
E	Young's modulus
F	yield function
G	shear modulus
$\underset{\sim}{I}$	identity matrix
K	bulk modulus
W	material constant

(iii) Greek

γ_{ik}	engineering shear strain
δ_{ij}	Kronecker delta
$\underset{\sim}{\epsilon}$	strain vector

ϵ_{ij}	strain tensor
ϵ_{kk} , ϵ_v	volumetric strain
λ_s , λ_t	damage variables
λ_p	plastic multiplier
ν	Poisson's ratio
$\underset{\sim}{\sigma}$	stress vector
σ_{ij}	stress tensor
σ_{kk}	volumetric stress
σ_m	hydrostatic stress

CHAPTER 1

INTRODUCTION

Strain softening or geometric effects cause instabilities in the material behaviour of brittle materials such as rock or concrete. These are manifested in the form of highly localized zones of deformation and damage which result in shear bands or in fracture.

In a brittle material subjected to a load, distributed damage due to microcrack growth is the main inelastic mechanism. For some stress paths, and at a certain critical condition, the material instability causes a bifurcation and subsequent deformation is confined to localized bands of large strain. The onset of localization can be determined by using the bifurcation techniques proposed by Hill (1962). These were subsequently applied to dilatant materials by Rudnicki and Rice (1975), and it is this form which is used in this study.

In computational mechanics, continuous damage models have been used extensively to model brittle materials. However, subsequent to localization, discrete damage modes are present which are not described by continuous theories. These modes result in structural failure. The motivation for finite element localization studies thus lies in the need to extend the range of applicability of these models as well as to predict the mode of material failure. The localization

techniques used in this work are readily implemented in finite element codes and enable both the onset of localization and the resulting failure modes to be predicted.

As a basis for this work, a relatively simple isotropic damage model first proposed by Resende and Martin (1984a) and subsequently extended by Resende (1985,1987) was used. This model has already been shown to predict the stress-strain response of brittle materials with reliability, but its ability to predict localized failure still remains to be assessed.

The aim of this work is to test this aspect of the model, study the ability of the localization techniques in reproducing experimental observations, and to determine the extent to which the method extends the predictive range of continuous damage constitutive theories. For this purpose, a large range of numerical studies were performed. These ranged from simple "material point" models, to non-uniform triaxial models, and to large boundary value problems which have a practical application. The results of these studies are compared with some well known experimental observations.

The structure of this thesis is as follows. In chapter 2, a wide variety of available literature was surveyed, providing a comprehensive review of localization theory, damage mechanics, and of relevant experimental records. The localization condition and procedures for the computation of localized failure are described in chapter 3. This is followed by a review of the relevant damage model

and a description of the implementation of the localization theory into an existing finite element code. The numerical studies are presented and discussed in chapter 6. The thesis is then concluded with some comments and suggestions for future development.

CHAPTER 2

LITERATURE SURVEY

2.1 Introduction

Interest has increased steadily in recent years in the need to accurately model and assess the localized failure modes of materials in order to make realistic predictions about the response of complex structures.

Both analytical and finite element analyses of localization problems have been successfully performed for ductile materials, see for example Needleman and Tvergaard (1982). However, the study of localization in such brittle materials as concrete, rock and ceramics is a relatively unexplored area. For example, Rudnicki and Rice (1975) studied localization using a Drucker-Prager non-associated flow rule framework, and Ortiz (1986) investigated the failure modes of concrete.

Similarly, experimental studies of localized failure modes in brittle materials are sparse and often incomplete. Kupfer *et al* (1969) reported failure modes of concrete under biaxial stresses, Hallbauer *et al* (1973) investigated the microstructural changes and shear band formation occurring in quartzitic rock and, recently, a detailed study of localized failure modes in concrete was published by van Mier (1984, 1986).

The review of literature for this thesis covers firstly, the theoretical background to localization, secondly, experimental work on brittle materials and thirdly, constitutive modelling of brittle and strain-softening materials.

2.2 Analytical and Numerical Localization Studies

Observations of failure modes in solids show that when certain critical conditions are reached, failure often occurs in the form of highly localized deformations. In metals or ductile solids, these zones manifest themselves in the form of narrow shear bands (Anand and Spitzig (1980), Chang and Asaro (1980)), whilst in brittle materials both shear bands and splitting (fracture modes) can be observed (Kupfer *et al* (1969), van Mier (1986)). The orientation of the localized failure mode with respect to the state of stress is a material characteristic and is an outcome of the constitutive behaviour of the material (Ortiz *et al* (1986)).

These zones of localized failure can occur either during hardening, or when the material is softening (Rudnicki and Rice (1975)) and are normally a precursor to failure, hence the importance of understanding the nature of this phenomenon. Studies have shown that the onset of localization in brittle materials occurs at or after the maximum load (Hallbauer *et al* (1973), van Mier (1986)), and that for biaxial tests on sand, localization is only possible before the peak (Vardoulakis (1978,1980)). A characteristic of localization is that once deformations have localized, the strains inside the band become very large, loading continues within the band and unloading occurs elsewhere in the body.

It has been known for some time that localization in a deformed solid can be treated as an instability in the macroscopic constitutive description of the material (Hill (1962), Rudnicki and Rice (1975), Rice (1976), Needleman and Tvergaard (1982)). This instability can be treated as a bifurcation phenomenon in the sense that the initially homogeneously deformed material may undergo non-uniform deformation (in the form of a localized deformation band) under continuing conditions of equilibrium and continuing homogeneous deformations outside the localized zone (Rudnicki and Rice (1975)).

In a rate independent, thermally decoupled material, we can use the theoretical framework for analysing the onset of such localized failure modes given by Hill (1962). His work was an extension of the earlier work by Hadamard (1903) and Thomas (1961). Hill's criterion for bifurcation is now widely used by many authors eg. Rice (1976), Needleman and Tvergaard (1982), Ortiz (1986) and de Borst (1986). Rice (1976) has shown that this material bifurcation coincides with a loss of ellipticity of the governing incremental equilibrium equations.

Work in the field of localization has mainly been in plasticity and ductile solids (Needleman and Tvergaard (1982), Needleman and Rice (1978), Anand and Spitzig (1980), Tvergaard *et al* (1981) and Cristoffersen and Hutchinson (1979)). Here, the use of large deformation formulations are essential (although Anand and Spitzig only consider small strain theory) and it has been observed that the critical strain at which shear band bifurcation occurs is very sensitive to the material description. Experimental observations show

that for metals, localized failure modes invariably take the form of shear bands (Elam (1927)). In brittle materials however, localized failure modes ranging from splitting to pure shear type failure can occur. Sometimes, states of stress can exist such that a distributed type of failure is preferred to a highly localized one. In brittle materials, it has been noted that even though large strains can accumulate inside a failure band, the strains in the surrounding material remain largely unaffected and hence the assumption of small strains is valid (Ortiz *et al* (1986)).

Other important works in the field of localization are those by Rudnicki and Rice (1975) who formulated the localization condition for dilatant materials, de Borst (1986) who studied bifurcation phenomena in cohesive granular materials and Vardoulakis *et al* (1978) who used a semi-inverse method for the bifurcation problem of shear bands in sand masses.

The actual mechanisms of damage, fracture and shear band formation have been receiving much attention in recent studies. It is generally accepted that microcrack and macrocrack growth precede shear band formation, faulting or fracture failure. Research has shown that microcrack growth is distributed during early loading (Spooner and Dougill (1975), Dougill (1976), Ortiz (1985)). Only near or beyond certain critical conditions does localized damage prevail (Dougill (1976)) in the form of discrete failure planes. For these reasons, Ortiz (1986) and Ortiz *et al* (1986) adopted a distributed damage model for their computations. An interesting feature of the work by Ortiz *et al* (1986), is that once the localization conditions are satisfied, enhanced elements are used to fully capture the deformation state of the failure mode.

It must be noted that, in practice, a bifurcation point cannot be isolated since finite arithmetic is used. However, we can determine when this point has been passed (de Borst (1986)). Also, in the physical system (as opposed to the discretised system in finite element studies) non-uniformities can cause localization before the theoretical onset of the described instability.

2.3 Experimental Results

The current work has been devoted to the study of failure modes in concrete and norite (an igneous rock). This is mainly because of their general industrial importance and because of the availability of experimental results for these materials. Concrete is important as a building material, while norite is important to the mining industry.

Generally speaking, experimental data on failure modes for brittle materials is lacking. The data that is available is affected by the fact that failure modes are very sensitive to the experimental setup (Hegemier and Read (1984)). On the other hand experimental results for shear band formation in metals is freely available and ranges from material science research to finite element studies (Elam (1927), Chang and Asaro (1980), Anand and Spitzig (1980), Peirce *et al* (1981), Tvergaard *et al* (1981), Cristoffersen and Hutchinson (1979)).

Even though the post peak behaviour of concrete and other brittle materials has attracted attention (Bieniawski *et al* (1969), Read and Hegemier (1984), Willam *et al* (1984), Willam (1984), Sture and Ko (1978), Loland (1980)), the study of the failure modes has tended to

be incomplete. Some of the early research works on the failure mechanisms of rock were by Bieniawski (1967) and Bieniawski *et al* (1969). Kupfer *et al* (1969) gave the first description of failure modes in concrete under biaxial stresses. They also reported the orientation of the failure planes with respect to the principal applied stress. It has become the norm to report these orientations, even though there is some debate whether measured shear band inclinations are really material properties or rather properties of the complete structure formed by the loading platten and specimen (Kotsovos (1983) and van Mier (1986)). Nelissen (1972) also investigated the behaviour of concrete under various states of biaxial stress, and reports on some failure modes as well as the transition between shear and splitting failure modes. A very important contribution to the understanding of failure behaviour in rocks was made by Hallbauer *et al* (1973). This study included a very useful study on the progression of damage into a shear band in quartzitic rock specimens and shows photographic evidence of the failed quartzite. Sture and Ko (1978) conducted a study of strain-softening in geological materials, and have a graphical description of failure in a fractured rock specimen. Hegemier and Read (1984) did a similar study on concrete.

A major reference for this work was Stavropoulou's (1982) study on brittle rocks. Here, a detailed study of norite under triaxial stress at various confining pressures can be found. The corresponding failure modes are also reported. The most complete experimental work to date pertaining to failure modes was done by van Mier (1986), who studied localization in concrete under multiaxial states of stress. His work was used as the main source of concrete data for this study.

2.4 Damage Mechanics Constitutive Theories

To validate a constitutive model, researchers typically perform a strength fit and compare stress-strain predictions with experimental data. Until recently however, localized deformation or failure mode fits were seldom performed even though it is evident that this is a very important aspect of constitutive modelling. One of the purposes of this work is to attempt a localized failure mode fit using the damage mechanics theory of Resende and Martin (1984 a,b) and Resende (1987).

Past research has shown that the localization criteria are sensitive to features of the constitutive model (Rudnicki and Rice (1975), Rice (1976), Needleman and Rice (1978), Needleman and Tvergaard (1982), Ortiz (1986, 1987). In other words, the success of localization techniques in predicting localized failure modes depend on having a realistic constitutive model. Hence these techniques provide a stringent test for constitutive theories.

In the past, three basic approaches have been used to model the phenomena associated with brittle material fracturing or cracking.

(i) The discrete fracture mechanics approach describes the initiation and propagation of a single discontinuity.

(ii) The smeared crack approach models the propagation of distributed microdefects, usually by means of a strain-softening formulation.

(iii) Continuous damage mechanics describes the degradation of the inelastic compliances by means of a damage parameter and a damage evolution law.

Willam *et al* (1984) report that for tensile macrocracking, the fracture mechanics approach is recommended, whereas for shear type fracture problems damage mechanics is best. A number of authors have thus suggested the need for a combined approach (Janson and Hult (1977)) or a continuous transition between the two (Willam (1984)).

The smeared crack approach was used extensively by de Borst (1986) in his post-bifurcation and post-failure study of cohesive granular materials. For this study, he used Hill's (1962) bifurcation criteria.

Damage mechanics is a logical tool to use for localization studies since damage initially occurs in a general mode prior to the onset of localization. (Hallbauer *et al* (1973), Dougill (1976), Ortiz (1986)). Ortiz (1986) notes that distributed damage models are a good basis to study the onset and subsequent development of localized failure modes.

The main mechanisms underlying the inelastic behaviour of brittle materials are:

(i) Damage, in the form of nucleation and growth of micro-cracks, which is a progressive phenomena occurring at all stress levels (Spooner and Dougill (1975), Mazars and Lemaitre (1984), Ortiz (1985)).

(ii) Plastic flow, which is due to slip between the granular particles and the matrix material, or intercrystalline micro-cracking (Resende (1985), Lemaitre (1985), Ortiz (1985)).

Numerous continuous damage models of varying degrees of complexity have been proposed to model brittle materials for example Loland (1980), Krajcinovic and Fonseka (1981), Resende and Martin (1984), Resende (1987) and Ortiz (1985). For simplicity, some models assume the damage measure to be isotropic (Kracjinovic, Loland, Resende) because of evidence that microcracks are evenly distributed during early loading. On the other hand, Ortiz uses tensorial damage and mixture theory to account for the directionality of damage in later loading and to quantify the heterogeneous nature of concrete. Sometimes plasticity yield criteria are used to augment damage models; the models of Resende, Ortiz and Lemaitre (1985) are good examples.

The continuous damage model used in this work incorporates sufficient basic features to capture the behaviour of both rock and concrete materials (Resende (1986a, 1986b, 1987)). This isotropic model is rate independent and provides inelasticity via two basic mechanisms, namely, shear damage and hydrostatic tension damage. The total damage caused by these two mechanisms is measured by a scalar damage parameter. In addition, a plasticity yield surface is included to bound the model in the hydrostatic compression sense. A useful feature of the model is that it can easily be calibrated for a variety of brittle materials.

Van Mier (1986) notes that, in many problems, damage is not continuous and should be treated as anisotropic, and that concrete should be modelled as a heterogeneous material. It is, therefore, a prime interest of this study to determine the functionality of using relatively simple damage models for localization problems.

CHAPTER 3

LOCALIZATION THEORY

3.1 Introduction

In this chapter, the general theory of localization of inelastic deformations is reviewed. Attention is confined to small deformation theory and thermally decoupled, rate-independent material behaviour. These assumptions are consistent with the damage mechanics theory formulated by Resende and Martin (1984) and Resende (1985,1987), which is used in this work. These assumptions were also adopted by Ortiz (1986) and others who also used damage mechanics as a basis for their localization studies.

Whether we deal with damage or plasticity models, the general bifurcation theory is essentially the same and the basic principles follow the work of Hadamard (1903), Thomas (1961), Hill (1962), Rice (1976) and Ortiz (1986), to name but a few. This chapter first discusses the localization criteria, then deals with the computation of localized failure modes and concludes with some general matters of interest.

3.2 The Condition for Localization

We consider a rate-independent, homogeneous, homogeneously deformed solid, and subject it to quasi-static rates of deformation $\dot{\underset{\sim}{\epsilon}}$. The

question addressed is, when does a bifurcation into a localized failure mode occur such that subsequent deformations become discontinuous across a failure plane of unit normal $\underset{\sim}{n}$?

This is illustrated in Figure 3.1, where we see that when the localized deformation pattern is preferred, a bifurcation occurs, and the uniform deformation field changes to one which shows a jump across the shear band.

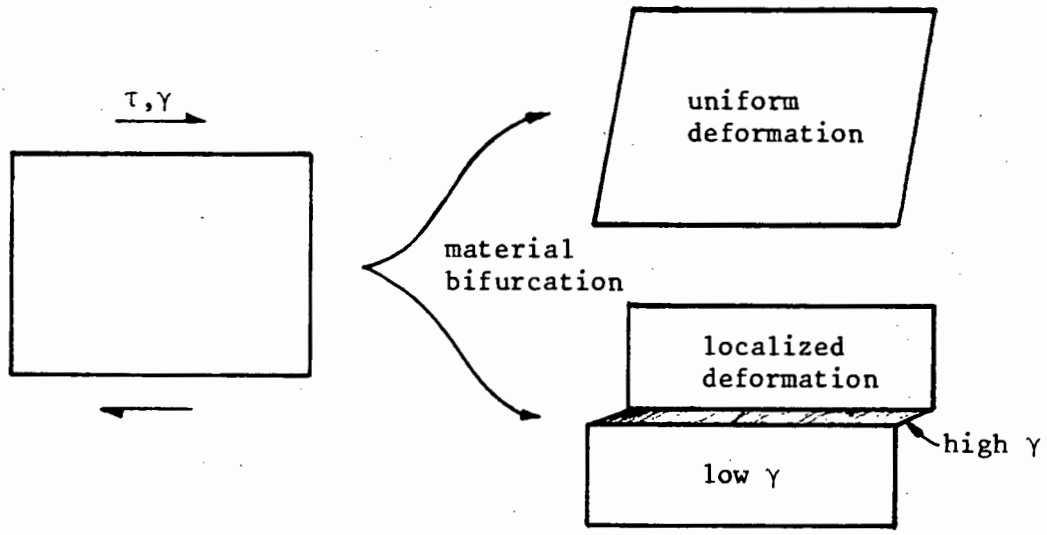

Figure 3.1 : Localization as a bifurcation phenomenon

For the complete characterization of localization, this jump must satisfy the field conditions, namely, -

(i) compatibility ;

(ii) equilibrium of tractions ;

(iii) constitutive laws.

Making use of the above three conditions, we can derive the condition for localization and determine the nature and description of the localized failure plane.

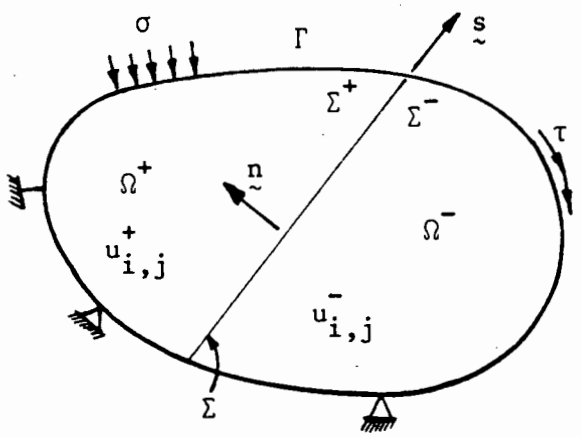

Figure 3.2 : Discontinuity plane description

3.2.1 Description of the discontinuity plane

Let $\underset{\sim}{u}$ be the displacement field in the solid. After the onset of localization (Figure 3.2), $\underset{\sim}{u}$ remains continuous over Σ, but $\nabla\underset{\sim}{u}$, the displacement gradients will exhibit a jump across the plane. The indicial notation is used to indicate i,j = 1,2,3 .

Using the notation,

$$\nabla\underset{\sim}{u} = \frac{\partial u_i}{\partial x_j} = u_{i,j}$$

and defining $u^+_{i,j}$ and $u^-_{i,j}$ to be on the plus and minus sides of Σ, the jump can be written as follows,

$$[\![u_{i,j}]\!] = u^+_{i,j} - u^-_{i,j} \neq 0 \quad . \tag{3.1}$$

Defining the vector $\underset{\sim}{s}$ as lying along the plane Σ, and using Maxwell's jump conditions to satisfy compatibility of the discontinuity plane,

$$u_i^+(\underset{\sim}{s}) = u_{i,j}^+ s_j$$
$$u_i^-(\underset{\sim}{s}) = u_{i,j}^- s_j \quad . \tag{3.2}$$

Since the displacement field remains continuous over Σ

$$u_i^+(\underset{\sim}{s}) - u_i^-(\underset{\sim}{s}) = 0 \quad , \tag{3.3}$$

and by taking derivatives,

$$(u_{i,j}^+ - u_{i,j}^-)\, s_j = 0 \quad , \tag{3.4}$$

or, by using the jump notation,

$$[\![u_{i,j}]\!]\, s_j = 0 \quad . \tag{3.5}$$

From the above, expanding in dyadic form, we can write

$$[\![u_{i,j}]\!] = g_i\, n_j \tag{3.6}$$

for some arbitrary vector $\underset{\sim}{g}$.

Now define $\underset{\sim}{m}$ as the unit vector along $\underset{\sim}{g}$.

$$\underset{\sim}{m} = \frac{\underset{\sim}{g}}{|g|} \quad , \quad \text{or} \quad m_i = \frac{g_i}{|g|} \quad .$$

Thus from (3.6),

$$[\![u_{i,j}]\!] = m_i\, n_j\, |g| \qquad \text{with} \qquad |m| = |n| = 1 \quad . \tag{3.7}$$

It is clear that vectors $\underset{\sim}{m}$ and $\underset{\sim}{n}$ completely define the nature and the orientation of the discontinuity plane as shown in Figure 3.3. The displacement field introduced by the localized mode can then be expressed in the form :-

$$u_i(x) = g_i\, n_j\, (x_j - x_j^o) \qquad \text{for} \qquad n_j\, (x_j - x_j^o) > 0 \quad \text{inside the shear band}$$

$$u_i(x) = 0 \qquad \text{for} \qquad n_j\, (x_j - x_j^o) \leq 0 \quad \text{elsewhere} \qquad (3.8)$$

where x_j^o is some point on the localized plane.

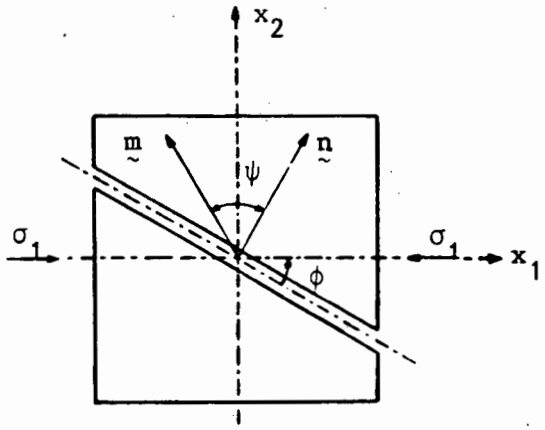

Figure 3.3 : Definition of the discontinuity plane

Using small strain theory, we can write the strain jump as

$$\begin{aligned} [\![\epsilon_{ij}]\!] &= \tfrac{1}{2}\,([\![u_{i,j}]\!] + [\![u_{j,i}]\!]) \\ &= \tfrac{1}{2}\,(g_i\, n_j + g_j\, n_i) \\ &= \tfrac{1}{2}\,|g|\,(m_i\, n_j + m_j\, n_i) \end{aligned} \qquad (3.9)$$

In reality, we find two planes of discontinuity pairing up to form a band. Theoretically, one plane of discontinuity is possible, but is unstable because, physically, we would have one side loading and the other side unloading. The case of the band therefore gives a more

stable situation where loading continues within the band while allowing the rest of the body to unload. Thus we get what can be called failure modes, where different modes are described by the behaviour of the two planes relative to each other.

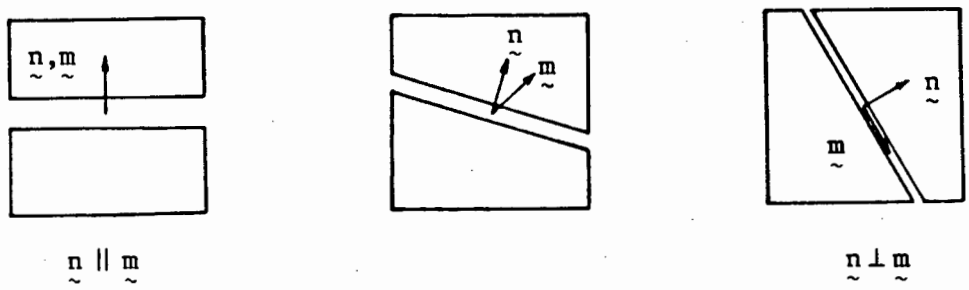

(a) splitting (b) mixed (c) shear

Figure 3.4 : Definition of failure modes

Noting the diagram of shear band and splitting modes in Figure 3.4, we realise that a combination of both modes is also possible where $\underset{\sim}{m}$ and $\underset{\sim}{n}$ are neither perpendicular nor parallel. These are called mixed failure modes. By taking the dot product, the angle between the vectors can be calculated

$$\begin{aligned} \underset{\sim}{m}\cdot\underset{\sim}{n} &= |m||n| \cos \varphi \\ &= \cos \varphi \\ \varphi &= \operatorname{acos}(m_i n_i) \quad . \end{aligned} \tag{3.10}$$

Thus φ can be used to characterize the type of failure mode. For $\varphi = 0^\circ$, $\underset{\sim}{m}$ and $\underset{\sim}{n}$ are coincident and we get a splitting fracture mode, and for $\varphi = 90^\circ$ a pure shear band is the failure mode. For concrete

and rock we find that the failure modes can range from pure shear modes to pure splitting failure.

3.2.2 Equilibrium of the failure plane

From the laws of equilibrium, the tractions $\underset{\sim}{t}$ must be continuous across the plane of discontinuity,

$$t_i^+ - t_i^- = 0 \quad ,$$

or in jump notation form,

$$[\![t_i]\!] = 0 \quad .$$

The traction can be written in terms of stress,

$$\underset{\sim}{t} = \underset{\sim}{\sigma}^T \underset{\sim}{n} \quad ,$$

and taking jumps across the discontinuity plane, we have

$$[\![t_j]\!] = [\![\sigma_{ij}]\!] n_i = 0 \quad . \tag{3.11}$$

3.2.3 Constitutive behaviour

In order to determine the onset of localization, we need to relate the compatibility conditions and the equilibrium of the failure plane to the material description. This can be done through the incremental stress-strain relations.

At the onset of localization, we still have $\underset{\sim}{u}$, $\underset{\sim}{\epsilon}$, $\underset{\sim}{\sigma}$ continuous throughout the body, but the deformation gradient and the stress and strain rates are not. Assuming the incremental relation,

$$\dot{\sigma}_{ij} = D_{ijk\ell}\,\dot{\epsilon}_{k\ell} \tag{3.12}$$

where $D_{ijk\ell}$ are the tangent stiffness compliances of the material which are updated at each increment, we can write

$$\dot{\sigma}^{+}_{ij} = D^{+}_{ijk\ell}\,\dot{\epsilon}^{+}_{k\ell}$$

$$\dot{\sigma}^{-}_{ij} = D^{-}_{ijk\ell}\,\dot{\epsilon}^{-}_{k\ell} \quad . \tag{3.13}$$

The same constitutive moduli are presumed to apply both inside and outside the band. This would not be the case if the band contained imperfections. Thus if Hill's (1962) equivalent linear solid is used, we can take

$$D^{+}_{ijk\ell} = D^{-}_{ijk\ell} = D_{ijk\ell}$$

since this gives the minimum bifurcation load. Defining the jump

$$[\![\dot{\sigma}_{ij}]\!] = \dot{\sigma}^{+}_{ij} - \dot{\sigma}^{-}_{ij} \quad ,$$

and using (3.13), we have

$$[\![\dot{\sigma}_{ij}]\!] = D_{ijk\ell}\,[\![\dot{\epsilon}_{k\ell}]\!] \quad . \tag{3.14}$$

From the equilibrium condition (3.11) and equation (3.14),

$$[\![\dot{\sigma}_{ij}]\!]n_i = D_{ijk\ell}\,[\![\dot{\epsilon}_{k\ell}]\!]n_i = 0 \quad . \tag{3.15}$$

Finally, from Maxwell's compatibility condition and relation (3.9),

$$|g|\, D_{ijk\ell}\, (m_k\, n_i) n_i = 0 \quad ,$$

$$(n_i\, D_{ijk\ell}\, n_\ell) m_k = 0 \quad . \tag{3.16}$$

This is the condition for localization. Localization will occur at the first point in the deformation history for which a non-trivial solution to equation (3.16) can be found. The unit vectors $\underset{\sim}{n}$ and $\underset{\sim}{m}$ can now be seen to fully define the failure mode.

Using Ortiz' notation, we introduce what is called the localization matrix $\underset{\sim}{A}(\underset{\sim}{n})$ which is defined by ,

$$A_{jk} = n_i\, D_{ijk\ell}\, n_\ell \quad . \tag{3.17}$$

Immediately it can be seen that the localization condition reduces to the familiar eigenproblem

$$A_{jk}\, m_k = 0 \quad ,$$

in matrix form

$$\underset{\sim}{A}\, \underset{\sim}{m} = \underset{\sim}{0} \quad . \tag{3.18}$$

In other words, for a bifurcation into a failure plane of orientation $\underset{\sim}{n}$ to occur, the determinant of the localization matrix $\underset{\sim}{A}(\underset{\sim}{n})$ must be zero. Thus we write

$$f(\underset{\sim}{n}) = \det(\underset{\sim}{A}(\underset{\sim}{n})) = 0 \quad , \qquad |n| = 1 \quad . \tag{3.19}$$

Therefore if, at some stage during the incremental analysis a unit vector $\underset{\sim}{n}$ can be found to satisfy the above equation, localization is possible. Once the localization condition has been satisfied, the "direction vector" $\underset{\sim}{m}$ can be determined as the eigenvector of equation (3.18).

The most important and fundamental aspect of the localization condition is that it is a pointwise condition. This has far-reaching implications in that the method is ideal for finite element implementation, since all the computations can be done at the element level.

3.3 Computation of Localized Failure Modes

The critical band (failure plane) orientation is the one for which equation (3.19) is satisfied at the earliest stage of the imposed deformation history. In a numerical analysis, the localization check must be performed at each increment of the solution procedure and at each gauss point of the finite element mesh. Here it is necessary to differentiate between the continuous and discrete cases. We are computing the bifurcation point for a discrete system. Thus it must be realised that normally we can only determine when we have passed this point ie. $f(\underset{\sim}{n}) \leq 0$.

It will be shown later that, if the material is elastic, $f(\underset{\sim}{n})$ is always positive and independent of $\underset{\sim}{n}$ and no localization is possible. As the incremental solution and the processes of deformation and

damage progress, f becomes a function of $\underset{\sim}{n}$ (eqn. 3.19) and develops minima. If the least value becomes zero or negative, it signals the onset of a localized failure mode. Thus at each stage of the solution procedure we have a constrained minimisation problem :

$$\text{minimise} \quad f(\underset{\sim}{n}) = \det (n_i \, D_{ijk\ell} \, n_\ell)$$

$$\text{subject to} \quad |n| = 1 \quad , \tag{3.20}$$

where $D_{ijk\ell}$ = current tangent modulus.

If $f_{min} = 0$ then localization has occurred and $\underset{\sim}{n}$ and $\underset{\sim}{m}$ can be computed

$f_{min} > 0$ no localization.

This problem can be solved by using a Lagrange multiplier method (Ortiz *et al* (1986)), in which a two-level iterative scheme is used. The first level is used to obtain a first approximation to $\underset{\sim}{n}$, following which, the second level uses a Newton-Raphson method to obtain an accurate solution.

3.3.1 The 2D localization problem

The Lagrange multiplier is suitable for general problems. For a 2D problem, the solution can be obtained by using a polynomial method (Ortiz *et al* (1986)), and since a 2D code is used for this work, this method is documented here.

In two dimensions, the localization matrix

$$A_{jk} = n_i D_{ijk\ell} n_\ell$$

where $\underset{\sim}{n} = (n_1, n_2, 0) = (\cos\theta, \sin\theta, 0)$, becomes

$$A_{jk} = \left[\begin{array}{l|l} n_1D_{1111}n_1 + n_1D_{1112}n_2 + & n_1D_{1121}n_1 + n_1D_{1122}n_2 + \\ n_2D_{2111}n_1 + n_2D_{2112}n_2 & n_2D_{2121}n_1 + n_2D_{2122}n_2 \\ \hline n_1D_{1211}n_1 + n_1D_{1212}n_2 + & n_1D_{1221}n_1 + n_1D_{1222}n_2 + \\ n_2D_{2211}n_1 + n_2D_{2212}n_2 & n_2D_{2221}n_1 + n_2D_{2222}n_2 \end{array}\right] \quad (3.21)$$

The localization condition $f(\underset{\sim}{n}) = \det(\underset{\sim}{A}(\underset{\sim}{n}))$ becomes

$$f = \det \underset{\sim}{A} = a_0n_1^4 + a_1n_1^3n_2 + a_2n_1^2n_2^2 + a_3n_1n_2^2 + a_4n_2^4$$

where

$$\begin{aligned} a_0 &= D_{1111}D_{1221} - D_{1211}D_{1121} \\ a_1 &= D_{1111}D_{1222} + D_{1111}D_{2221} - D_{1211}D_{1122} - D_{2211}D_{1121} \\ a_2 &= D_{1111}D_{2222} + D_{1112}D_{1222} + D_{1112}D_{2221} \\ &\quad - D_{1212}D_{1122} - D_{2211}D_{1122} - D_{2211}D_{2121} \\ a_3 &= D_{1112}D_{2222} + D_{2111}D_{2222} - D_{2212}D_{1122} - D_{2211}D_{2122} \\ a_4 &= D_{2112}D_{2222} - D_{2212}D_{2122} \quad . \end{aligned} \quad (3.22)$$

Following the NOSTRUM (1983) conventions, the stress and strain tensors are written in vector form as

$$\underset{\sim}{\sigma} = \begin{Bmatrix} \sigma_{11} \\ \sigma_{22} \\ \sigma_{12} \\ \sigma_{33} \end{Bmatrix} \quad \text{and} \quad \underset{\sim}{\epsilon} = \begin{Bmatrix} \epsilon_{11} \\ \epsilon_{22} \\ \gamma_{12} \\ \epsilon_{33} \end{Bmatrix} .$$

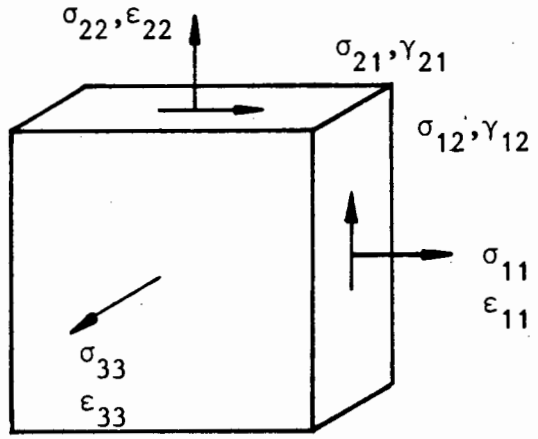

Figure 3.5 : Stress and strain conventions

The rate equations are written as

$$\dot{\sigma}_i = D_{ij} \dot{\epsilon}_j .$$

Comparing terms of the $\underset{\sim}{D}$ matrix above with

$$\dot{\sigma}_{ij} = D_{ijk\ell} \dot{\epsilon}_{k\ell} ,$$

and using $D_{ijk\ell} = D_{jik\ell} = D_{ij\ell k}$,

$$\sigma_{ij} = \sigma_{ji} ,$$

$$\epsilon_{ij} = \epsilon_{ji} ,$$

but with no symmetry , $D_{ijk\ell} \neq D_{k\ell ij}$

we find that

$$D_{ij} = \begin{bmatrix} D_{11} & D_{12} & D_{13} & D_{14} \\ D_{21} & D_{22} & D_{23} & D_{24} \\ D_{31} & D_{32} & D_{33} & D_{34} \\ D_{41} & D_{42} & D_{43} & D_{44} \end{bmatrix} \equiv \begin{bmatrix} D_{1111} & D_{1122} & D_{1112} & D_{1133} \\ D_{2211} & D_{2222} & D_{2212} & D_{2233} \\ D_{1211} & D_{1222} & D_{1212} & D_{1233} \\ D_{3311} & D_{3322} & D_{3312} & D_{3333} \end{bmatrix} = \begin{matrix} \text{non zero} \\ \text{terms of} \\ D_{ijk\ell} \end{matrix} . \qquad (3.23)$$

By writing

$$x = \tan\theta = \frac{\sin\theta}{\cos\theta} = \frac{n_2}{n_1} ,$$

and using the relation (3.23) for D_{ij} , the localization condition (3.22) becomes,

$$f = [\, a_0 + a_1 x + a_2 x^2 + a_3 x^3 + a_4 x^4 \,]\, n_1^4$$

$$f = 0 \quad \text{for localization} \quad .$$

This gives what we call the localization polynomial, where

$$f(x) = a_0 + a_1 x + a_2 x^2 + a_3 x^3 + a_4 x^4$$

$$a_0 = D_{11}D_{33} - D_{31}D_{13}$$

$$a_1 = D_{11}D_{32} + D_{11}D_{23} - D_{31}D_{12} - D_{21}D_{13}$$

$$a_2 = D_{11}D_{22} + D_{13}D_{32} + D_{31}D_{22} - D_{33}D_{12} - D_{21}D_{12} - D_{21}D_{33}$$

$$a_3 = D_{13}D_{22} + D_{31}D_{22} - D_{23}D_{12} - D_{21}D_{32}$$

$$a_4 = D_{33}D_{22} - D_{23}D_{32} \quad . \qquad (3.24)$$

The localization polynomial fully describes the present state of the material with respect to orientation and is positive everywhere prior to localization. If the polynomial becomes zero or negative for any x , we have localization. Some typical localization polynomials are shown in Figure 3.6, and need not necessarily be symmetrical. The situation in Figure 3.7i needs special consideration since the minima lie at $x = \tan\theta = \pm \infty$. The solution procedure thus sets up $f(x)$ for each gauss point and checks the minima which usually occur at $f'(x) = 0$.

$$f' = a_1 + 2a_2x + 3a_3x^2 + 4a_4x^3$$
$$= 0 \quad \text{for a local min/max} \quad .$$

The solution, $x = \tan\theta$ to this cubic equation can be obtained in closed form by using Cardan's Rule.

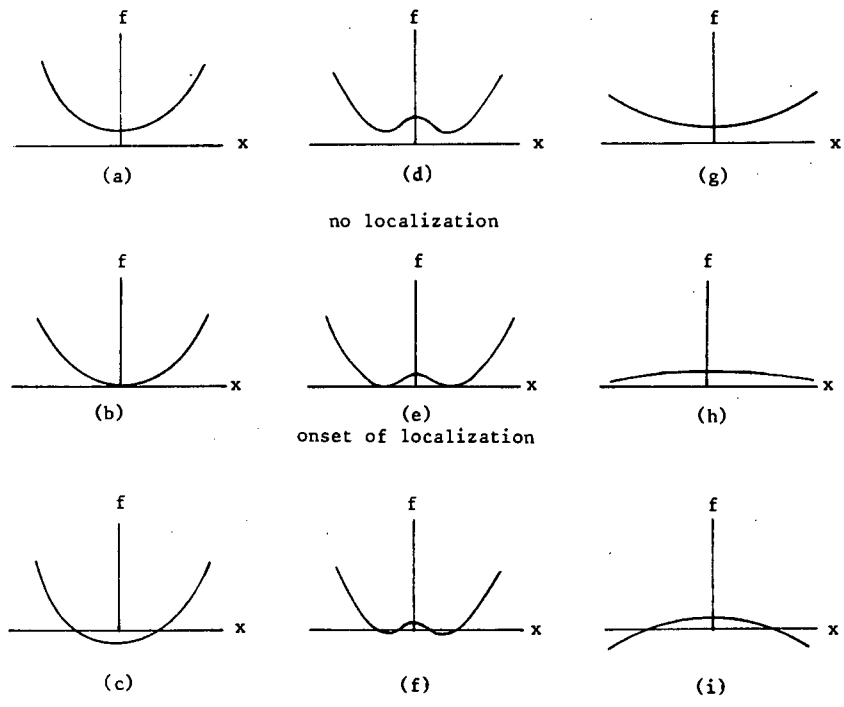

Figure 3.6 : Typical localization polynomials

3.3.2 Cardan's rule

The formulae for the roots of a cubic equation were first published by Cardan in the Ars Magna of 1545. The formula operates on a reduced cubic equation and the procedure is as follows. If

$$f = a_0 + a_1x + a_2x^2 + a_3x^3 + a_4x^4 \quad ,$$

localized failure occurs along orientations x , for which

$$f' = a_1 + 2a_2x + 3a_3x^2 + 4a_4 x^3 = 0 \quad .$$

Which can be rewritten as

$$g = x^3 + px^2 + qs + r = 0 \qquad (3.25)$$

where $p = \frac{3a_3}{4a_4}$, $q = \frac{a_2}{2a_4}$, $r = \frac{a_1}{4a_4}$.

The reduced cubic is found by substituting $x - \frac{1}{3}p$ into equation (3.25) giving

$$\hat{g} = x^3 + c_1x + c_2 = 0$$

where $c_1 = \frac{1}{3}(3q-p^2)$

$$c_2 = \frac{1}{27}(2p^3-9pq - 27r) \quad . \qquad (3.26)$$

The nature of the roots of g is given by

$$R = \frac{c_2^2}{4} + \frac{c_1^3}{27} \quad .$$

If : $R > 0$ 1 real root , 2 imaginary roots ;

$= 0$ 3 real, 2 equal roots ;

< 0 3 real, unequal roots. (3.27)

The roots of the reduced cubic are determined as follows:-

$$\text{If} \quad A = \left(\frac{-c_2}{2} + \sqrt{\frac{c_2^2}{4} + \frac{c_1^3}{27}} \right)^{1/3} = \left(\frac{-c_2}{2} + \sqrt{R} \right)^{1/3}$$

$$\text{and} \quad B = \left(\frac{-c_2}{2} - \sqrt{R} \right)^{1/3}$$

then the roots are (bearing (3.27) in mind)

$$\text{roots}_{1,2,3} = A + B \; ; \; \frac{-(A+B)}{2} + \sqrt{-3}\,\frac{(A+B)}{2} \; ; \; \frac{-(A+B)}{2} - \sqrt{-3}\,\frac{(A+B)}{2} \; . \quad (3.28)$$

And the roots of the cubic (stationary points of the quartic) are,

$$x_{1,2,3} = \text{roots}_{1,2,3} - \frac{p}{3} \quad , \quad (3.29)$$

which can be used to locate f_{min} and hence the orientation of the localized band :

$$\theta = \text{atan}(x)$$

$$n_1 = \cos(\theta)$$

$$n_2 = \sin(\theta) \quad . \quad (3.30)$$

3.3.3 Slip direction $\underset{\sim}{m}$

The slip direction $\underset{\sim}{m} = (m_1; m_2; 0)$ can be computed as the eigenvector of

$$\underset{\sim}{A}(\underset{\sim}{n})\underset{\sim}{m} = \underset{\sim}{0}$$

where $A_{jk} = n_i D_{ijk\ell} n_\ell$ is computed using the vector $\underset{\sim}{n}$ which satisfies the localization condition.

3.4 Localization Calculations in Elastic Solids

During the early stages of loading, brittle materials behave elastically. From the elastic material description and from previously obtained results, it can be shown that the localization condition is always positive.

In an elastic solid, the material compliances are given by

$$D^e_{ijk\ell} = \lambda_o \delta_{ij}\delta_{k\ell} + \mu_o(\delta_{ik}\,\delta_{j\ell} + \delta_{i\ell}\,\delta_{jk})$$

where λ_o, μ_o are the Lamé constants of the undeformed material.

δ_{ij} is the Kronecker delta.

Computing the localization condition for this elastic material using the previously derived equations (3.22) for a 2D solid,

$$f = \det \underset{\sim}{A} = a_0 n_1^4 + a_1 n_1^3 n_1 + a_2 n_1^2 n_2^2 + a_3 n_1 n_2^2 + a_4 n_2^4$$

where
$$a_0 = (\lambda_o + 2\mu_o)\mu_o$$
$$a_1 = 0$$
$$a_2 = 2(\lambda_o + 2\mu_o)\mu_o$$
$$a_3 = 0$$
$$a_4 = (\lambda_o + 2\mu_o)\mu_o \qquad (3.31)$$

$$\text{giving } f = (\lambda_o+2\mu_o)\mu_o[n_1^4 + 2n_1^2n_2^2 + n_2^4]$$

$$= (\lambda_o+2\mu_o)\mu_o$$

$$> 0 \quad \text{and independent of } \underset{\sim}{n} . \tag{3.32}$$

For a 3D solid, it can be shown that

$$f = (\lambda_o+2\mu_o)\mu_o^2 . \tag{3.33}$$

This general result shows that localization can never occur in an elastic solid.

3.5 Localization and the Loss of Ellipticity

It has been shown by Hill (1962) and Rice (1976) that the bifurcation of the material description coincides with the loss of ellipticity of the equations governing incremental equilibrium. This therefore presents us with an alternative perspective of the localization phenomenon. We can view the localization condition as either :

(i) $\det(\underset{\sim}{A}(\underset{\sim}{n})) = 0$ being met for some orientation $\underset{\sim}{n}$ as used in this work, or alternatively,

(ii) in a program of deformation, the onset of localization is first possible, when the equilibrium equations lose their ellipticity (Hill (1962)).

It can be shown that the established condition is equivalent to the loss of ellipticity. This is done here for a general second order partial differential equation (pde), Ortiz (1987). Let the pde be of the form

$$a_{ij}\phi'' + b_i\phi' + c\phi = 0 , \quad i,j = 1,2$$

where $\phi'' = \dfrac{\partial^2 \phi}{\partial x_i \partial x_i}$

$$\phi' = \frac{\partial \phi}{\partial x_i} \quad . \tag{3.34}$$

The discriminant (determinant) of $\underset{\sim}{a}$ is

$$\Delta = a_{11}a_{22} - a_{12}^2 \quad . \tag{3.35}$$

Depending on the sign of the discriminant, the character of the pde will vary :

(i) $\Delta > 0$ elliptic ;

(ii) $\Delta = 0$ parabolic ;

(iii) $\Delta < 0$ hyperbolic. (3.36)

From equations (3.35) and (3.21), it can be shown that

$$\Delta = \det(n_i D_{ijk\ell} n_\ell) \quad ,$$

and that prior to localization,

$$\Delta > 0 \quad . \tag{3.37}$$

Hence the governing equations are elliptic. However, it can also be seen that

$$\Delta \equiv f(\underset{\sim}{n}) \quad ,$$

the localization condition.

And if $f = 0$ we have localization, and from (3.36), the governing equations lose their ellipticity.

CHAPTER 4

DAMAGE MECHANICS CONSTITUTIVE MODEL

4.1 Introduction

This chapter serves primarily as a review of the damage mechanics constitutive theory proposed by Resende and Martin (1984a,b, 1987), Resende (1985, 1986b, 1987), for brittle materials such as rock and concrete. This model provides the basis for the localization studies in this work and thus it is very important to understand the salient features of the model before analysing the numerical results.

The reasons for using this damage model are, firstly, damage mechanics has been shown to provide a good basis for localization studies in brittle materials (Ortiz (1986)) and, secondly, the model has been validated by means of a strength fit (Resende (1985, 1986)), and a failure mode fit is required to complete this validation.

The behaviour of rate-independent brittle materials under loading has been the subject of interest to many researchers for some time (Bieniawski (1967), Bieniawski *et al* (1969), Kupfer *et al* (1969), Nelissen (1972), Hallbauer *et al* (1973), Spooner and Dougill (1975), Dougill (1976), Sture and Ko (1978), Stavropoulou (1982), Willam (1984), and van Mier (1986)). The essential features of brittle material behaviour have been summarised in Resende and Martin (1984) and Resende (1985) and are shown here in Figure 4.1. Spooner and Dougill (1975) show that concrete and rock exhibit similar behaviour,

the major feature being that these materials are substantially more brittle in tension than in compression. Resende's damage theory attempts to capture these features, the material inelasticity in this model is provided by two damage mechanisms, namely tensile cracking and shear induced cracking. The progressive fracturing ideas of Dougill form the basis of the model which uses an internal damage variable, which, together with damage evolution laws, define the rate of material degradation. The evolution laws contain the essential features to describe the material behaviour, and relate the rate of damage to the stress and strain history of the material. Figure 4.1 shows some features of brittle material behaviour.

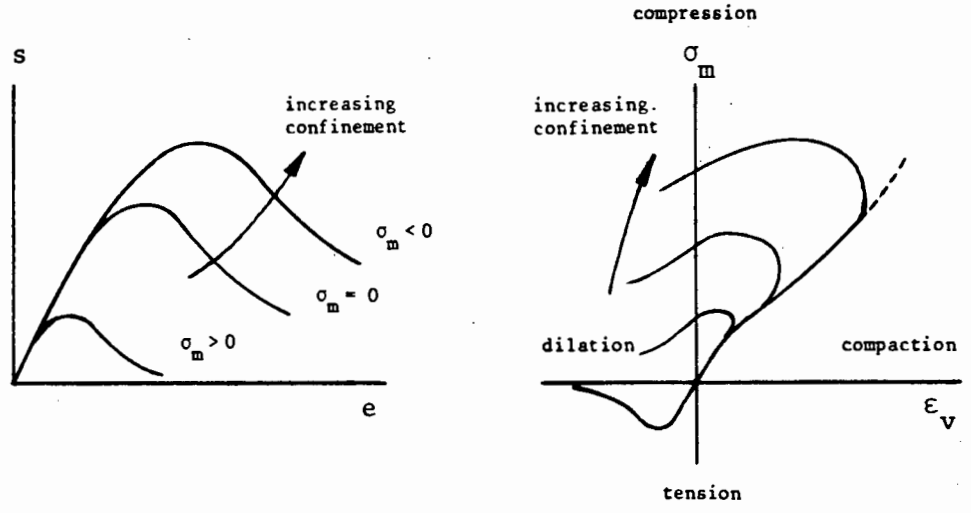

Figure 4.1 : Typical brittle material behaviour

It must be noted that microcracking (damage) is assumed to be continuous and not discrete. The measure of damage is assumed to be scalar and hence the model is isotropic, since the damage measure lacks directionality. In reality, these assumptions are only valid up to the onset of localization.

The chapter first deals with the derivation of the damage equations and evolution laws using the deviator and volumetric invariant relations. The equations are then generalised to component form. Finally, the calibration of the model parameters is described.

4.2 Constitutive Equations

The constitutive equations are best developed and demonstrated by using the invariant form, and then using the stress, stress-invariant relations to obtain the equations in a general form for continuum problems.

Define the stress invariants following Resende and Martin (1985) as

$$\sigma_m = \frac{1}{3}\sigma_{kk} \quad ,$$
$$\dot{\sigma}_m = \frac{1}{3}\dot{\sigma}_{kk} \quad ,$$

$$s = \left(\frac{1}{2} s_{ij}\, s_{ij}\right)^{1/2} \quad ,$$
$$\dot{s} = \frac{1}{2s} s_{ij}\, \dot{s}_{ij} \quad ,$$

where

$$s_{ij} = \sigma_{ij} - \frac{1}{3}\sigma_{kk}\,\delta_{ij} \quad ,$$
$$\dot{s}_{ij} = \dot{\sigma}_{ij} - \frac{1}{3}\dot{\sigma}_{kk}\,\delta_{ij} \quad . \qquad (4.1a)$$

Note that σ_{ij} and ϵ_{ij} are the stress and strain tensors, δ_{ij} is the Kronecker delta and the $\bullet$ represents a rate.

Define the strain invariants and conjugate strain invariant rates as

$$\epsilon_v = \epsilon_{kk} \quad ,$$
$$\dot{\epsilon}_v = \dot{\epsilon}_{kk} \quad ,$$

$$\dot{e} = \frac{1}{s} s_{ij} \dot{e}_{ij} \quad ,$$

where $\dot{e}_{ij} = \dot{\epsilon}_{ij} - \frac{1}{3} \dot{\epsilon}_{kk} \delta_{ij}$,

$$\epsilon_v = \int \dot{\epsilon}_v \, dt \quad ,$$

$$e = \int \dot{e} \, dt \quad . \tag{4.1b}$$

Now define the measure of damage λ ,

$$\lambda = \lambda_s + \lambda_t \tag{4.2}$$

where λ_s = damage caused by shear

λ_t = damage caused by hydrostatic tension

and $0 \leq \lambda \leq 1$.

Damage is therefore a scalar quantity and has no directionality; however, the response of the material is in general non-isotropic. As will be seen later in equations (4.3) and (4.25), when $\lambda = 0$ the material is in its virgin state, and when $\lambda = 1$, it is fully damaged. The nature of λ_s and λ_t will be discussed later.

4.2.1 Deviator relations in compression (defined as $\sigma_m \leq 0$) .

Under compressive conditions, a shear damage mechanism is postulated, representing the breaking of internal bonds as the material is sheared. The effective shear stress, shear strain invariant, elastic relationship, in total terms, is:

$$s = G_o(1-\lambda)e^e \qquad (4.3)$$

where G_o = initial shear modulus

e^e = elastic component of shear strain invariant.

In rate form the total shear strain invariant $\dot{e}$, is assumed to be the sum of elastic and damage shear strain invariants

$$\dot{e} = \dot{e}^e + \dot{e}^d \quad , \qquad (4.4)$$

where $\dot{e}^d$ = damage shear strain rate, which is directly dependent on the amount and the rate of shear damage.

This is defined as

$$\dot{e}^d = d_1 \lambda_s \dot{\lambda}_s \quad , \qquad (4.5)$$

where d_1 = permanent shear strain constant (a material parameter).

For a displacement based finite element formulation, the stress rates should be in terms of total strain rates. Hence from equations (4.3), (4.4) and (4.5), and defining unloading as any path in which no additional damage occurs ($\dot{\lambda} = 0$),

$$\dot{s} = \begin{cases} G_o(1-\lambda)\dot{e} - G_o(1-\lambda)d_1\lambda_s\dot{\lambda}_s - G_o e^{e}\dot{\lambda} & \text{for loading } (\dot{\lambda} > 0) \\ G_o(1-\lambda)\dot{e} & \text{for unloading } (\dot{\lambda} = 0) \end{cases} \tag{4.6}$$

Under these conditions, only the $\dot{\lambda}_s$ mechanism is active.

4.2.2 Deviator relations in tension (defined as $\sigma_m > 0$)

Under tensile conditions, it is assumed that the same shear damage mechanism can also be active, hence equation (4.6) holds. However, for tensile paths, $\lambda_t >> \lambda_s$, hence from definition (4.5), $\dot{e}^d$ is assumed zero, giving

$$\dot{s} = \begin{cases} G_o(1-\lambda)\dot{e} - G_o e^{e}\dot{\lambda} & \text{for loading } (\dot{\lambda} > 0) \\ G_o(1-\lambda)\dot{e} & \text{for unloading } (\dot{\lambda} = 0) \end{cases} \tag{4.7}$$

4.2.3 Volumetric relations in compression ($\sigma_m \leq 0$)

When loaded and subsequently unloaded in hydrostatic compression, concrete shows permanent strains. To account for the behaviour of concrete, Resende (1985) uses a plasticity yield surface to bound the model along the hydrostatic compression axis (see Figure 4.2). Stavropoulou (1982) suggests that there are no such permanent strains in rock. The disparity between concrete and rock behaviour is then taken care of in the calibration for rock, by deactivating the cap (Resende (1986a,b)).

The volumetric relations are introduced by defining the total volumetric strain rate $\dot{\epsilon}_v$;

$$\begin{aligned}\dot{\epsilon}_v &= \dot{\epsilon}_v^t + \dot{\epsilon}_v^d \\ &= \dot{\epsilon}_v^e + \dot{\epsilon}_v^s + \dot{\epsilon}_v^d\end{aligned} \tag{4.8}$$

where $\dot{\epsilon}_v^t$ = volumetric strain rate due to the hydrostatic compression mechanism;

$\dot{\epsilon}_v^e$ = elastic volume strain rate;

$\dot{\epsilon}_v^s$ = plastic volume strain rate;

$\dot{\epsilon}_v^d$ = volumetric strain rate due to the shear damage mechanism.

Note that as in classical elasto-plasticity, it is assumed that $\dot{\epsilon}_v^t$ is composed of an elastic and plastic contribution.

The elastic hydrostatic stress, volumetric strain relation is given by

$$\dot{\sigma}_m = K_o \dot{\epsilon}_v^e \quad , \tag{4.9}$$

where K_o = initial elastic bulk modulus.

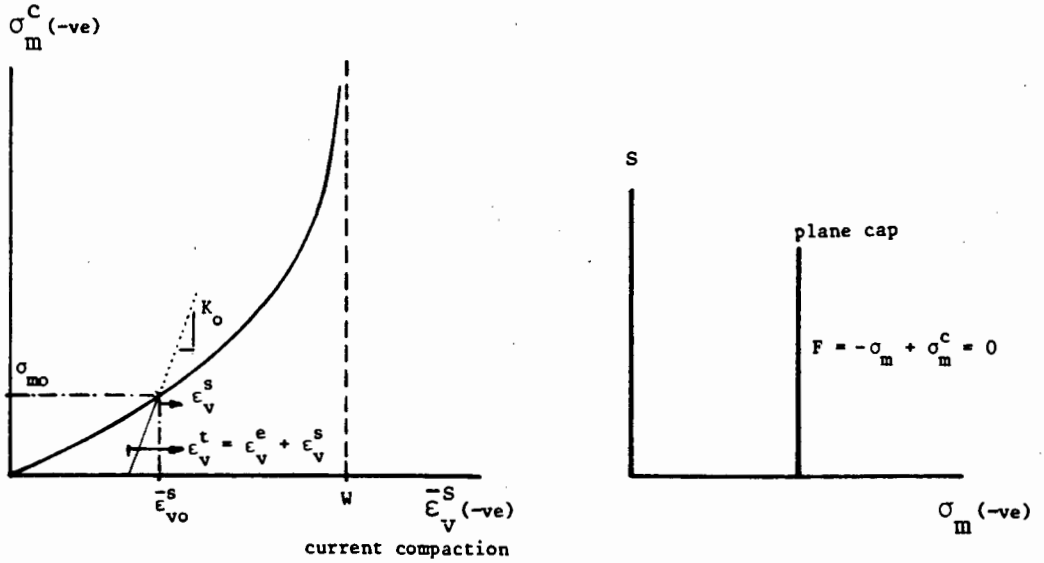

(a) nonlinear hardening rule (b) cap yield surface

Figure 4.2 : Plasticity yield surface and nonlinear hardening rule

The model uses a plane yield surface, and this is defined as

$$F = -\sigma_m + \sigma_m^c = 0 \quad . \tag{4.10}$$

The parameter σ_m^c is a hardening parameter and depends on the plastic volume strain ϵ_v^s which has occurred since initial loading. By defining the current degree of compaction $\bar{\epsilon}_v^s$, as follows,

$$\bar{\epsilon}_v^s = \bar{\epsilon}_{vo}^s + \epsilon_v^s \tag{4.11}$$

$$= W\left(1-e^{D\sigma_m^c}\right) \quad , \tag{4.12}$$

where $\bar{\epsilon}_{vo}^s$ = initial degree of compaction;

$\bar{\epsilon}_v^s$ = current degree of compaction

ϵ_v^s = plastic volume strain;

W,D = constants;

the strengthening of the material under increasing hydrostatic pressure can be accounted for. The cap can translate along the compression side of the σ_m axis, but only in the negative σ_m direction.

Inverting (4.12) and substituting in equation (4.10),

$$F = -\sigma_m + \frac{1}{D}\,\ell n\left(a - \frac{\epsilon_v^s}{W}\right) \tag{4.13}$$

where $a = \left(1 - \frac{\bar{\epsilon}_{vo}^s}{W}\right)$.

Using the normality rule, the plastic volume strain rate is given by

$$\dot{\epsilon}_v^s = \dot{\lambda}_p \frac{\partial F}{\partial \sigma_m}$$
$$= -\dot{\lambda}_p \quad , \tag{4.14}$$

where $\dot{\lambda}_p$ is a plastic multiplier and $\dot{\lambda}_p \geq 0$.

Note that $\dot{\lambda}_p$ is not a damage measure.

Now using equations (4.8) and (4.14),

$$\dot{\epsilon}_v^e = \dot{\epsilon}_v^t - \dot{\epsilon}_v^s$$
$$= \dot{\epsilon}_v^t + \dot{\lambda}_p \quad , \tag{4.15}$$

yielding,

$$\dot{\sigma}_m = K_o(\dot{\epsilon}_v^t + \dot{\lambda}_p) \quad . \tag{4.16}$$

Now using the classical plasticity condition for loading ($\dot{F} = 0$), equation (4.13) becomes

$$-\dot{\sigma}_m - H\,\dot{\epsilon}_v^s = 0$$

$$\text{where } H = \frac{1}{WD\left(a - \frac{\epsilon_v^2}{w}\right)} \quad ; \tag{4.17}$$

and by using (4.14) in (4.17)

$$-\dot{\sigma}_m + H\,\dot{\lambda}_p = 0 \quad . \tag{4.18}$$

Substituting (4.16) into (4.18) gives

$$\dot{\lambda}_p = \frac{-K_o \dot{\epsilon}_v^t}{K_o - H} \tag{4.19}$$

Now $(K_o - H)$ is always positive, hence :

(i) for loading $-K_o \dot{\epsilon}_v^t > 0$ and $\dot{\lambda}_p > 0$,

(ii) for unloading $-K_o \dot{\epsilon}_v^t \leq 0$ and $\dot{\lambda}_p = 0$. (4.20)

For $-K_o \dot{\epsilon}_v^t < 0$, the plastic multiplier, $\dot{\lambda}_p$, is set equal to zero, since physically $\dot{\lambda}_p < 0$ is not possible.

From the above, and using equations (4.16) and (4.19), the constitutive equations for compressive loadings parallel to the hydrostatic axis are

$$\dot{\sigma}_m = \begin{cases} \left(K_o - \dfrac{K_o^2}{K_o - H}\right) \dot{\epsilon}_v^t & \text{for loading , } \dot{\lambda}_p > 0 \\ K_o \dot{\epsilon}_v^t & \text{for unloading, } \dot{\lambda}_p = 0 \ . \end{cases} \tag{4.21}$$

These equations are augmented by introducing a coupling between the shear damage λ_s and the volumetric deformation due to shear damage, ϵ_v^d , given by the following law,

$$\dot{\epsilon}_v^d = (c_1 + c_2 e)\, \dot{\lambda}_s + c_3\, \lambda_s \dot{e} \tag{4.22}$$

where c_1 , c_2 , c_3 are material parameters.

From equations (4.8) and (4.22)

$$\begin{aligned}\dot{\epsilon}_v^t &= \dot{\epsilon}_v - \dot{\epsilon}_v^d \\ &= \dot{\epsilon}_v - (c_1+c_2 e)\dot{\lambda}_s - c_3\lambda_s\dot{e} \quad ,\end{aligned} \tag{4.23}$$

which can be substituted into equation (4.21) to complete the constitutive description for compressive loadings.

In summary, there are four modes of behaviour in compression :-

(i) $\dot{\lambda}_s > 0$ shear damage active

$\dot{\lambda}_p > 0$ volumetric yielding active

$$\dot{\sigma}_m = \left(K_o - \frac{K_o^2}{K_o - H}\right)\left(\dot{\epsilon}_v - (c_1+c_2 e)\dot{\lambda}_s - c_3\lambda_s\dot{e}\right) \tag{4.24a}$$

(ii) $\dot{\lambda}_s = 0$

$\dot{\lambda}_p > 0$ volumetric yielding active

$$\dot{\sigma}_m = \left(K_o - \frac{K_o^2}{K_o - H}\right)\left(\dot{\epsilon}_v - c_3\lambda_s\dot{e}\right) \tag{4.24b}$$

(iii) $\dot{\lambda}_s > 0$ shear damage active

$\dot{\lambda}_p = 0$

$$\dot{\sigma}_m = K_o\left(\dot{\epsilon}_v - (c_1+c_2\dot{e})\dot{\lambda}_s - c_3\lambda_s\dot{e}\right) \tag{4.24c}$$

(iv) $\left.\begin{aligned}\dot{\lambda}_s &= 0\\ \dot{\lambda}_p &= 0\end{aligned}\right\}$ elastic behaviour

$$\dot{\sigma}_m = K_o(\dot{\epsilon}_v - c_3\lambda_s\dot{e}) \qquad (4.24d)$$

4.2.4 Volumetric relations in tension ($\sigma_m > 0$)

When brittle materials are loaded under tension, the material behaviour is substantially different to the compression case, the material particles separate resulting in cracking. To account for this behaviour, a hydrostatic tension damage mechanism is used. The elastic relationship between hydrostatic stress and elastic volume strain is

$$\sigma_m = K_o(1-\lambda)\epsilon_v^e \qquad (4.25)$$

where K_o = initial elastic bulk modulus;

ϵ_v^e = elastic volume strain;

and $0 \leq \lambda \leq 1$.

The rate form of equation (4.25) is

$$\dot{\sigma}_m = \begin{cases} K_o(1-\lambda)\dot{\epsilon}_v^e - K_o\,\epsilon_v^e\,\dot{\lambda} & \text{for loading , } \dot{\lambda} > 0 \\ K_o(1-\lambda)\dot{\epsilon}_v^e & \text{for unloading, } \dot{\lambda} = 0 \end{cases} \qquad (4.26)$$

Using equations (4.8) and (4.23),

$$\dot{\sigma}_m = \begin{cases} K_o(1-\lambda)(\dot{\epsilon}_v - (c_1+c_2 e)\dot{\lambda}_s - c_3\lambda_s\dot{e}) - K_o\,\epsilon_v^e\,\dot{\lambda} & , \quad \dot{\lambda} > 0 \\ \\ K_o(1-\lambda)(\dot{\epsilon}_v - c_3\lambda_s\dot{e}) & , \quad \dot{\lambda} = 0 \end{cases} \tag{4.27}$$

Under the above conditions, $\dot{\lambda}$ would be dependent mainly upon $\dot{\lambda}_t$.

4.2.5 Damage evolution equations

The deviator and volumetric relations can now be merged to give the damage constitutive equations and an associated set of constraints for each possible mode of behaviour.

The damage equation in rate form is

$$\dot{\lambda} = \dot{\lambda}_s + \dot{\lambda}_t$$

$$= A(e,\sigma_m)\dot{e} + B(\epsilon_v)\dot{\epsilon}_v \quad , \tag{4.28a}$$

where $\dot{\lambda}_s = A(e,\sigma_m)\dot{e}$ = shear damage evolution rate, $A(e,\sigma_m)$ contains material parameters

$\dot{\lambda}_t = B(\epsilon_v)\dot{\epsilon}_v$ = hydrostatic tension damage evolution rate, $B(\epsilon_v)$ contains material parameters.

The damage mechanisms that are active at any instant depend on the constraints and states of stress defined in the theory.

Mode	Stress State	Conditions	Description
1	compression $\sigma_m \leqq 0$	$\dot{\lambda}_p = 0$ no volumetric yielding $\dot{\lambda} = 0$ unloading	elastic behaviour
2	compression $\sigma_m \leqq 0$	$\dot{\lambda}_p > 0$ volumetric yielding $\dot{\lambda} = 0$ unloading	elastic-plastic behaviour
3	compression $\sigma_m \leqq 0$	$\dot{\lambda}_p = 0$ no volumetric yielding $\dot{\lambda} = \lambda_s$ shear damage active	shear damage behaviour
4	compression $\sigma_m \leqq 0$	$\dot{\lambda}_p > 0$ volumetric yielding $\dot{\lambda} = \lambda_s$ shear damage active	shear damage/ elastic-plastic behaviour
5	tension $\sigma_m > 0$	$\dot{\lambda} = 0$ unloading	elastic behaviour
6	tension $\sigma_m > 0$	$\dot{\lambda} = \dot{\lambda}_s + \dot{\lambda}_t$ shear and hydrostatic damage active	shear and hydrostatic tension damage behaviour
7	tension $\sigma_m > 0$	$\dot{\lambda} = \dot{\lambda}_s$ shear damage active	shear damage behaviour

Table 4.1 : Summary of damage model behaviour

(i) Compression ($\sigma_m \leq 0$) and tension ($\sigma_m > 0$) , when $\dot{\epsilon}_v < 0$.

The only active damage mechanism can be shear damage, λ_s , thus $\dot{\lambda}_t = 0$ and,

$$\dot{\lambda} = \begin{cases} A\dot{e} & \text{for } \lambda_s = \lambda_{smax} \ , \quad \dot{e} > 0 \\ 0 & \text{otherwise} \ . \end{cases} \tag{4.28b}$$

In addition to the above mechanism, the hydrostatic plasticity loading conditions have to be taken into account for compressive stress states ($\sigma_m \leq 0$) . This depends on the sign of the plastic multiplier, $\dot{\lambda}_p$. If $\dot{\lambda}_p > 0$, we have hardening.

(ii) Tension ($\sigma_m > 0$) , when $\dot{\epsilon}_v \geq 0$ and $\dot{e} > 0$.

Here, the shear and/or hydrostatic tension damage mechanisms can be active, depending on whether $\lambda_s = \lambda_{smax}$, $\lambda_t = \lambda_{tmax}$.

$$\dot{\lambda} = \begin{cases} A\dot{e} + B\dot{\epsilon}_v & \text{for } \lambda_s = \lambda_{smax} \ , \ \lambda_t = \lambda_{tmax} \\ A\dot{e} & \lambda_s = \lambda_{smax} \ , \ \lambda_t < \lambda_{tmax} \\ B\dot{\epsilon}_v & \lambda_t = \lambda_{tmax} \ , \ \lambda_t = \lambda_{tmax} \end{cases} \tag{4.28c}$$

(iii) Tension ($\sigma_m > 0$) , when $\dot{\epsilon} \geq 0$ and $\dot{e} \leq 0$.

In this case, further damage can only occur if $\dot{\lambda}$ is positive and $\lambda_t = \lambda_{tmax}$. Thus $\dot{\lambda}_s$ can be negative.

$$\dot{\lambda} = \begin{cases} A\dot{e} + B\dot{\epsilon}_v & \text{for } \lambda_t = \lambda_{tmax}, \quad \dot{\lambda} = \dot{\lambda}_s + \dot{\lambda}_t > 0 \\ 0 & \text{otherwise.} \end{cases} \tag{4.28d}$$

These seven modes are summarised in Table 4.1.

4.2.6 Damage constitutive equations

The above mechanisms relate to the behaviour modes in compression and tension which were described earlier. The invariant damage constitutive equations can be represented in matrix form as

$$\begin{Bmatrix} \dot{s} \\ \dot{\sigma}_m \end{Bmatrix} = \begin{bmatrix} (G-a_{11}) & -a_{12} \\ -a_{21} & (K-a_{22}) \end{bmatrix} \begin{Bmatrix} \dot{e} \\ \dot{\epsilon}_v \end{Bmatrix} \tag{4.29}$$

where $G = G_o(1-\lambda)$ for compression or tension;

$$K = \begin{cases} K_o & \text{for compression;} \\ K_o(1-\lambda) & \text{for tension.} \end{cases}$$

Here,

G, K represents the current elastic moduli and are updated during the loading history;

and

a_{ij} are related to the damage of the material and depend on the current state and mode of behaviour. The values for the coefficients are given in Table 4.2 .

Mode of behaviour	a_{11}	a_{12}	a_{21}	a_{22}	Conditions
1	0	0	$K_0 c_3 \lambda_s$	0	$\sigma_m \leq 0,\ \dot{\lambda} = 0,\ \dot{\lambda}_p = 0$
2	0	0	$\left(K_0 - \frac{K_0^2}{K_0 - H}\right) c_3 \lambda_s$	$\frac{K_0^2}{K_0 - H}$	$\sigma_m \leq 0,\ \dot{\lambda} = 0,\ \dot{\lambda}_p > 0$
3	$G_0(1-\lambda) d_1 \lambda_s A + G_0 e^c A$	0	$K_0[(c_1 + c_2 e)A + c_3 \lambda_s]$	0	$\sigma_m \leq 0,\ \dot{\lambda} = \dot{\lambda}_s = A\dot{e},\ \dot{\lambda}_p = 0$
4	$G_0(1-\lambda) d_1 \lambda_s A + G_0 e^c A$	0	$\left(K_0 - \frac{K_0^2}{K - H}\right)[(c_1 + c_2 e)A + c_3 \lambda_s]$	$\frac{K_0^2}{K_0 - H}$	$\sigma_m \leq 0,\ \dot{\lambda} = \dot{\lambda}_s = A\dot{e},\ \dot{\lambda}_p > 0$
5	0	0	$K_0(1-\lambda) c_3 \lambda_s$	0	$\sigma_m > 0,\ \dot{\lambda} = 0$
6	$G_0 e^c A$	$G_0 e^c B$	$K_0(1-\lambda)[(c_1 + c_2 e)A + c_3 \lambda_s] + K_0 \varepsilon_v^e A$	$K_0 \varepsilon_v^e B$	$\sigma_m > 0,\ \dot{\lambda} = \dot{\lambda}_s + \dot{\lambda}_t,\ \dot{\varepsilon}_v \geq 0$
7	$G_0 e^c A$	0	$K_0(1-\lambda)[(c_1 + c_2 e)A + c_3 \lambda_s] + K_0 \varepsilon_v^e A$	0	$\sigma_m > 0,\ \dot{\lambda} = \dot{\lambda}_s = A\dot{e},\ \dot{\varepsilon}_v < 0$

Table 4.2 : Constitutive matrix coefficients (Resende (1987))

4.2.7 Damage evolution laws

The damage evolution laws form the basis of the material modelling. A complete discussion of the different possible kinds of laws and their features can be found in Resende (1987). Investigations have shown that monotonic damage evolution takes the form of an S-shaped λ curve with the high strain end of the curve being asymptotic to a line of very low positive slope. This gives the stress-strain responses shown in Figure 4.3 which is typical of brittle materials. The type of function adopted to approximate the damage evolution was a rational function. This type of function has proved to be popular in the past since they inherently possess the shape of the damage evolution curves shown in Figure 4.3 . It has been suggested that both the shear damage and hydrostatic damage evolution are of this form.

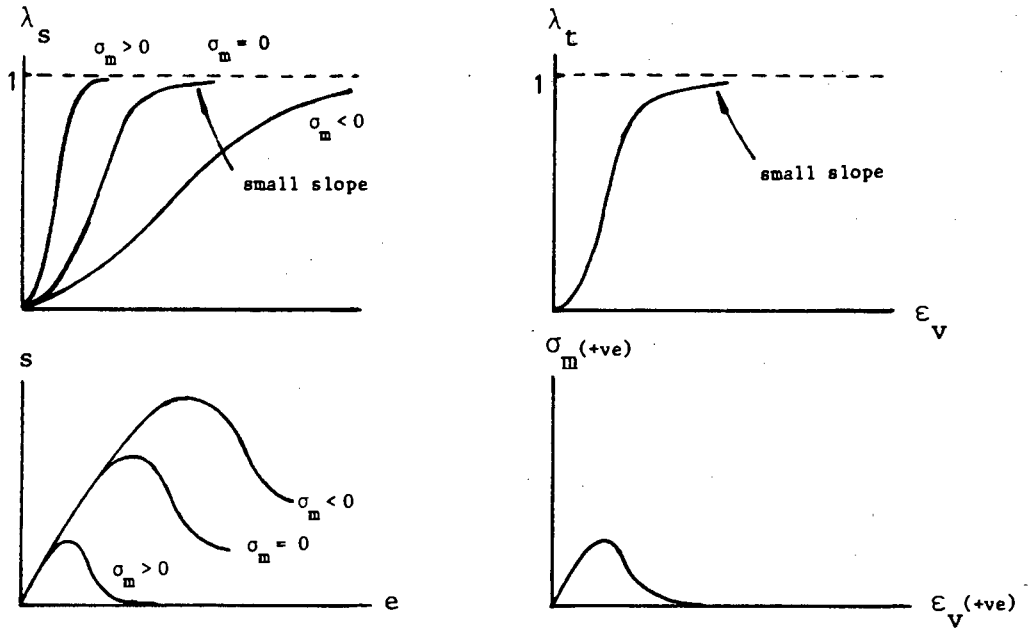

Figure 4.3 : Damage evolution curves

If we integrate the evolution laws

$$\dot{\lambda}_s = A(e,\sigma_m)\dot{e}$$

and $$\dot{\lambda}_t = B(\epsilon_v)\dot{\epsilon}_v$$

for monotonic loading, we get the S-shaped curves in Figure 4.3. These curves can then be represented by rational functions as follows :

For shear damage

$$\lambda_s = \frac{a_1^2 e^2}{1 + a_2 e + a_1^2 e^2} \quad , \qquad (4.30a)$$

and for hydrostatic tension damage

$$\lambda_t = \frac{b_1^2 \epsilon_v^2}{1 + b_2\epsilon_v + b_1^2\epsilon_v^2} \quad . \tag{4.30b}$$

The constants a_1 , a_2 , b_1 , b_2 must be calibrated for each kind of brittle material, and the procedure is shown in section 4.4 .

The constants a_1 , a_2 are contained in $A(e,\sigma_m)$ and are a function of the deviator strain and hydrostatic stress (still to be introduced). The constants b_1 , b_2 in $B(\epsilon_v)$ are a function of the volume strain. These relationships are shown in Figure 4.3.

4.3 Constitutive Equations for Plane Problems

So far, the equations have been derived in invariant form. However for application purposes, a generalised form is required. This procedure follows Resende and Martin (1985) where a form for three dimensions was derived. Here it will only be done for two dimensions because this restriction applies to the localization studies in this thesis.

In tensor form the stress and strain are written as

$$\underset{\sim}{T} = \begin{bmatrix} \sigma_{11} & \sigma_{13} & 0 \\ \sigma_{21} & \sigma_{22} & 0 \\ 0 & 0 & \sigma_{33} \end{bmatrix} \quad \underset{\sim}{E} = \begin{bmatrix} \epsilon_{11} & \gamma_{12} & 0 \\ \gamma_{21} & \epsilon_{22} & 0 \\ 0 & 0 & \epsilon_{33} \end{bmatrix}$$

these are written in vector form as

$$\underset{\sim}{\sigma} = (\sigma_{11} \quad \sigma_{22} \quad \sigma_{12} \quad \sigma_{33})^T$$
$$\underset{\sim}{\epsilon} = (\epsilon_{11} \quad \epsilon_{22} \quad \gamma_{12} \quad \epsilon_{33})^T$$
where $\gamma_{12} = 2\epsilon_{12}$. (4.31)

The derivatoric components of stress and strain,

$$s_{ij} = \sigma_{ij} - \frac{1}{3}\sigma_{kk}\delta_{ij} \quad , \quad e_{ij} = \epsilon_{ij} - \frac{1}{3}\epsilon_{kk}\delta_{ij} \quad ,$$

can also be conveniently represented in vector form, giving a

$$\underset{\sim}{s} = (s_{11} \quad s_{22} \quad s_{12})^T$$
$$\underset{\sim}{e} = (e_{11} \quad e_{22} \quad e_{12})^T \quad . \tag{4.32}$$

Now using the fact that

$$s_{11} + s_{22} + s_{33} = 0$$
$$e_{11} + e_{22} + e_{33} = 0 \quad , \tag{4.33}$$

the total stresses and strains can be written in terms of the deviatoric vectors, the mean hydrostatic stress, σ_m , and the volume strains,

$$\dot{\underset{\sim}{\sigma}} = \begin{Bmatrix} \dot{\sigma}_{11} \\ \dot{\sigma}_{22} \\ \dot{\sigma}_{12} \\ \dot{\sigma}_{33} \end{Bmatrix} = \begin{bmatrix} 1 & 0 & 0 & 1 \\ 0 & 1 & 0 & 1 \\ 0 & 0 & 1 & 0 \\ -1 & -1 & 0 & 1 \end{bmatrix} \begin{Bmatrix} \dot{s}_{11} \\ \dot{s}_{22} \\ \dot{s}_{12} \\ \dot{\sigma}_m \end{Bmatrix} = \underset{\sim}{C} \begin{Bmatrix} \dot{\underset{\sim}{s}} \\ \dot{\sigma}_m \end{Bmatrix} \tag{4.34}$$

$$\begin{Bmatrix} \dot{\underset{\sim}{e}} \\ \dot{\epsilon}_v \end{Bmatrix} = \begin{Bmatrix} \dot{e}_{11} \\ \dot{e}_{22} \\ \dot{e}_{12} \\ \dot{\epsilon}_v \end{Bmatrix} = \begin{bmatrix} \frac{2}{3} & \frac{-1}{3} & 0 & \frac{-1}{3} \\ \frac{-1}{3} & \frac{2}{3} & 0 & \frac{-1}{3} \\ 0 & 0 & \frac{1}{2} & 0 \\ 1 & 1 & 0 & 1 \end{bmatrix} \begin{Bmatrix} \dot{\epsilon}_{11} \\ \dot{\epsilon}_{22} \\ \dot{\gamma}_{12} \\ \dot{\epsilon}_{33} \end{Bmatrix} = \hat{\underset{\sim}{C}} \dot{\underset{\sim}{\epsilon}} \quad . \tag{4.35}$$

Now, using the definition for the invariant strain rate and equations (4.33),

$$\dot{e} = \frac{1}{s} s_{ij} \dot{e}_{ij}$$

$$= \frac{1}{s} \left(s_{11}\dot{e}_{11} + s_{22}\dot{e}_{22} + s_{33}\dot{e}_{33} + s_{12}\dot{e}_{12} + s_{21}\dot{e}_{21} \right)$$

$$= \frac{1}{s} \left(\left(2s_{11} + s_{22} \right)\dot{e}_{11} + \left(s_{11} + 2s_{22} \right)\dot{e}_{22} + 2s_{12}\dot{e}_{12} \right)$$

$$= \frac{1}{s} \left(s_{11} \; s_{22} \; s_{12} \right) \begin{bmatrix} 2 & 1 & 0 \\ 1 & 2 & 0 \\ 0 & 0 & 2 \end{bmatrix} \begin{Bmatrix} \dot{e}_{11} \\ \dot{e}_{22} \\ \dot{e}_{12} \end{Bmatrix}$$

$$\dot{e} = \frac{1}{s} \underset{\sim}{s}^T \underset{\sim}{n} \dot{\underset{\sim}{e}} \quad . \tag{4.36}$$

Similarly,

$$s = \left(\frac{1}{2} s_{ij} \, s_{ij} \right)^{1/2} = \left(\frac{1}{2} \underset{\sim}{s}^T \underset{\sim}{n} \underset{\sim}{s} \right)^{1/2} \tag{4.37}$$

$$\dot{s} = \frac{1}{2s} s_{ij} \dot{s}_{ij} = \frac{1}{2s} \underset{\sim}{s}^T \underset{\sim}{n} \dot{\underset{\sim}{s}} \quad . \tag{4.38}$$

By using equation (4.29) and the above relations, the required relation being $\dot{\underset{\sim}{\sigma}}$ and $\dot{\underset{\sim}{\epsilon}}$ can be found

$$\begin{Bmatrix} \dot{s} \\ \dot{\sigma}_m \end{Bmatrix} = \begin{bmatrix} (G-a_{11}) & -a_{12} \\ -a_{21} & (K-a_{22}) \end{bmatrix} \begin{Bmatrix} \dot{e} \\ \dot{\epsilon}_v \end{Bmatrix} .$$

Using (4.36), (4.37) and (4.38)

$$\dot{s} = (G-a_{11})\dot{e} - a_{12}\dot{\epsilon}_v$$

$$\frac{\underset{\sim}{s}^T \underset{\sim}{n} \dot{\underset{\sim}{s}}}{2s} = G\frac{\underset{\sim}{s}^T \underset{\sim}{n} \dot{\underset{\sim}{e}}}{s} - a_{11}\frac{\underset{\sim}{s}^T \underset{\sim}{n} \dot{\underset{\sim}{e}}}{s} - \frac{a_{12}}{s^2}\frac{\underset{\sim}{s}^T \underset{\sim}{n} \underset{\sim}{s}}{2}\dot{\epsilon}_v$$

$$= G\frac{\underset{\sim}{s}^T \underset{\sim}{n} \dot{\underset{\sim}{e}}}{s} = a_{11}\frac{\underset{\sim}{s}^T \underset{\sim}{n} \underset{\sim}{s}}{s^2}\frac{\underset{\sim}{s}^T \underset{\sim}{n} \dot{\underset{\sim}{e}}}{s} - \frac{a_{12}}{s^2}\frac{\underset{\sim}{s}^T \underset{\sim}{n} \underset{\sim}{s}}{2}\dot{\epsilon}_v$$

$$\dot{\underset{\sim}{s}} = \left(2G\underset{\sim}{I} - \frac{a_{11}}{s^2}\underset{\sim}{s}\,\underset{\sim}{s}^T\underset{\sim}{n}\right)\dot{\underset{\sim}{e}} - \frac{a_{12}}{s}\underset{\sim}{s}\,\dot{\epsilon}_v \quad . \qquad (4.39a)$$

And using (4.36)

$$\dot{\sigma}_m = -a_{21}\dot{e} + (K - a_{22})\dot{\epsilon}_v$$

$$= -a_{21}\frac{\underset{\sim}{s}^T \underset{\sim}{n}}{s}\dot{\underset{\sim}{e}} + (K - a_{22})\dot{\epsilon}_v \quad . \qquad (4.39b)$$

Or in matrix form, as in Resende and Martin (1985),

$$\begin{Bmatrix} \dot{\underset{\sim}{s}} \\ \dot{\sigma}_m \end{Bmatrix} = \begin{bmatrix} 2G\underset{\sim}{I} - \frac{a_{11}}{s^2}\underset{\sim}{s}\,\underset{\sim}{s}^T\underset{\sim}{n} & \frac{-a_{12}}{s}\underset{\sim}{s} \\ \frac{-a_{21}}{s}\underset{\sim}{s}^T\underset{\sim}{n} & K - a_{22} \end{bmatrix} \begin{Bmatrix} \dot{\underset{\sim}{e}} \\ \dot{\epsilon}_v \end{Bmatrix} = D \begin{Bmatrix} \dot{\underset{\sim}{e}} \\ \dot{\epsilon}_v \end{Bmatrix} \quad (4.40)$$

where $\underset{\sim}{I}$ = a 3 x 3 unit matrix.

This shows that the coefficients a_{11}, a_{12}, a_{21}, a_{22} can be taken directly from the discussion of the invariant equations. It leaves the task of transforming equations (4.40) into stress and strain rates $\dot{\underset{\sim}{\sigma}}$ and $\dot{\underset{\sim}{\epsilon}}$, which can be done as follows

$$\dot{\underset{\sim}{\sigma}} = \underset{\sim}{C} \begin{Bmatrix} \dot{\underset{\sim}{s}} \\ \dot{\sigma}_m \end{Bmatrix} = \underset{\sim}{C}\,\underset{\sim}{D} \begin{Bmatrix} \dot{\underset{\sim}{e}} \\ \dot{\epsilon}_v \end{Bmatrix} = \underset{\sim}{C}\,\underset{\sim}{D}\,\hat{\underset{\sim}{C}}\,\dot{\underset{\sim}{\epsilon}}$$

or $$\dot{\underset{\sim}{\sigma}} = \underset{\sim}{D}^* \dot{\underset{\sim}{\epsilon}} \quad , \qquad (4.41)$$

which is the generalised constitutive equation for plane problems. The matrix $\underset{\sim}{D}^*$ can therefore be obtained explicitly as in Resende and Martin (1985); however, this will not be done here.

Equation (4.41) reduces to the elastic relationship by setting a_{11}, a_{12}, a_{21}, $a_{22} = 0$.

$$\dot{\underset{\sim}{\sigma}} = \underset{\sim}{C} \begin{bmatrix} 2G & & & \\ & 2G & & \\ & & 2G & \\ & & & K \end{bmatrix} \hat{\underset{\sim}{C}}\, \dot{\underset{\sim}{\epsilon}} = \begin{bmatrix} \frac{4}{3}G+K & -\frac{2}{3}G+K & 0 & -\frac{2}{3}G+K \\ & \frac{4}{3}G+K & 0 & -\frac{2}{3}G+K \\ \text{symmetric} & & G & 0 \\ & & & \frac{4}{3}G+K \end{bmatrix} \dot{\underset{\sim}{\epsilon}}$$

and by using $G = \frac{E}{2(1+\nu)}$, $K = \frac{E}{3(1-2\nu)}$, we get

$$\dot{\underset{\sim}{\sigma}} = \frac{E}{(1+\nu)(1-2\nu)} \begin{bmatrix} (1-\nu) & \nu & 0 & \nu \\ \nu & (1-\nu) & 0 & \nu \\ 0 & 0 & \tfrac{1}{2}(1-2\nu) & 0 \\ \nu & \nu & 0 & (1-\nu) \end{bmatrix} \underset{\sim}{\epsilon} \quad , \qquad (4.42)$$

which can be reduced to plane stress and plane strain cases.

4.4 Model Parameters

The parameters that were introduced to control the behaviour of the model must be identified and calibrated separately for each type of brittle material. These material dependent parameters can be calibrated and quantified by means of a series of simple laboratory tests as presented by Resende (1985, 1986). The parameters can be grouped into six distinct categories and are summarised, together with the tests required for their calibration, in Table 4.3.

In order to begin the calibration, it is first necessary to derive some important quantities, to define the hydrostatic stress shear damage behaviour and to make some assumptions about the shear-volumetric coupling.

material parameters and description	equations	tests required
G_o , K_o = initial elastic moduli	(29)	monotonic loading multiaxial tests (G_o) hydrostatic compression test (K_o)
W, D, σ_{mo} = cap hardening parameters and initial cap position	(12)	hydrostatic compression test
A (e, σ_m) = shear damage parameters a_1^* , a_2 , a_3	(28),(30),(51)	monotonic loading multiaxial tests e.g. uniaxial, biaxial, triaxial
B (ε_v) = hydrostatic tension damage parameters b_1 , b_2	(28),(30)	monotonic tensile tests
c_1, c_2, c_3 = shear damage - volumetric coupling parameters	(22)	from volumetric behaviour of monotonic compression tests
d_1 = permanent shear strain parameter	(5)	unloading and reloading information from compression tests

Table 4.3 : Material parameter identification and description

4.4.1 Further quantities and assumptions used for calibration

Recall the form of the shear damage evolution equation

$$\lambda_s = \frac{a_1^2 e^2}{1 + a_2 e + a_1^2 e^2} \quad .$$

Substituting $\lambda = \lambda_s$ we get

$$s = G_o(1-\lambda)e = G_o \left(\frac{1 + a_2 e}{1 + a_2 e + a_1^2 e^2} \right) e \quad , \qquad (4.43)$$

which is used to determine the residual and peak stresses as shown in Figure 4.4.

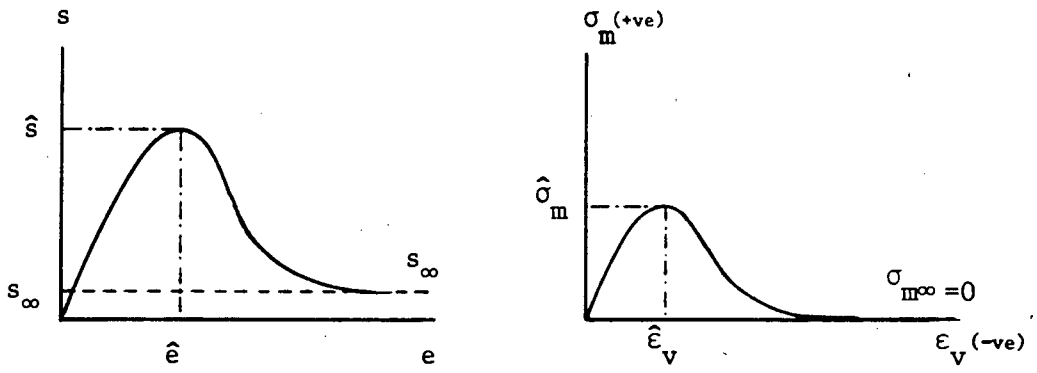

(a) for shear damage calibration

(b) for hydrostatic tension damage calibration

Figure 4.4 : Residual and peak stresses and strains

(i) The residual stress is obtained by taking limits as $e \to \infty$ of equation (4.43), giving

$$s_\infty = \frac{G_o a_2}{a_1^2} \quad . \tag{4.44}$$

(ii) The peak shear stress is given by

$$\hat{s} = \frac{G_o}{2a_1 - a_2} \quad , \tag{4.45}$$

and the corresponding shear strain

$$\hat{e} = \frac{1}{a_1 - a_2} \quad . \tag{4.46}$$

Similarly, for the hydrostatic tension damage,

$$\lambda_t = \frac{b_1^2 \epsilon_v^2}{1 + b_2 \epsilon_v + b_1^2 \epsilon_v^2} \quad ,$$

and substituting as follows,

$$\sigma_m = K_o(1-\lambda)\epsilon_v = K_o\left(\frac{1 + b_2\epsilon_v}{1+b_2\epsilon_v + b_1^2\epsilon_v^2}\right)\epsilon_v \quad , \tag{4.47}$$

yielding (see Figure 4.4) :-

(iii) the residual hydrostatic tension stress;

$$\sigma_{m\infty} = \frac{K_o b_2}{b_1^2} \quad , \tag{4.48}$$

(iv) and the peak hydrostatic tension stress and volumetric strain

$$\hat{\sigma}_m = \frac{K_o}{2b_1 - b_2} \quad , \tag{4.49}$$

$$\hat{\epsilon}_v = \frac{1}{b_1 - b_2} \quad . \tag{4.50}$$

All these quantities play an important role in the calibration procedure. Two important aspects need to be addressed before calibration. These are the dependence of shear damage on the hydrostatic stress, which has yet to be introduced through $A(e,\sigma_m)$, and the question of quantifying the shear-volumetric coupling constants c_1 , c_2 amd c_3 .

(v) The hydrostatic stress influence on shear damage is introduced by means of the expression

$$a_1 = a_1^* \left[-(\sigma_m - a_3) \right]^{-1/4} \tag{4.51}$$

for Kupfer concrete, or

$$a_1 = a_1^* \left[-(\sigma_m - a_3) \right]^{-1/2} \tag{4.52}$$

for norite, rock, or ordinary concrete.

Here, a_1^* is a constant;

a_3 is the maximum attainable hydrostatic tension stress (compare with $\hat{\sigma}_m$ in equation (4.49));

$-1/4$ is found appropriate for the Kupfer concrete;

$-1/2$ is a value more typical of other rocks and concretes.

(vi) The shear-volumetric coupling in equation (4.23), is in a rate form and must be approximated by writing

$$\epsilon_v^d = (c_1 + c_2 d)\lambda_s + c_3 \lambda_s e \tag{4.53}$$

before the coupling constants can be quantified.

4.4.2 Calibration for concrete

The calibration for concrete makes use of the experimental data of Kupfer *et al* (1969,1973), this data is in the form of uniaxial and biaxial compression, tension and compression-tension tests.

From the uniaxial tension, uniaxial and biaxial compression tests, it is estimated that :-

$$G_o = 200 \text{ ksi}$$

$$K_o = 240 \text{ ksi} \quad .$$

From the data available, it is not possible to obtain the hydrostatic compression material parameters, but for other concretes it is estimated that :-

$$W = -0.125$$

$$D = 0.03 \text{ ksi}^{-1}$$

$$\sigma_{mo} = 3.15 \text{ ksi} \quad .$$

To quantify the shear damage parameters, it is assumed that concrete has zero residual shear stress, which is appropriate for structural concrete, thus $s_\infty = 0$. From equation (4.44) we get

$$a_2 = \frac{s_\infty a_1^2}{G_o} = 0 \quad .$$

Now $$a_1 = a_1^* \left[-(\sigma_m - a_3) \right]^{-1/4}$$

where a_3 , the maximum attainable hydrostatic tension stress, is estimated from the uniaxial tension test,

$$a_3 = 0.2 \text{ ksi} \quad .$$

Substituting the expression for a_1 and the values for a_2 and a_3 into equation (4.45) yields

$$\hat{s} = \frac{G_o\,[-(\sigma_m - 0.2)]^{1/4}}{2a_1^*} \quad . \tag{4.54}$$

This can be used via a trial and error approach to obtain a_1^* to give a good fit of the peak shear strain for the unizaxial and biaxial compression tests (see Figure 14 in Resende (1986)),

$$a_1^* = 337.5 \quad .$$

The shear-volumetric coupling constants are assumed to be inter-dependent, $c_1 = c_2/20$, $c_3 = -c_2/2$ so that only one material constant needs calibrating, giving

$$c_2 = -0.025 \quad .$$

To obtain a value for the permanent shear strain constant d_1 , it is necessary to have some unloading-reloading data which is not provided by Kupfer *et al* . However, consulting other references (eg. Spooner and Dougill (1975)) yields a value of

$$d_1 = 0.005 \quad .$$

Finally, the hydrostatic tension damage constants can be obtained by first assuming that cracked concrete retains no hydrostatic strength ($\sigma_{m\infty} = 0$) thus,

$$b_2 = \frac{\sigma_{m\infty}\, b_1^2}{K_o} = 0 \quad ,$$

and then by using $\hat{\sigma}_m = a_3 = 0.2$ in equation (4.49),

$$b_1 = \frac{K_o}{2\sigma_m} = 6000 \quad ,$$

thus completing the calibration for concrete.

4.4.3 Calibration for norite

This calibration uses the experimental results of Stavropoulou (1982) and Bieniawski (1967) which are generally more complete than the data used for the concrete calibration.

Using Stavropoulou's hydrostatic compression tests and Bieniawski's uniaxial tension tests, the bulk modulus is estimated as

$$K_o = 60 \text{ GPa} \; .$$

The shear modulus of elasticity is estimated from Bieniawski's uniaxial tension tests and Stavropoulou's triaxial compression tests as

$$G_o = 70 \text{ GPa} \; .$$

The hydrostatic compression parameters are unnecessary since the cap is "deactivated" by setting the cap yield surface out of the range of interest as follows,

$$\sigma_{mo} = -10 \text{ GPa} \; .$$

This takes account of the fact that Stavropoulou's tests show the degree of nonlinearity in hydrostatic compression to be insignificant.

The hydrostatic tension damage parameters are obtained by assuming, as in concrete, that

$$b_2 = 0$$

and then choosing

$$b_1 = 2300$$

to give a good fit of peak stresses with Bieniawski's uniaxial tension experiments.

The above choice immediately yields a value for $\hat{\sigma}_m$ from equation (4.49) and hence a value for a_3 (equation (4.52));

$$\hat{\sigma}_m = \frac{K_o}{2b_1} = 13 \text{ MPa}$$

or

$$a_3 = 13 \text{ MPa} \quad .$$

In order to calibrate the shear damage parameters, Stavropoulou's triaxial compression tests are used. These show that the residual shear stresses can be approximated by

$$s_\infty = \frac{G_o a_2^2}{a_1^2} = a_3 - \sigma_m \quad . \tag{4.55}$$

In addition, by using equations (4.55), (4.52) and substituting into (4.45) yields

$$\hat{s} = \frac{G_o (a_3 - \sigma_m)^{1/2}}{2G_o a_1^* - a_1^{*2}(a_3 - \sigma_m)^{1/2}} \tag{4.56}$$

which gives the direct relation between $\hat{s}$ and a_1^* for a particular σ_m . Again, by using a trial and error iterative procedure, a value

for a_1 can be obtained that gives a good fit of peak shear stresses for the triaxial compression tests. This gives

$$a_1^* = 1700$$

and thus $a_2 = 60$.

Finally, the calibration is completed by assuming $c_1 = -c_2/20$, $c_3 = c_2/2$ for the shear-volumetric coupling parameters. Here a value for c_2 is obtained from observations of the volumetric response in the triaxial tests, giving

$$c_2 = -0.15 \quad .$$

CHAPTER 5

FINITE ELEMENT IMPLEMENTATION

5.1 Introduction

This chapter deals with the implementation of the localization theory. For this purpose, NOSTRUM (1983), a general purpose, research orientated finite element program for the static and dynamic, linear and nonlinear analysis of two dimensional plane problems was used. The reasons are that firstly, it incorporates Resende's damage model, and secondly, the code is open to development. Several modifications were necessary for this implementation, and these are described here.

5.2 NOSTRUM Background

NOSTRUM was developed in 1983 by the University of Cape Town Applied Mechanics Research Unit. It is primarily a research tool geared to the developers' interests, and it can be adapted for any general research requirements. It also has the capability for solving real practical problems which arise in industry. Since a sufficiently large class of research problems are two dimensional, the code was developed to handle only plane stress, plane strain and axisymmetric problems. The code is capable of both full and modified Newton-Raphson as well as Euler forward equilibrium iteration schemes. In this study, the full Newton-Raphson scheme was used.

NOSTRUM has been used for a wide variety of research problems, some of which are currently receiving attention are:-

(i) nonlinear constitutive laws for rock, concrete and soils, for example, the damage model used in this study ;

(ii) geotechnical problems ;

(iii) nonlinear geometric and stability problems ;

(iv) friction and contact problems ;

(v) soil-structure interaction ;

(vi) creep and viscoplasticity ;

(vii) coupled thermomechanical problems ;

(viii) solidification processes ;

(ix) thermal problems ;

(x) piezo-electric problems.

5.3 Implementation of the Localization Criteria

The modular structure of NOSTRUM lends itself well to modifications with the minimum affect on other subroutines. It allows new features and tasks to be added by means of a single CALL statement in the code. In implementing the localization criteria, it was important to make the new additions as simple and as flexible as possible so that any further development of these features can easily be made.

Figure 5.1 gives an outline of the NOSTRUM software structure, and shows where the relevant localization checking subroutines fit into the existing structure. Only the important subroutines are shown so as to keep the overall layout clear. Table 5.1 summarises the subroutine tasks.

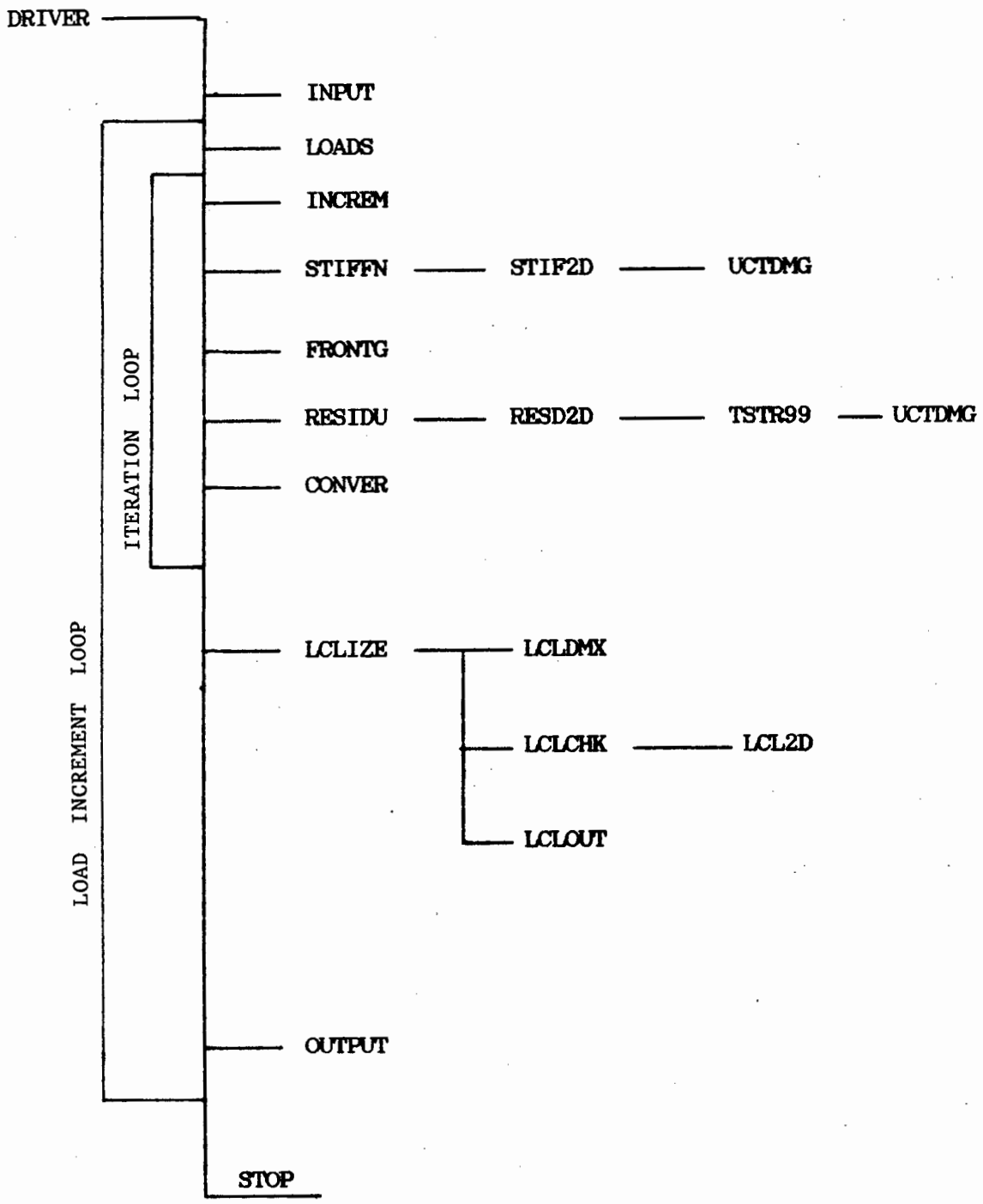

Figure 5.1 : Simplified NOSTRUM call chart

DRIVER	-	is the driver program which controls the solution procedure.
INPUT	-	controls all input data, which is checked for fatal errors.
LOADS	-	controls the calculation of the element load vectors.
STIFFN	-	controls the calculation of the element stiffness matrices, which are formulated in STIF2D and UCTDMG.
UCTDMG	-	controls all damage mechanics constitutive calculations.
FRONTG	-	assembles and solves the stiffness matrix by means of an out-of-core frontal solver.
RESIDU	-	controls the calculation of the residual load vector. RESD2D controls the calculation of the internal load vector, the stress calculations are carried out in TSTR99.
CONVER	-	checks the convergence of the iterative process against a tolerance set by the user.
LCLIZE	-	controls all localization calculations which are carried out in LCLDMX, LCLCHK and LCL2D.
OUTPUT	-	prints the general results.

Table 5.1 : NOSTRUM subroutine functions

Following the computational procedure set out in Chapter 3, the localization polynomial is calculated, checked for minima and if the localization condition is satisfied, the $\underset{\sim}{n}$ and $\underset{\sim}{m}$ vectors are computed. The localization calculations are performed at the element level after each solution step in the incremental analysis has converged. Ortiz (1986) checks the condition at the reduced integration points; however, in this work this was not seen as necessary. Thus every integration point is checked for localization. This does not significantly affect the solution time for 2D problems because the localization polynomial approach is used. However, in 3D problems where eigen iteration procedures are required, efficiency would be an important consideration.

As previously mentioned, a full Newton-Raphson iteration scheme was employed in this work, whereas Needleman and Tvergaard (1982) and Ortiz *et al* (1986) generally use an Euler-forward scheme with very fine increments. The advantages of using the Newton-Raphson scheme are that large increments can be made and convergence is good, and hence less computer time is used. However, the disadvantage is that by taking large increments, some information on the progression of damage and the onset of localization can be lost.

From the computational point of view, it should be noted that storage of localization related data requires special consideration. Here it is the researcher who should decide on an approach that is geared to his particular needs. In this work, data was only stored for each gauss point before being output, and thus relatively little memory and file space was required.

5.4 Aspects of Numerical Localization Studies

The most important aspect of finite element localization studies is that we can only calculate the bifurcation points of the discrete system (de Borst (1986)). This aspect is compounded by the fact that when using standard incremental procedures, we can only determine when we have passed the bifurcation point (Figure 5.2)

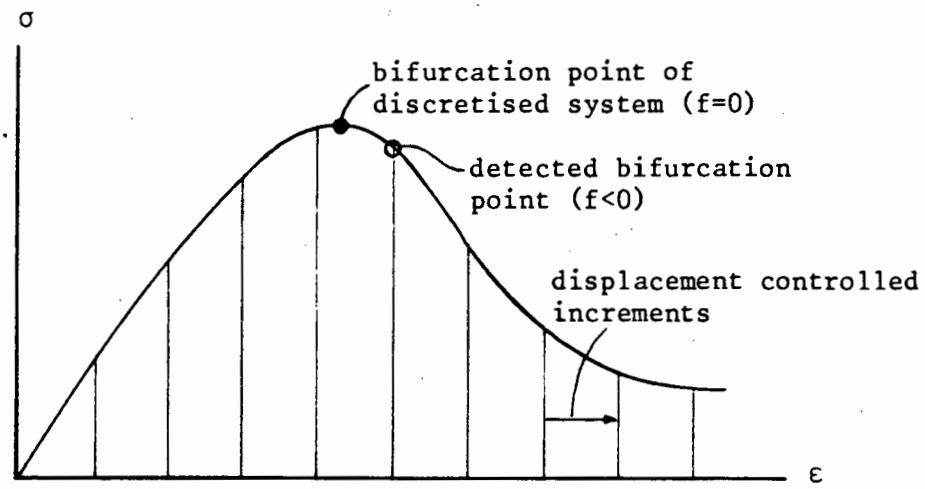

Figure 5.2 : Incremental solutions and bifurcation points

Hence, the finer the increments, the closer we can get to the bifurcation point and the more expensive N-R schemes become, as noted by Needleman and Tvergaard (1982). It is for this reason that some researchers only use a forward stepping scheme. Other schemes have also received attention, de Borst (1986) for example, has shown that the BFGS system can be particularly efficient for bifurcation studies.

Another aspect, which is related to the situation described above, is the calculation of failure modes. The localization condition $f = 0$ is seldom achieved, and once the bifurcation point has been passed, we actually work with $f < 0$ as can be seen in Figure 5.3 . The shape of the

localization polynomial at f < 0 is different to the shape at f = 0, and from the diagram, it can be seen that the value of x at f_{min} can be affected substantially.

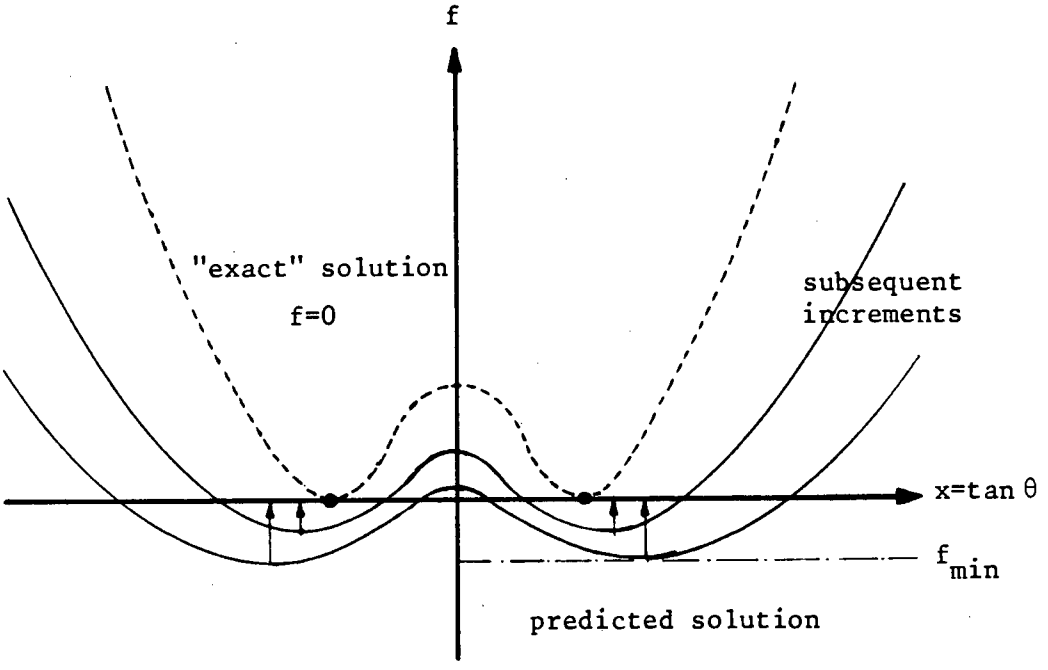

Note: the localization polynomial is not necessarily symmetric

Figure 5.3 : Effect of f < 0 on the localization polynomial

Again, the answer to these problems is to use very fine increments, but this is very expensive and in reality, the researcher should use his judgement to achieve some sort of balance between cost effectiveness and the accuracy of the solution.

CHAPTER 6

NUMERICAL RESULTS

6.1 Introduction

In this chapter, the numerical results are presented, analysed and compared with experimental records. The numerical examples cover a wide range of brittle material problems. These range from single element, single gauss point studies to larger boundary value problems. The aims of the tests were firstly to study the localized failure modes of brittle materials, secondly to examine the onset of localization and thirdly to test the damage mechanics constitutive theory. It must be stressed that we are looking at the qualitative performance of the theory, since even experimental data exhibits a large amount of scatter.

Two materials are used in this study, namely concrete and norite. Concrete is an important structural material and norite is structurally important with respect to deep level mining operations in South Africa. Norite is an igneous rock consisting of ferro-magnesium silicates and calcium-rich plagioclase and it has a uniaxial compressive strength of about ten times that of concrete.

The performance of the numerical localization procedures that were implemented are first investigated. The localized failure modes of concrete and norite are then studied and a parameter sensitivity study is performed. Following that, the results of some norite non-uniform triaxial tests and boundary value problems are discussed.

6.2 Numerical Verification

This section serves to check the implemented localization code from both the correctness and the performance point of view. The tests done were very simple; a single four-noded element with a single integration point was used so that the results could easily be checked and behavioural aspects accounted for. The Kupfer concrete calibration was used for the tests, which consisted of uniform uniaxial tension and compression tests.

6.2.1 Plain stress tests

The first test was to perform a uniaxial tension test in the x_1 and then the x_2 direction, knowing that the method should predict a pure splitting mode perpendicular to the applied load. This was indeed so, and the failure modes together with the corresponding shape of the localization polynomial are shown in Figure 6.1 .

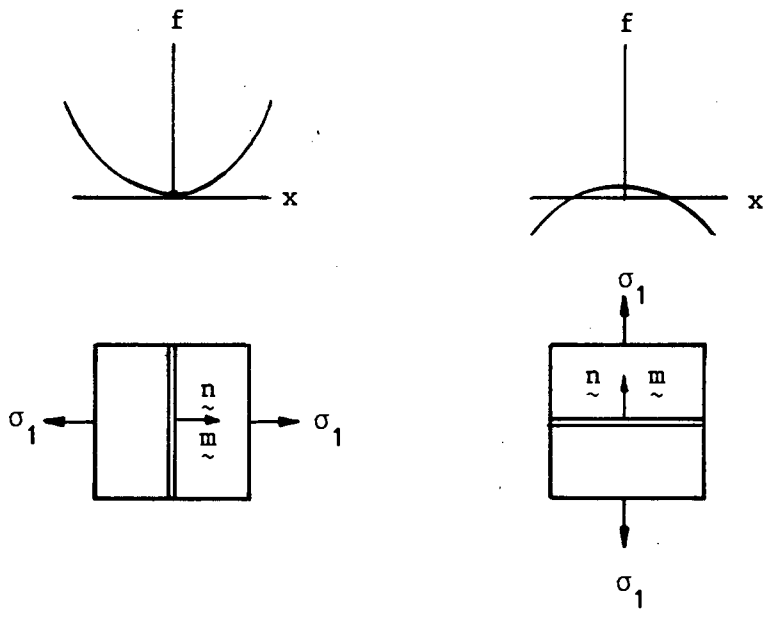

(a) x_1 tension (b) x_2 tension

Figure 6.1 : Plane stress uniaxial tension test

The second test was a uniaxial compression test in the x_1 and then the x_2 direction. Again the two results agree, however an interesting aspect emerges from this test, as shown in Figure 6.2. The shapes of the corresponding localization polynomials are different, as expected, since the polynomial gives $x = \tan \theta$, the orientation of the shear band with respect to the x_1 axis. However, $\phi = 90 - \theta$ in case (a) and $\phi = \theta$ in case (b), thus the two results converge on ϕ from opposing sides. This is because ($f \leq 0$) does not give an exact answer for θ . By performing the analysis with finer increments, the solution converges on $f = 0$ and the resulting ϕ's are equal.

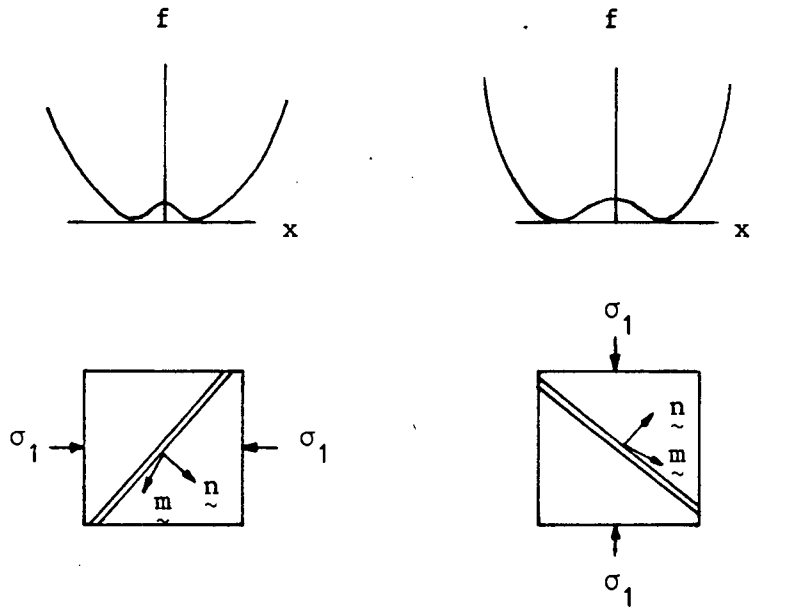

(a) x_1 compression (b) x_2 compression

Figure 6.2 : Plane stress uniaxial compression test

6.2.2 Axisymmetric and plain strain tests

The results for the axisymmetric uniaxial tension and compression tests are shown in Figure 6.3. The value of ϕ for the compression test differs slightly to that of the corresponding plane stress test because of the hoop stress in the axisymmetric case.

The results for the plain strain tests are similar to the axisymmetric tests since the stress state is now biaxial in nature.

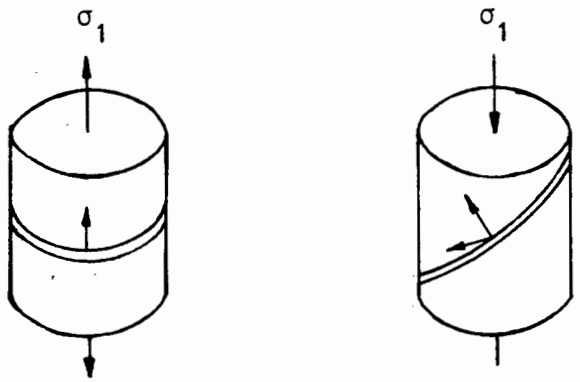

(a) tension (b) compression

Figure 6.3 : Axisymmetric uniaxial tension and compression tests

6.2.3 Behaviour of the localization polynomial

In chapter 5 some aspects of numerical solutions were investigated. Here, these are enlarged upon and some important results are studied.

As reported in chapter 5, the main area of caution is the fact that $f \leq 0$ is used and not $f = 0$ because of incremental solution procedures. Since the magnitude of f can be very large, $0(10^9$ to $10^{12})$, the value of θ , which gives the orientation of $\underset{\sim}{n}$, can be a few percent out as shown in Figure 6.4. Thus one must use sufficiently small increments to get an acceptable answer.

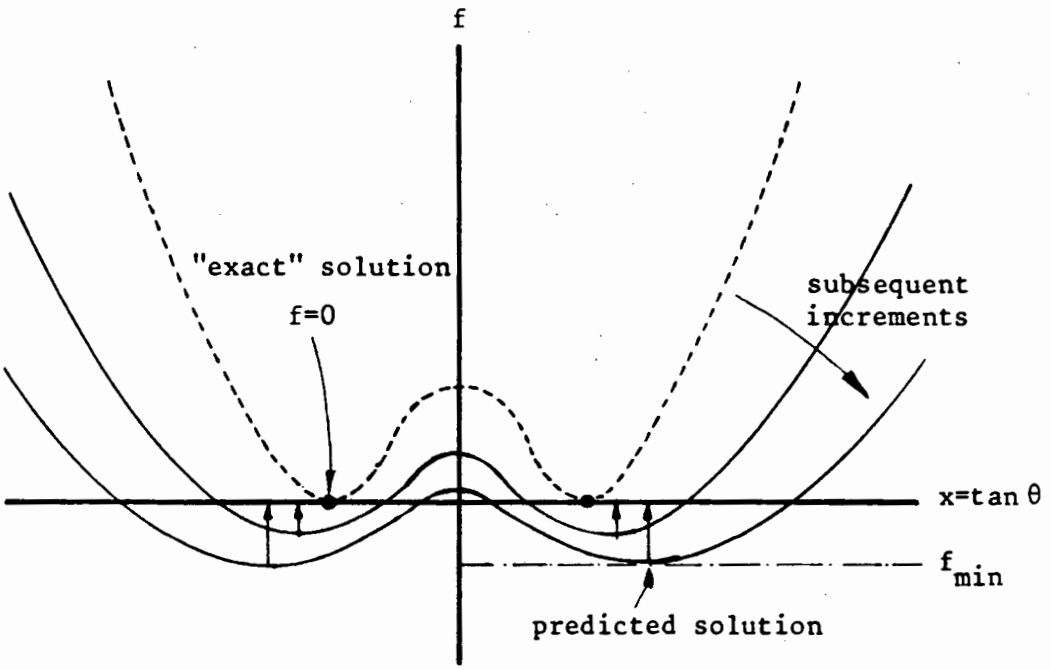

(a) Effect of f < 0 on the localization polynomial

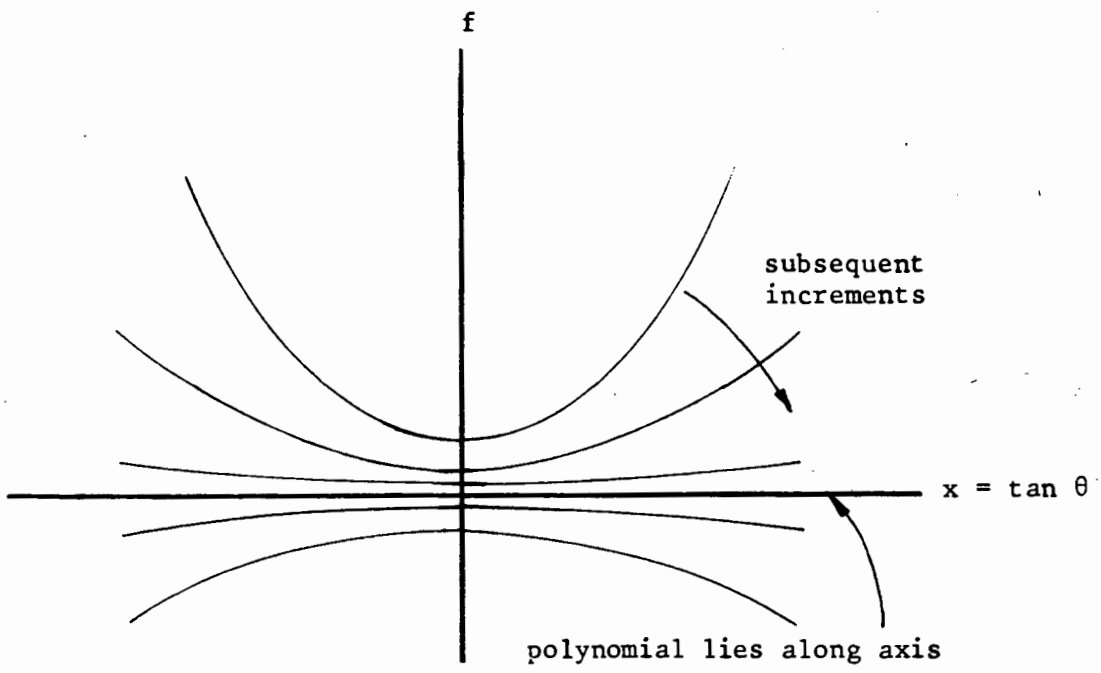

(b) Behaviour for "no preferred orientation"

Figure 6.4 : Behaviour of the localization polynomial

Another interesting aspect that occurred is shown in Figure 6.4b. Here the localization polynomial gets flatter and flatter as the solution proceeds, and tends to a straight line before inverting. This situation is interpreted as "no preferred orientation" since ϕ = 0°, 90° or lies somewhere between (in the case of the straight line).

6.3 Localized Failure Modes in Concrete

The Kupfer *et al* (1969, 1973) concrete calibration was used for the numerical analyses. The tests were either displacement, displacement-displacement or stress-displacement controlled and a single four-noded element with a single gauss point was used. Thus a uniform stress-field was assumed and we are effectively looking at a material point. The aim of the study was to determine the localized failure modes of concrete under predominantly biaxial stress states. To do this, plane strain, axisymmetric and plane stress tests were used.

The range of stress states studied are shown diagrammatically in Figure 6.5, and range from biaxial compression to biaxial tension.

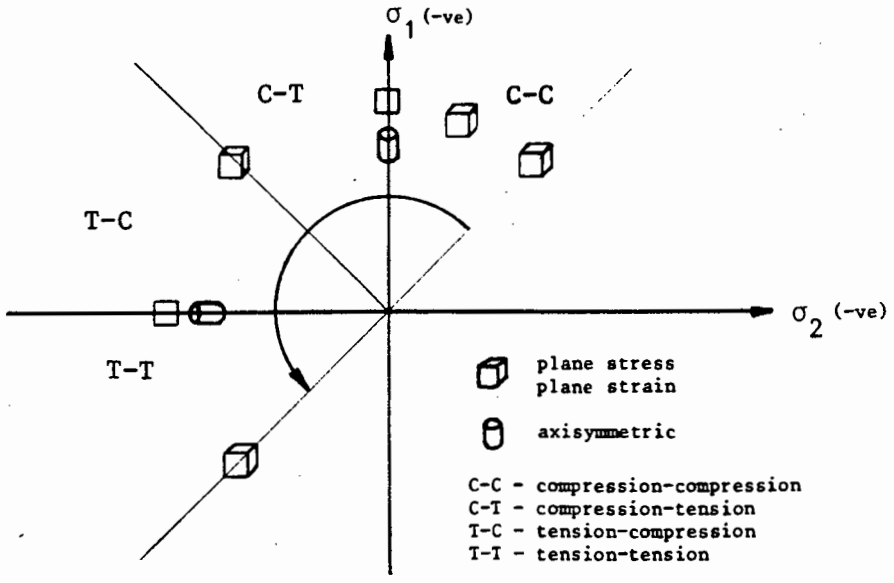

Figure 6.5 : Range of stress-states used in the concrete tests

This range of stresses was chosen so as to reproduce the experiments of Kupfer *et al* (1969) and van Mier (1986) and are summarised below :-

(i) biaxial compression; two studies were performed, in the first, loading was along the x_1 and x_2 axes, and in the second, along the x_1 and x_3 axes ;

(ii) uniaxial compression ;

(iii) compression-tension; here the transition between shear and splitting failure was also investigated ;

(iv) uniaxial tension ;

(v) biaxial tension.

The sign conventions are shown in Figure 6.6, the most important convention being the angle ϕ . This angle is taken as being the orientation of the failure plane with respect to the principle compressive load or the minor tensile load in the case of the tension tests. Compression is taken as negative. Failure occurs in the plane that contains the normal to the failure band.

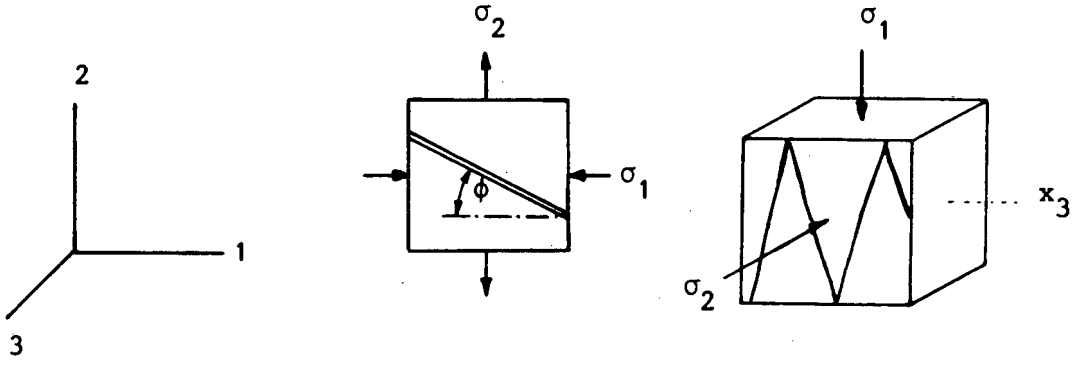

(a) right hand rule (b) orientation of failure band (c) failure in 1-3 plane

Figure 6.6 : Conventions and axes used for numerical analyses

6.3.1 Biaxial compression

The method predicted localization in all biaxial compression analyses. The results are tabulated in Table 6.1 , which shows for each stress ratio, σ_1/σ_2 , the orientation of the failure band ϕ , and the direction vector Ψ . The main features of these results are noted here and compared with results available from the literature, which are described in the text.

Test type	σ_1/σ_2	ϕ degrees	Ψ degrees	Model
Biaxial Compression				
a) x_1-x_3 plane	-1/-1	37.6	77.8	axi-s
	-2.4/-1	41.2	82.9	p-ϵ
b) x_1-x_2 plane	-1/-1	no preferred orientation		p-σ
	-1.8/-1	73.5	20.3	p-σ
	-7/-1	53.1	70.8	p-σ
	-10/-1	52.0	74.2	p-σ
	-45/-1	48.7	75.0	p-σ
Uniaxial Compression				
	-1/0	46.2	89.5	axi-s
	-1/0	52.1	78.8	p-σ

where : axi-s = Axisymmetric
p - ϵ = plane strain
p - σ = plane stress

Table 6.1 : Biaxial and uniaxial compression results

An important aspect to note is that two different classes of biaxial tests were performed. All the literature reviewed concentrates on the failure in the 1-3 plane, when it is clear that there is also localized failure in the 1-2 plane, as shown in Figure 6.7 taken from Kupfer *et al* (1969). Since with NOSTRUM it is not possible to directly

perform analyses with loading perpendicular to the plane stress model, only two such tests are reported, and instead, a more detailed study of the 1-2 failure plane was made.

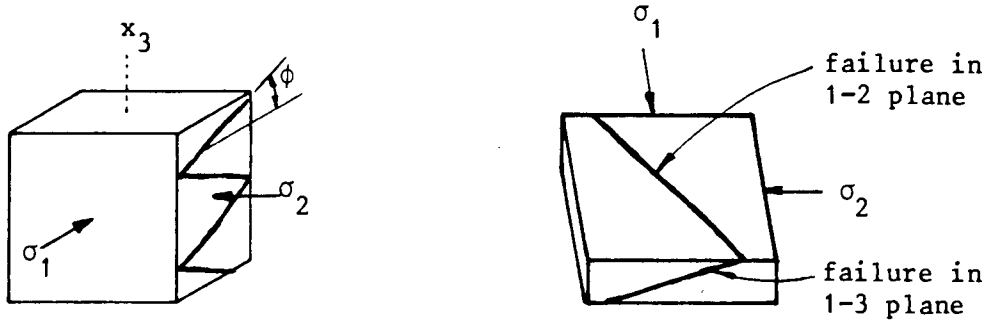

(a) Van Mier (b) Kupfer $\sigma_1/\sigma_2 = -1/-1$

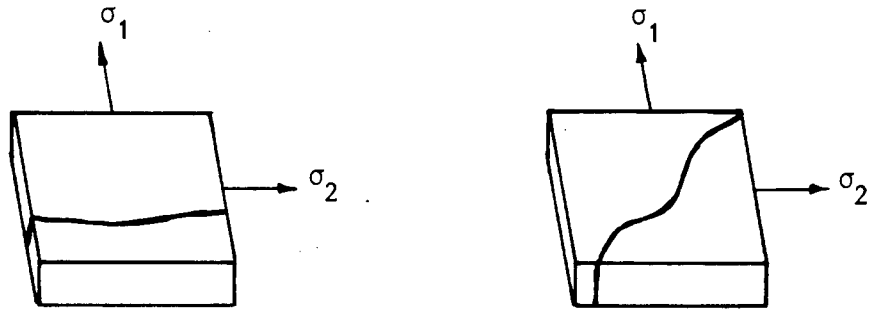

(c) Kupfer $\sigma_1/\sigma_2 = 1/0.54$ (d) Kupfer $\sigma_1/\sigma_2 = 1/1$

Figure 6.7 : Biaxial tests and failure planes

For the $x_1 - x_3$ plane analyses, the predicted angle ϕ ranges between 37° and 41°, and localization occurred just after the peak. The angle ψ indicates that a shear mode of failure is active. In comparison to the reported values for ϕ of 18° to 27°, Kupfer *et al* (1969), and 21° to 25°, van Mier (1986), the NOSTRUM values of ϕ are too large. However, the nature of the failure mode and the onset of localization is consistent with reported values. In addition, the trends observed, i.e. ϕ , ψ increasing for σ_1 increasing, are consistent with Ortiz (1986).

The x_1 - x_2 plane biaxial compression analyses also predicted localization, however there is a scarcity of data with which to compare results. Figure 6.7b (Kupfer *et al* (1969)) shows failure in this plane for σ_1/σ_2 = -1/-1 . However, failure in this plane tends to be unstable, van Mier (1986), and it is perhaps for this reason that data is unavailable. The results in Table 6.1 show that for σ_1/σ_2 = -1/-1 , there is no preferred orientation, but as conditions approach uniaxial compression so the failure plane tends to the diagonal and the mode changes from splitting to shear. These results tend to indicate that failure is unstable and very sensitive to the load path. As before, the onset of localization is at or just after the peak. Intuitively these results appear to be correct.

6.3.2 Uniaxial compression

Under uniaxial compression, the method predicts localization in the form of shear bands, at an angle ϕ = 46° to 52° , occurring after the peak. Kupfer *et al* (1969) observed shear failure at ϕ = 30° and van Mier's results agree with this. Ortiz's (1986) analytical results show that localization does not occur and that failure is the result of distributed damage. However, van Mier (1986) clearly states that "in uniaxial compression, a shear type fracture plane develops, which takes the form of a ziz-zag band". Thus, there is a consistency between the damage model prediction and van Mier (1986), even though the predicted ϕ is too large.

6.3.3 Compression-tension

In these examples, compression-tension refers to loading paths from near uniaxial compression (σ_1/σ_2 = -15.5/1) through to tension-

compression (σ_1/σ_2 = -0.5/1). In all cases the analysis predicts localization and the results are tabulated in Table 6.2 . The failure modes of the near uniaxial compression conditions are consistent with those noted in 6.3.2

Test type	σ_1/σ_2	ϕ degrees	ψ degrees	Model
Compression-Tension				
	-15.5/1	49.4	80.8	p-σ
	-12/1	49.0	80.3	p-σ
	-4/1	48.1	86.0	p-σ
	-2/1	45.4	88.4	p-σ
	-1/1	0	0	p-σ
	-0.7/1	0	0	p-σ
	-0.5/1	0	0	p-σ
Uniaxial Tension				
	0/1	0	0	p-σ
	0/1	0	0	axi-s

Table 6.2 : Compression-tension and uniaxial tension results

From Table 6.2, it is interesting to note that the transition between shear and splitting failure occurs at around σ_1/σ_2 = -1/1 , and that as the tensile loading component is increased, the failure plane tends to orient itself normal to the principal tensile direction.

These results are consistent with Ortiz (1986). However, the orientation of the failure plane is again over estimated.

It has been noted that a continuous transition of failure bonds between shear and splitting modes occurs. Experimental records show that this transition zone occurs between σ_1/σ_2 = -15/1 , Kupfer *et al*

(1969), to -30/1 , Nelissen (1972). These results are shown graphically in Figure 6.8. The damage model thus predicts an abrupt transition at σ_1/σ_2 = -1/1 , the same as the analytically determined ratio of Ortiz (1986).

The numerical results correctly show that after the transition, the failure mode orients itself perpendicular to the principal tensile load giving a pure splitting mode.

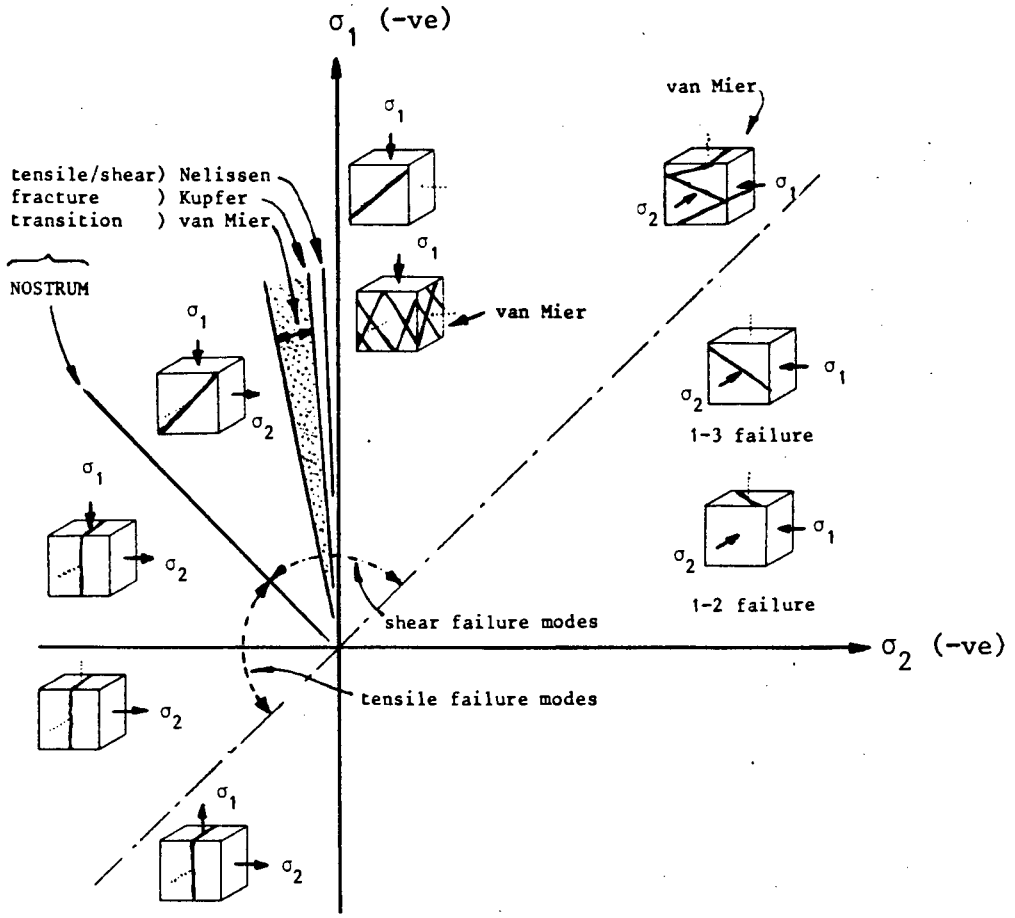

Figure 6.8 : Shear-splitting mode transition

6.3.4 Uniaxial tension

As the load-paths change from tension-compression to pure uniaxial tension, the predicted behaviour remains the same. Thus pure splitting modes (φ = 0°) are predicted with the onset of localization being at

the peak. These predictions are consistent with the reported experimental data of Kupfer *et al* (1969), Nelissen (1972) and van Mier (1986), and the analytical results of Ortiz (1986).

6.3.5 Biaxial tension

Under biaxial tension loading paths, the method predicts localization (Table 6.3). Localization occurs at the peak in the form of separation bands ($\Psi = 0$). For σ_1/σ_2 = 1/10 to 1/1.8 , the separation band is perpendicular to the principal tensile stress. However, for σ_1/σ_2 = 1/1 there is no preferred orientation of the failure band. These results are again consistent with the observations of Kupfer *et al* (1969) and Nelissen (1972). The analytical results of Ortiz (1986), fail to capture this behaviour. Ortiz reports that no localization is observed, with distributed damage being the cause of failure.

Test type	σ_1/σ_2	ϕ degrees	Ψ degrees	Model
Biaxial Tension				
	1/10	0	0	p–σ
	1/1.8	0	0	p–σ
	1/1	no preferred orientation		p–σ

Table 6.3 : Biaxial tension results

6.3.6 The onset of localization

From the numerical results, one can observe that for shear type failure modes ($\Psi = 90^\circ$) , localization occurs at or after the peak, whilst for splitting or separation modes ($\Psi = 0^\circ$) localization always occurs at the peak. These results are shown graphically on the $\sigma - \epsilon$ curve in Figure 6.9.

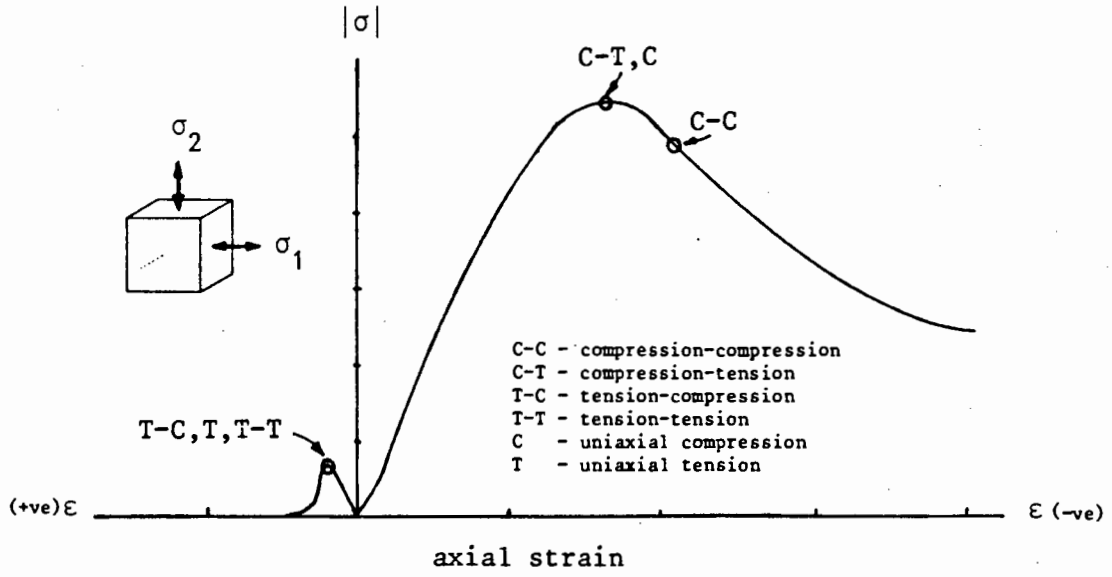

Figure 6.9 : The onset of localization

Since splitting modes are the result of tensile load paths, and shear modes result from predominantly compressive load paths, it is seen that the damage model predicts localization at the peak for materials subjected to tensile loads.

6.4 Localized Failure Modes in Norite

For these analyses, the calibration for norite was used for the damage model. The Stavropoulou (1982), Bieniawski (1967) and Hallbauer *et al* (1973) experimental data is used in this section. Hallbauers' work was on quartzitic rock, but was used because it provides data on the localization process.

Uniform triaxial tests were performed, for which a single 4-noded axisymmetric element with a single gauss point was used. This provided a uniform state of stress and deformation. The compression (or

tension) was provided by means of displacement control of the ends, and a confining pressure was also applied. The resulting uniform stress field thus simulated a typical material point. The tests ranged from hydrostatic compression to uniaxial tension.

6.4.1 Norite uniform triaxial analysis results

The results are tabulated in Table 6.4, and show that in the hydrostatic compression test, no localization was detected. This result was expected since under hydrostatic compression norite behaves elastically for the calibration used in this work.

Test type	$\sigma_1/\sigma_2/\sigma_3$	ϕ degrees	ψ degrees
Uniaxial Compression	-345/0/0	45.1	84.7
Triaxial Compression	-410/-10/-10	45.4	86.4
	-490/-25/-25	45.6	87.9
	-605/-50/-50	46.1	89.3
	-709/-75/-75	46.2	90.0
	-806/-100/-100	46.3	89.5
	-990/-150/-150	46.3	89.0
	-1160/-200/-200	46.5	88.8
	-1325/-250/-250	46.5	88.8
Hydrostatic Compression	hydrostatic	no localization	
Uniaxial Tension	18.5/0/0	90	0

Table 6.4 : Norite uniform triaxial results

In the triaxial tests, the confining pressure ranged from 0 to -250 MPa. In all the problems, localization was detected in the form of shear bands. The orientation of these bands ranged from $\phi = 45°$ to

46.5° and increased with increasing confining pressure. The mode of failure tended towards pure shear (ψ = 90°) as the confining pressure increased. The increase in confining pressure also had the effect of delaying the onset of localization.

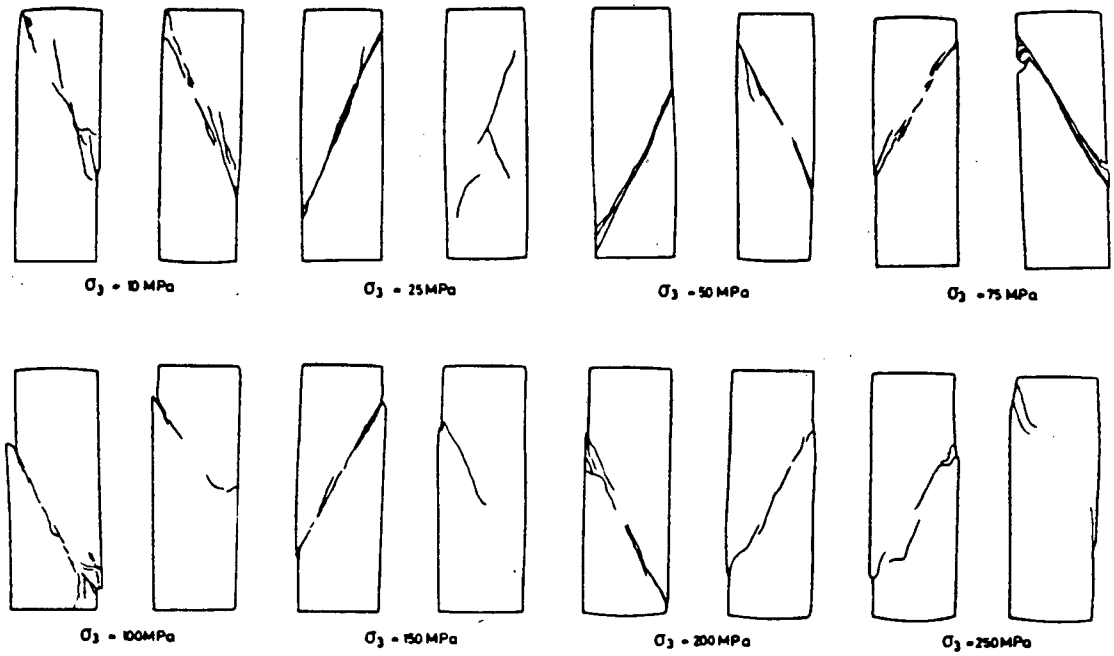

Figure 6.10 : Norite experimental triaxial tests (Stavropoulou (1982))

The experimental data of Stavropoulou (1982) shows that for similar laboratory tests, the orientation of the localized failure modes ranged between ϕ = 25° for low confining pressures to ϕ = 31° for high confining pressures (Figure 6.10). All the failures were due to shear bands. Results for quartzite, Hallbauer *et al* (1973), are typically the same as those for norite. Figure 6.11 shows localized failure typical of brittle rock materials.

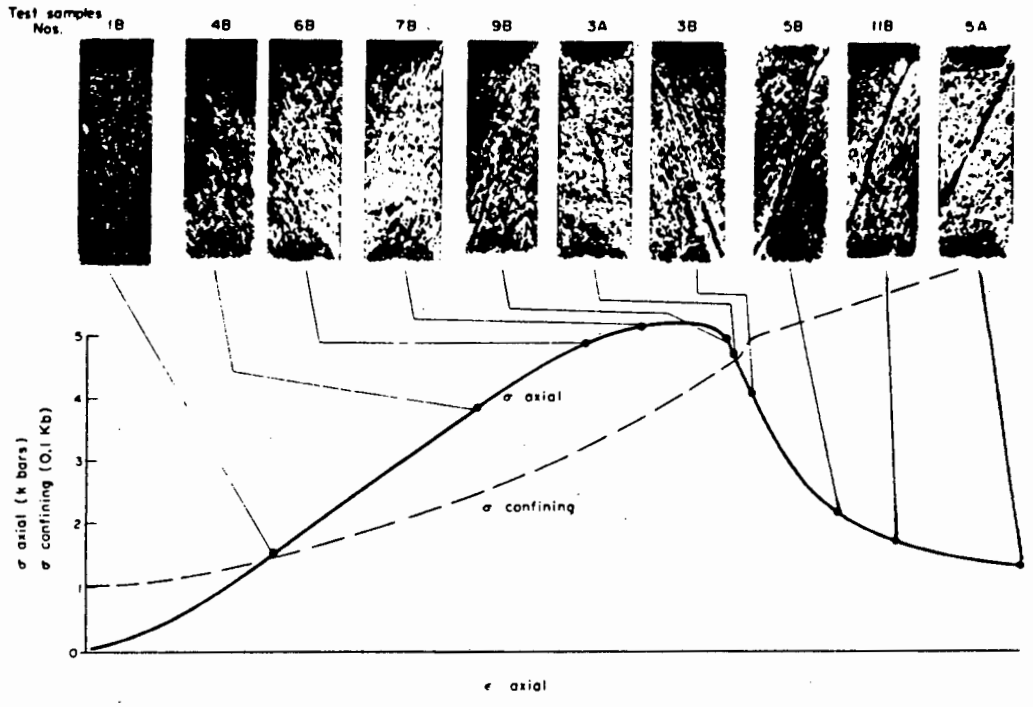

(a) Localization in quartzite (Hallbauer *et al* (1973))

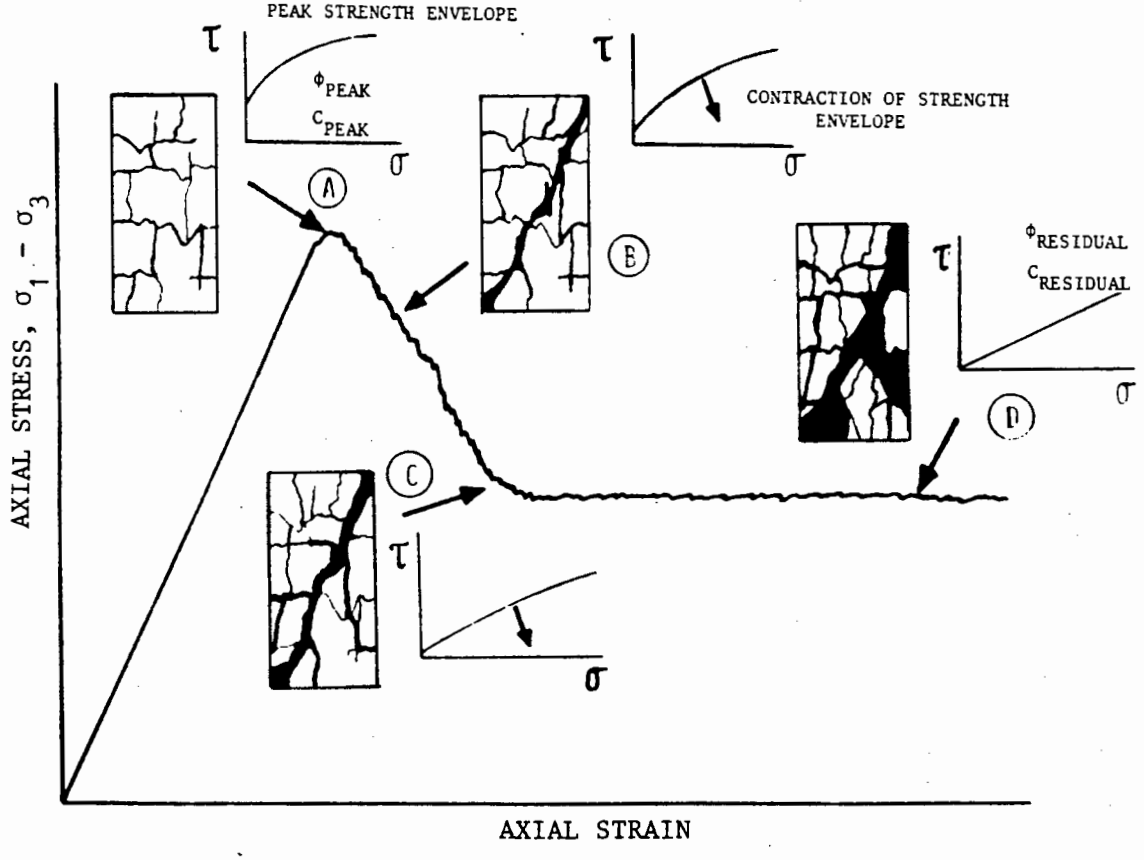

(b) Failure of brittle geologic materials (Sture and Ko (1978))

Figure 6.11 : Localization in rock materials

Under conditions of uniaxial tension, the NOSTRUM numerical analyses predict pure splitting modes (ψ = 0°) as observed by Stavropoulou (1982) and Bieniawski (1967).

Thus the damage model exaggerates the orientation of shear type failure modes, but correctly indicates the nature of these modes. It also correctly predicts behaviour under tensile conditions.

6.4.2 Parameter sensitivity

The aim of this study was to determine the sensitivity of the method to changes in the damage model parameters. In the calibration of the damage model, some approximation work had to be used to obtain values for some of the damage parameters. The most notable of these estimates was for the dilatancy parameters c_1 , c_2 and c_3 . Since these are directly related, it is necessary to vary each of them by the same degree for a sensitivity study. For this purpose, they were first doubled and then halved.The analyses used confining pressures ranging from 0 to - 25 MPa. The results are tabulated in Table 6.5 and the σ - ϵ response of the unconfined tests are plotted in Figure 6.12.

Test type	$\sigma_1/\sigma_2/\sigma_3$	ϕ degrees	ψ degrees
doubled c	uniaxial	42.2	74.9
	-410/-10/-10	43.2	78.4
	-490/-25/-25	43.7	81.2
halved c	uniaxial	46.3	90.0
	-410/-10/-10	46.9	89.0
	-490/-25/-25	46.7	88.4

Table 6.5 : Parameter sensitivity results for norite

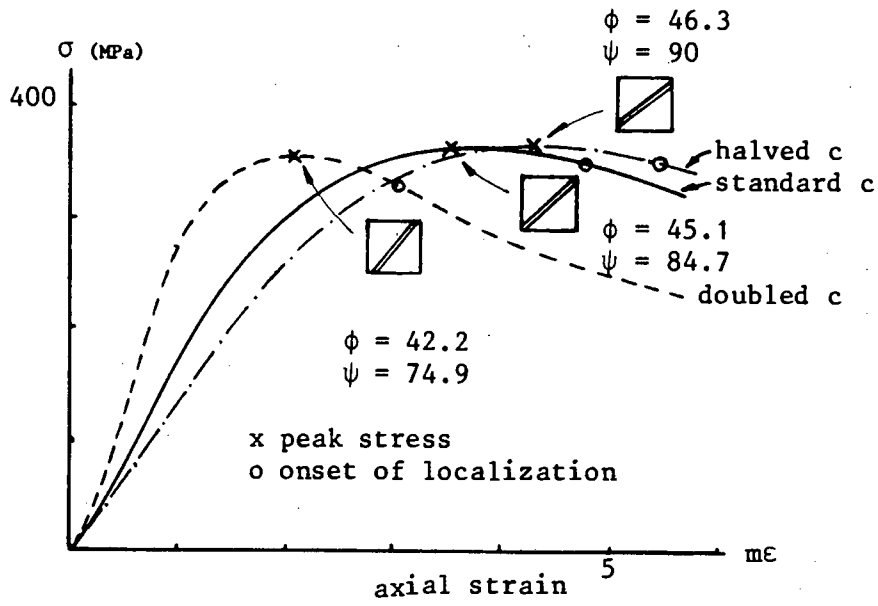

Figure 6.12 : Effect of the dilatancy parameters on the $\sigma - \epsilon$ curve

From the results it is evident that by doubling c , ϕ is reduced and the failure mode is less of a shear band ($\varphi = 75°$), whilst the opposite is true for halving c . The most notable effect is that by doubling the dilatancy parameters, the $\sigma - \epsilon$ curve is compressed. In the previous examples, it was evident that the predicted ϕ value was too large. Since we are trying to reduce ϕ , one might be tempted to use the above results and increase the dilatancy parameters. However, this would have the adverse effect of producing an unrealistic $\sigma - \epsilon$ response and thus the parameters appear to be realistically calibrated.

6.5 Localization in Norite Non-uniform Triaxial Tests

The rest of this chapter is devoted to non-uniform tests and boundary value problems. Here, non-uniform refers to the states of deformation and stress. In this section, the norite triaxial compression tests of

Stavropoulou (1982) are modelled by means of various axisymmetric finite element meshes. The finite element models make use of two lines of symmetry so that only a quarter model is necessary. Only the -200 MPa confining pressure tests were modelled here. The numerical tests used displacement control of the ends assuming perfect bonding between the ends and the loading plattens so as to induce the desired non-uniform deformation field.

The norite calibration was done by assuming uniform deformation behaviour in the laboratory tests. In reality, this is not the case and hence it is necessary to evaluate the effect of this assumption on the damage model predictions for the non-uniform tests. Mesh sensitivity effects were also investigated by using a crude mesh, discretized meshes (in the radial and/or axial direction) and an orientated mesh.

The numerical results are shown in Figures 6.13 to 6.16. Figure 6.13 shows the σ - ϵ response of the different models, and Figure 6.14 shows when the localization process occurs for the different meshes. Figure 6.15 shows the localization results for some of the meshes. The progression of localization with increasing axial strain as well as the orientation of the localized failure bands are shown here. By progression we mean the order in which the gauss points localize. In all tests, the method predicted shear band formation with an orientation of between 45° and 50°, compared with the reported values of 25° to 31°. Note that the $\underset{\sim}{m}$ vector is only shown in Figure 6.15(a), and shows that the failure modes are in shear. This vector has been omitted from the other results for clarity, and unless otherwise shown, all modes are in shear. The onset of localization occurred at

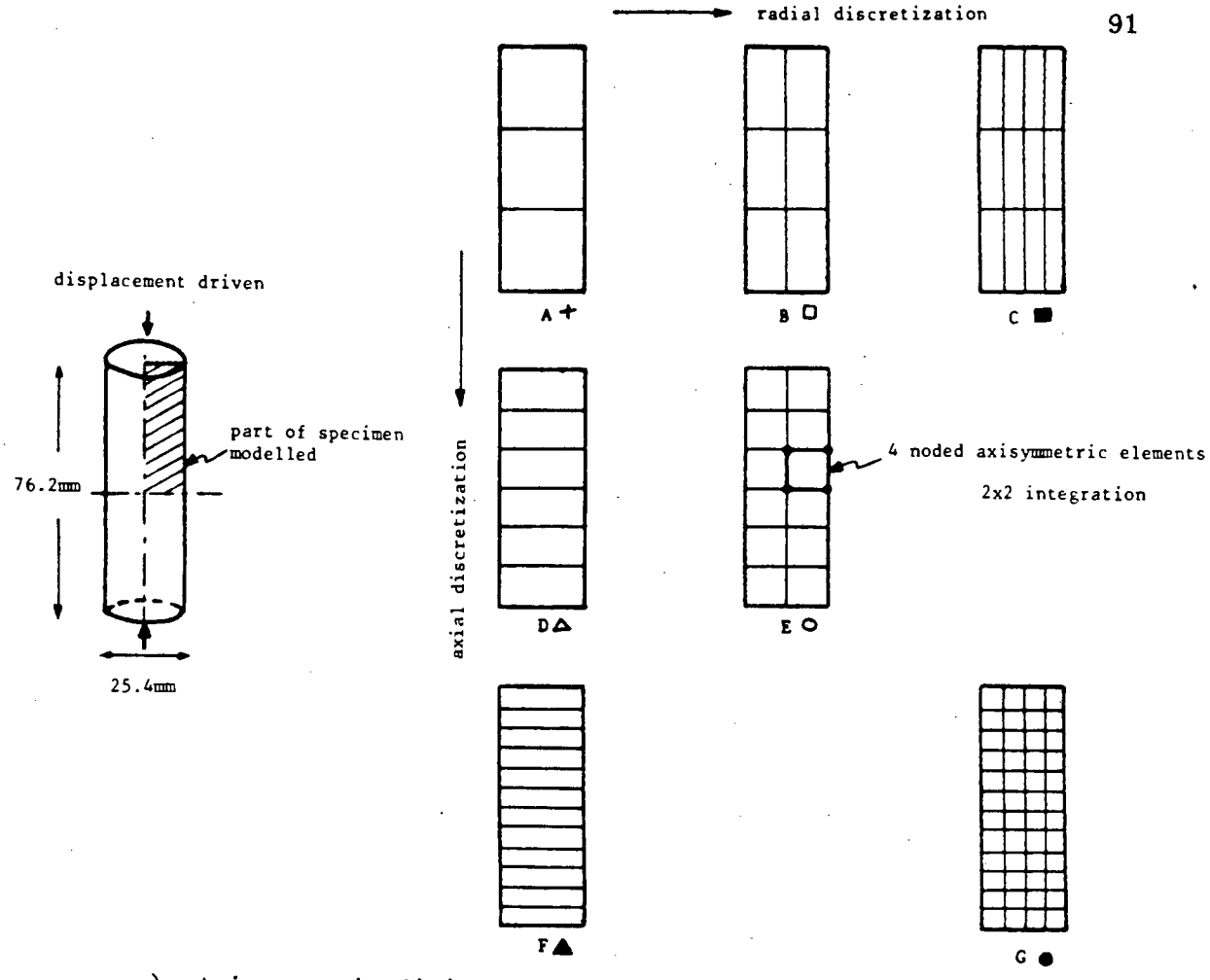

a) Axisymmetric finite element discretizations of the triaxial test specimens

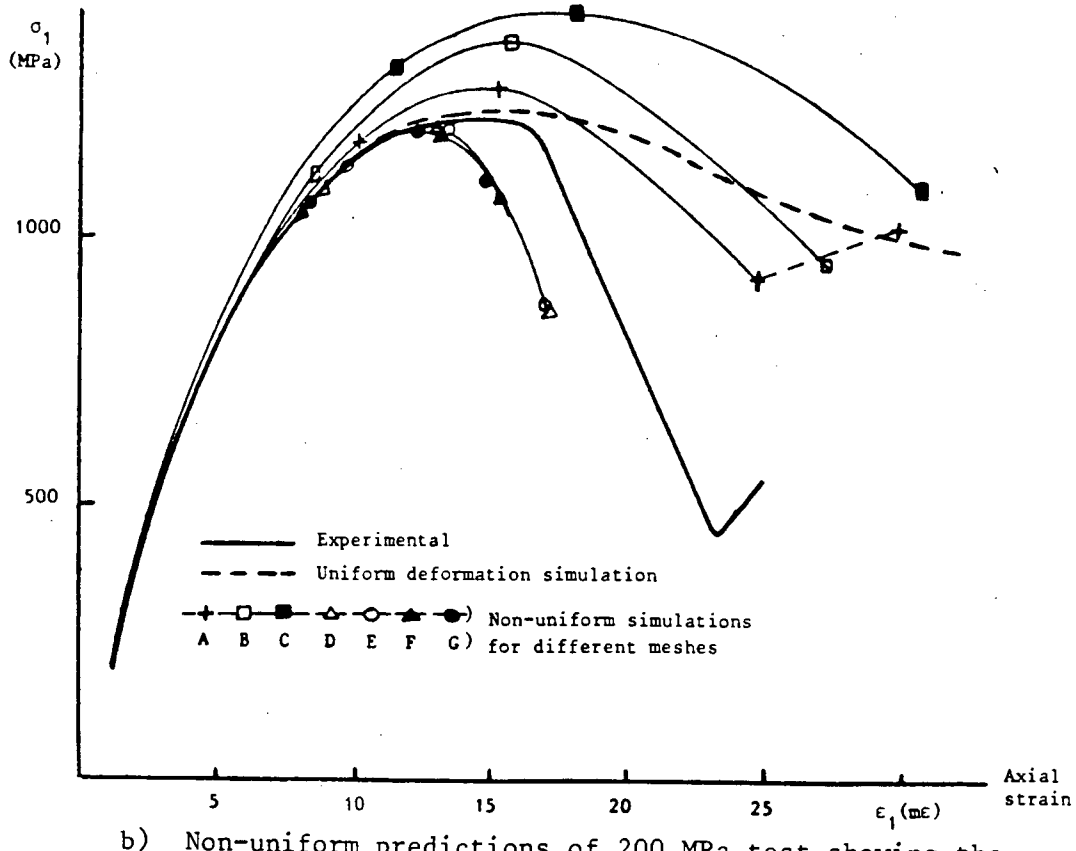

b) Non-uniform predictions of 200 MPa test showing the onset and completion of the localization process

Figure 6.13 : Non-uniform triaxial tests on norite showing the models and their response - Resende (1986)

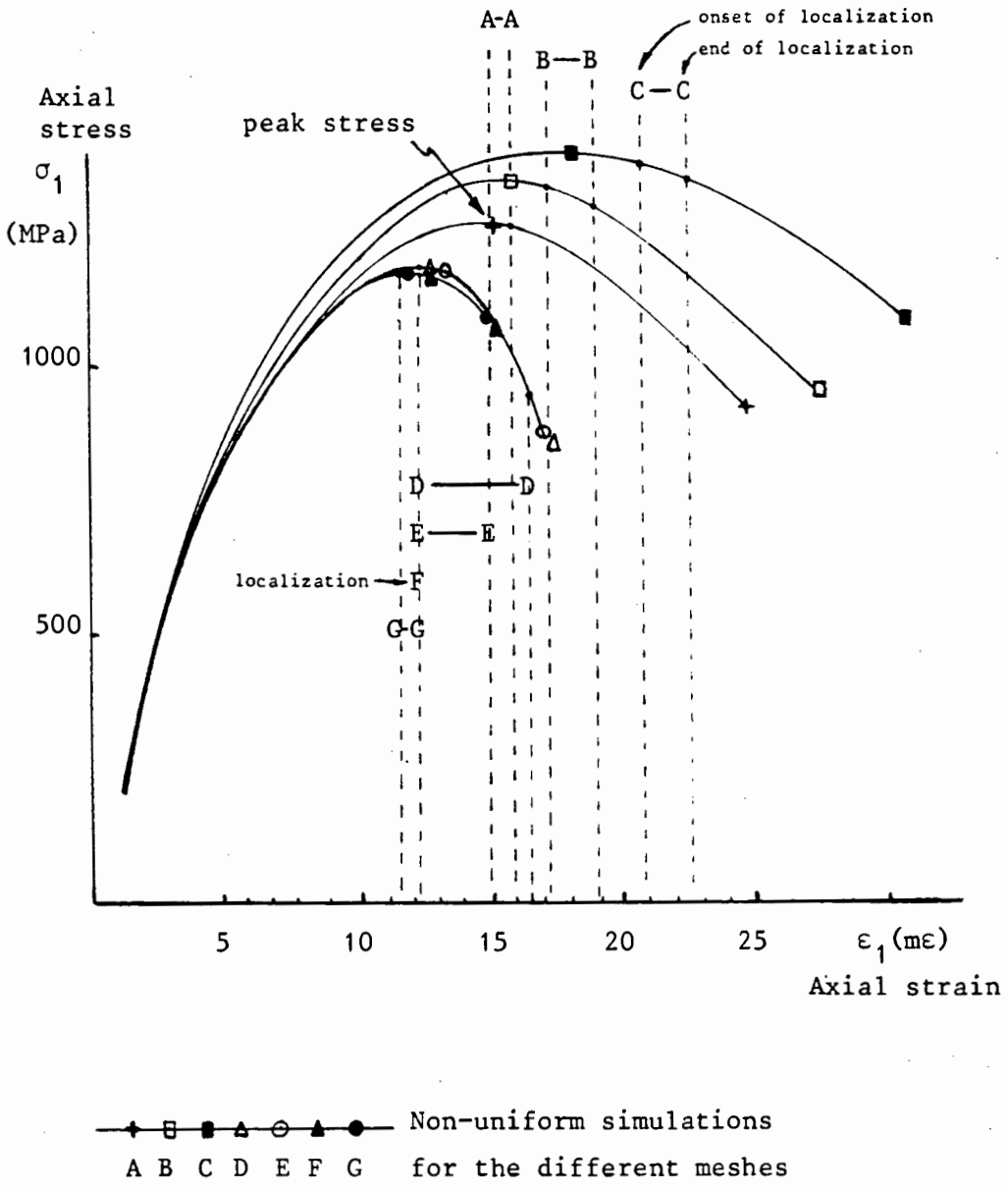

Figure 6.14 : Non-uniform triaxial tests on norite showing the predicted onset and completion of localization of the gauss points

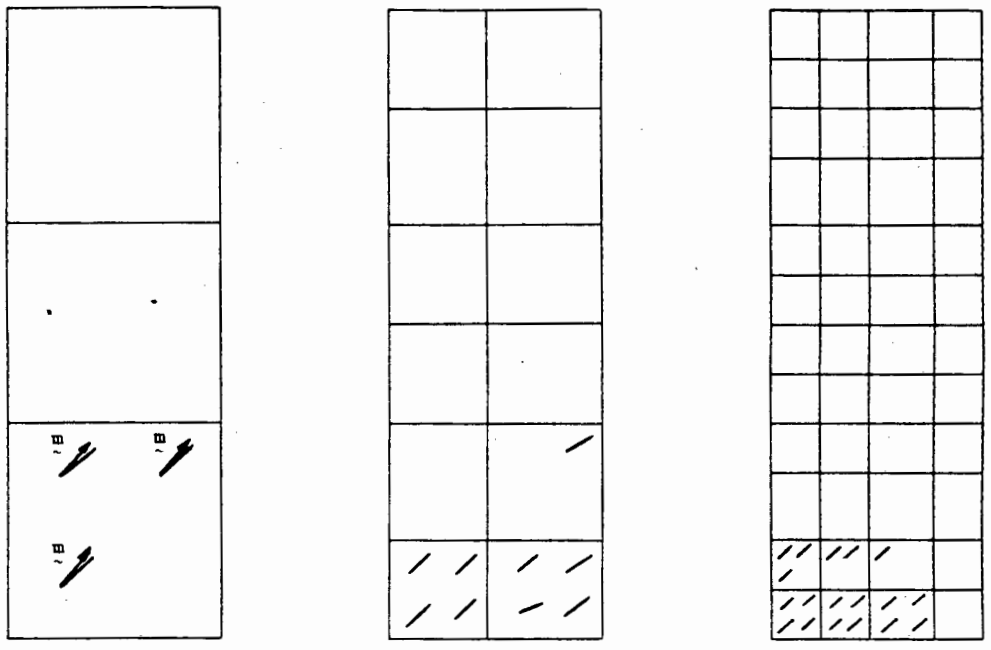

a) Localized failure band orientation
(note : left hand plot also shows $\underset{\sim}{m}$)

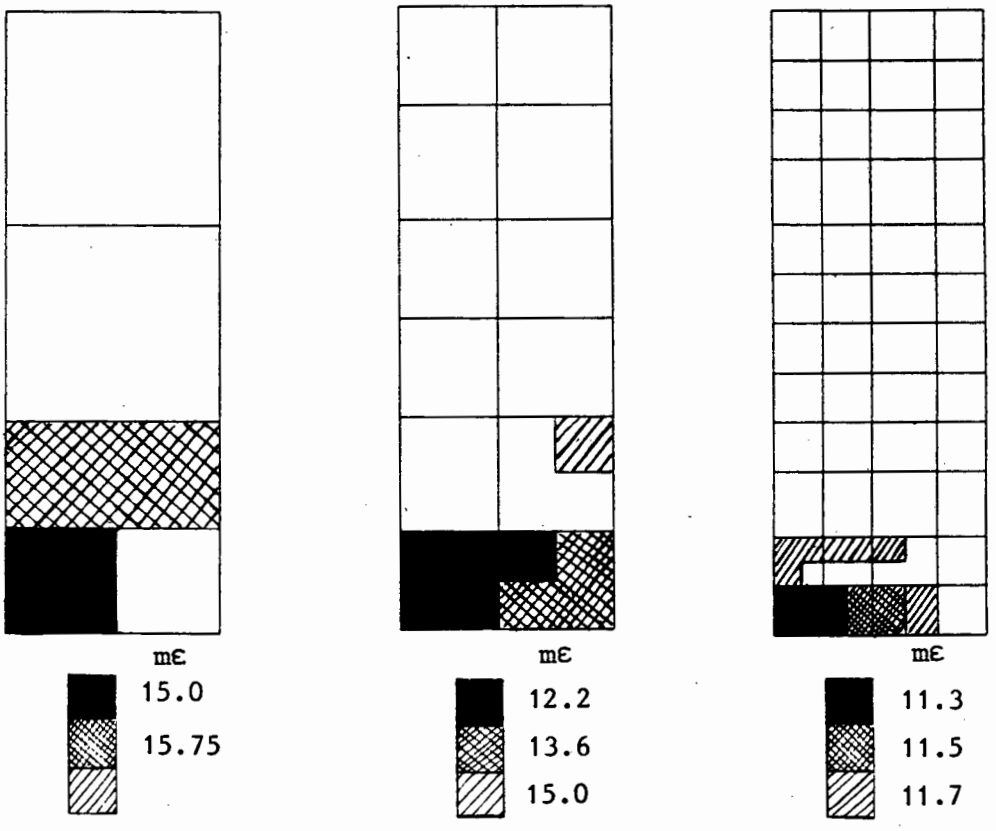

b) Progression of gauss points showing localized failure with increasing axial strain

Figure 6.15 : Localized failure mode results for meshes A,E,G

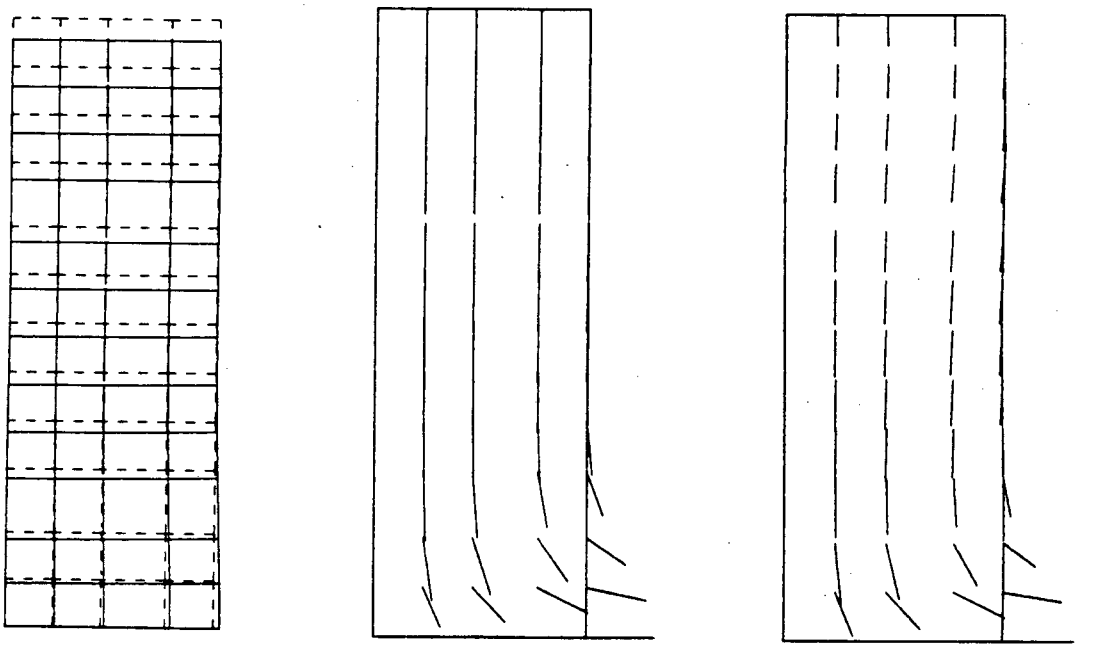

---- original mesh
——— displaced mesh

a) Displaced mesh after all gauss points have localized
mε = 11.7

b) Velocity vectors at the onset of localization
mε = 11.3

c) Velocity vectors after localization, showing unloading in upper half of model (different scale to (b))
mε = 11.7

Figure 6.16 : Non-uniform triaxial tests, mesh G, showing displaced mesh and velocity vectors

or after the peak and the process finished soon afterwards. These results are similar to the uniform tests in section 6.4, and all the same comments apply here. It can also be seen how localization follows the mesh discretization; this is a result of using isoparametric elements. Many researchers have noted that isoparametric elements tend to yield mesh sensitive results, de Borst (1986), and are also unable to capture highly localized deformation patterns. The results obtained show that the order in which the gauss points localize is sensitive to the mesh, Figure 6.15(b), but that the predicted orientation, mode, and onset of localization appear to converge with increased mesh refinement, Figures 6.14, 6.15(a). This can be seen for meshes E and G. Figure 6.16 shows the velocity vectors (i.e. change in deformation) and the displaced shapes for the fine mesh. It is interesting to relate the velocity vectors to the process of localization. These show quite clearly how the deformation changes from a distributed one to a localized one with unloading occurring outside the shear band.

Figure 6.17 shows an experimental observation of how the shear band forms. Localization first starts at the centre, microcracks coalesce and finally form a shear band. This observation by Hallbauer *et al* (1973) is consistent with the numerical results shown in Figure 6.15 .

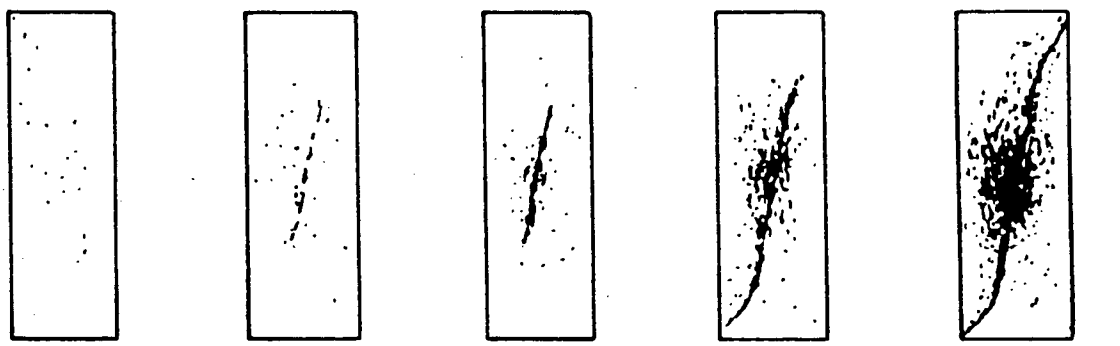

Figure 6.17 : The localization of damage in a quartzite specimen Hallbauer *et al* (1973)

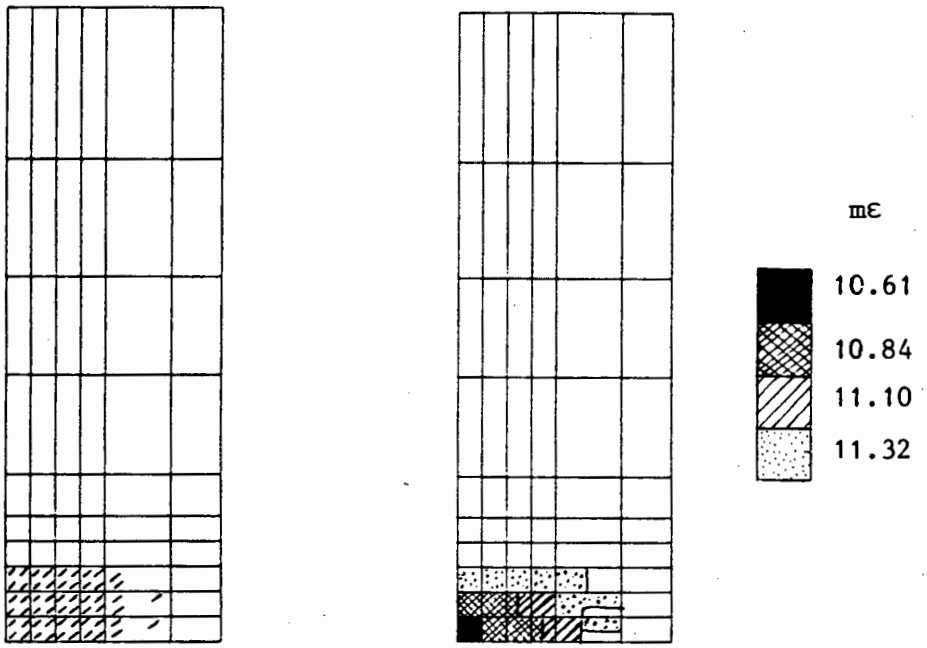

a) Refined mesh - 60 elements

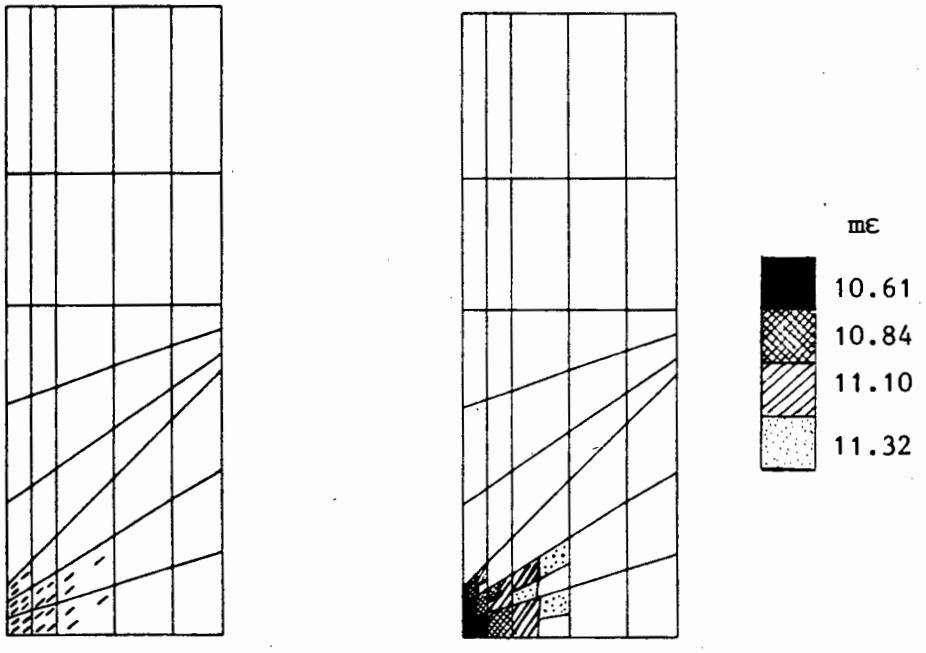

b) Orientated mesh - 40 elements

Note : only the orientation of the shear bands are shown

Figure 6.18 : Comparison of refined and oriented mesh results

What also becomes apparent from the different discretizations, is that a very fine mesh is required for localization studies, and it seems that even the finest mesh used here was not fine enough. However, due to computational limitations, a finer mesh was not attempted. To compensate for limitations of isoparametric elements, an orientated mesh was designed to encourage localization in the observed way. The results, together with the mesh, are shown in Figure 6.18. Two meshes were designed, both with a similar degree of refinement in the region where localization is expected, but one with the elements orientated in the direction of the anticipated shear band.

The results predicted by the two meshes are similar. The progression of localization proceeds along the line of the elements, with the orientated mesh showing a slight improvement.

6.6 Localization in the Norite Pillar Problem

This real physical problem arises from the mining industry where rock pillars are left unexcavated so as to provide a support while excavating gold seams. This leads to the situation where unconfined rock pillars are compressed between two extensive rock masses. The Chamber of Mines Research Organization performed some laboratory tests on cylindrical norite pillar specimens. These tests were modelled using finite elements and the results given by Resende (1986). Here, two of these finite element tests are repeated and checked for the occurrence of localization.

The finite element studies consist of two different axisymmetric meshes for the same laboratory test configuration as shown in Figure 6.19 . The tests are displacement driven assuming perfect bonding between ends and loading plattens and no horizontal displacement in the surrounding rock boundaries is permitted.

The σ - ϵ response shown in Figure 6.19 reveals little mesh sensitivity, both models showing similar displaced mesh shapes and progression of localization. The localized failure modes are shown in Figures 6.20 and 6.21, and reveal that two different modes of failure are active. Spalling from the "roof" occurs first in the form of splitting modes, following which, shear band failure occurs across the pillar. Once again localization tends to follow the element layout, but this only appears to affect the splitting modes. The progression of localization is also shown in Figures 6.20 and 6.21, and contours represent gauss points that have localized at the same values of axial strain.

Of major interest are the plots of the principal tensile stress vectors and velocity vectors in Figures 6.22 and 6.23 . These clearly show the coincidence of the orientation of the localized failure planes and orientation of the principle tensile stresses. This agrees with the observation by Hallbauer *et al* (1973) that macroscopic failure is more likely the result of tensile than shear processes. The velocity vector plots show how deformations become localized resulting in unloading outside the localized zones. They also show how localization of deformation first occurs in the roof and subsequently in the pillar.

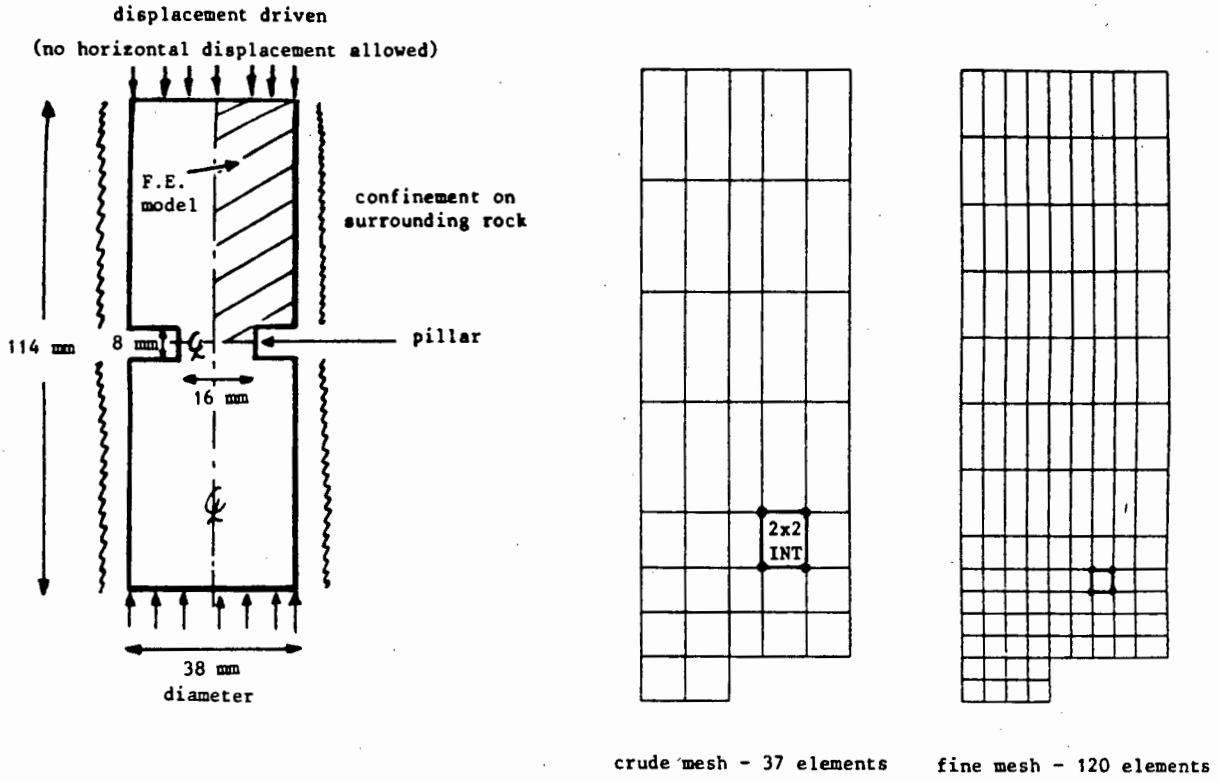

a) Norite pillar specimen and the axisymmetric finite element meshes

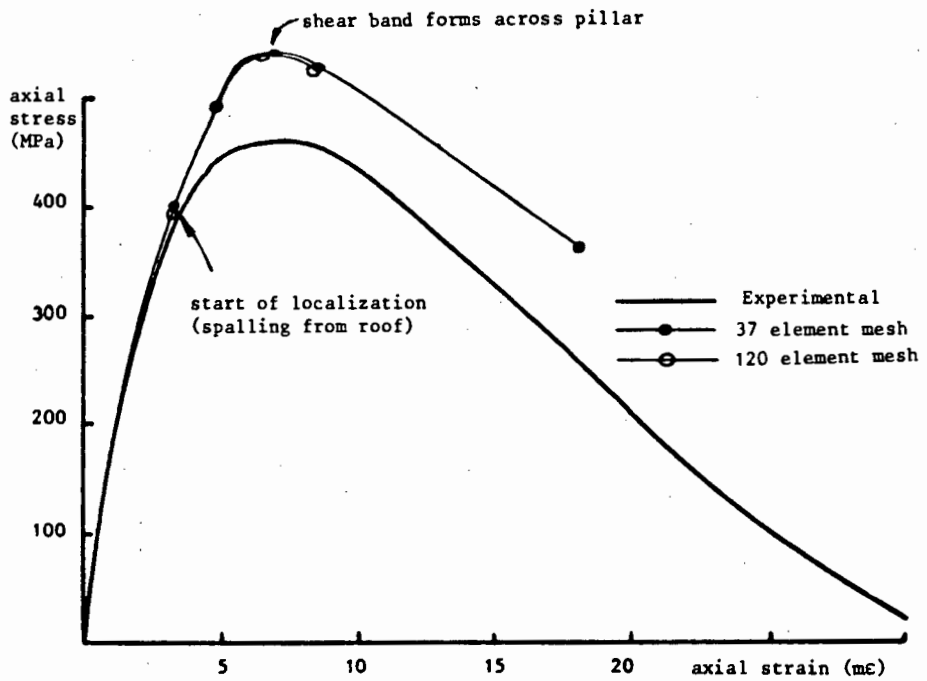

b) Response curves for pillar with rigid ring confinement

Figure 6.19 : Norite pillar test showing the models and their response - Resende (1986)

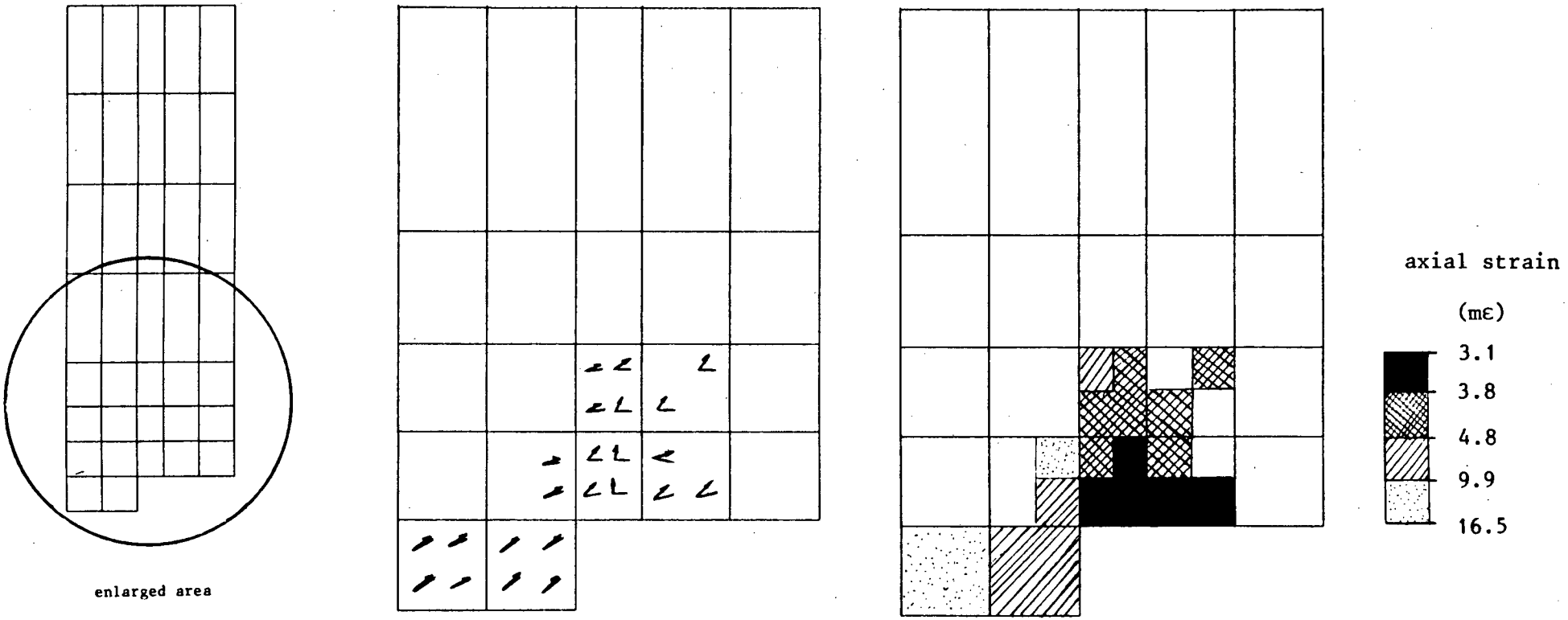

a) Axisymmetric mesh 37 elements

b) Orientation of localized failure bands and the $\underset{\sim}{m}$ direction vector

c) Progression of gauss points showing localized failure

Figure 6.20 : Norite pillar, localized failure modes and progression of localization - coarse mesh

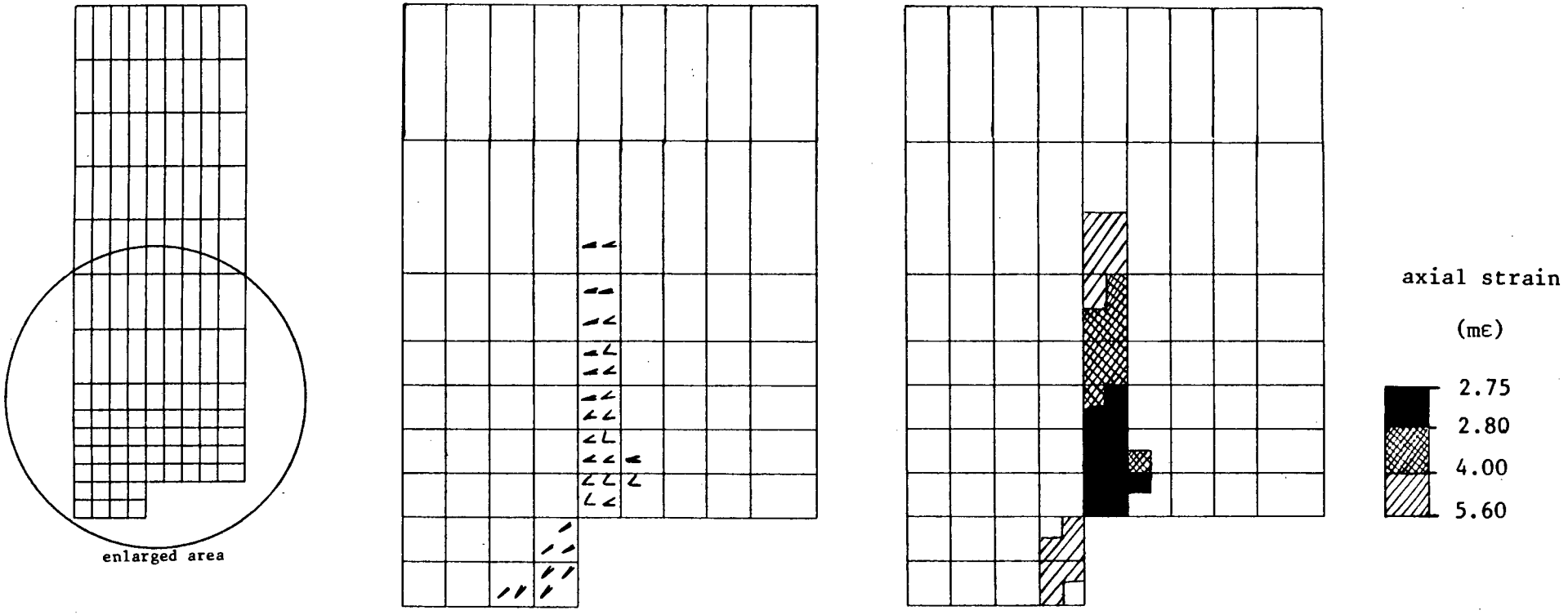

a) Axisymmetric mesh 120 elements

b) Orientation of the localized failure bands

c) Progression of gauss points showing localized failure

Figure 6.21 : Norite pillar, localized failure modes and progression of localization - fine mesh

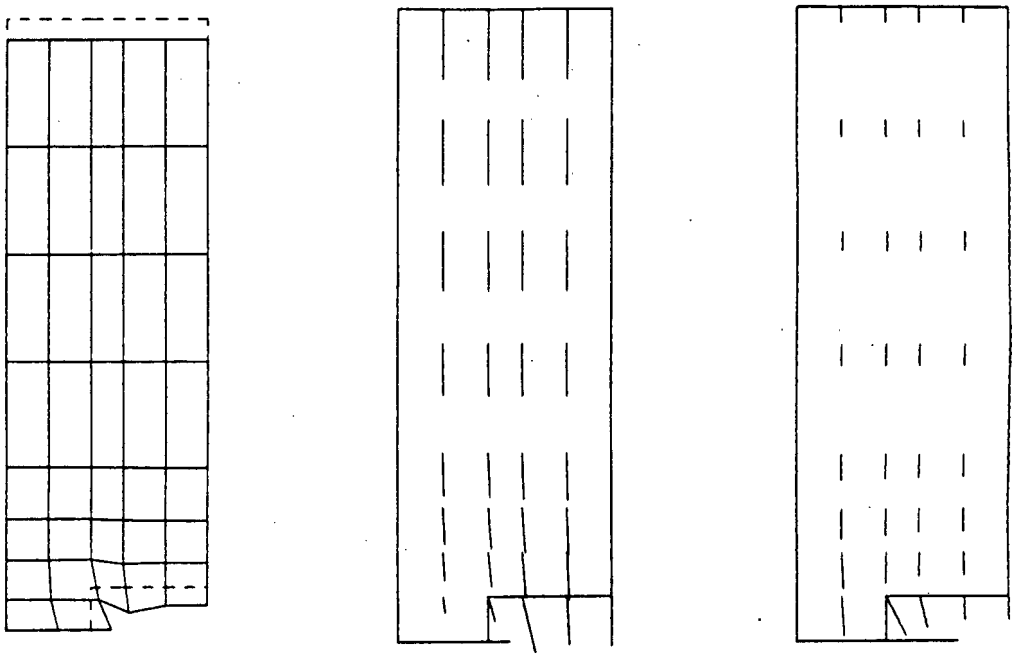

a) displaced mesh

b) velocity vectors at the onset and completion of localization

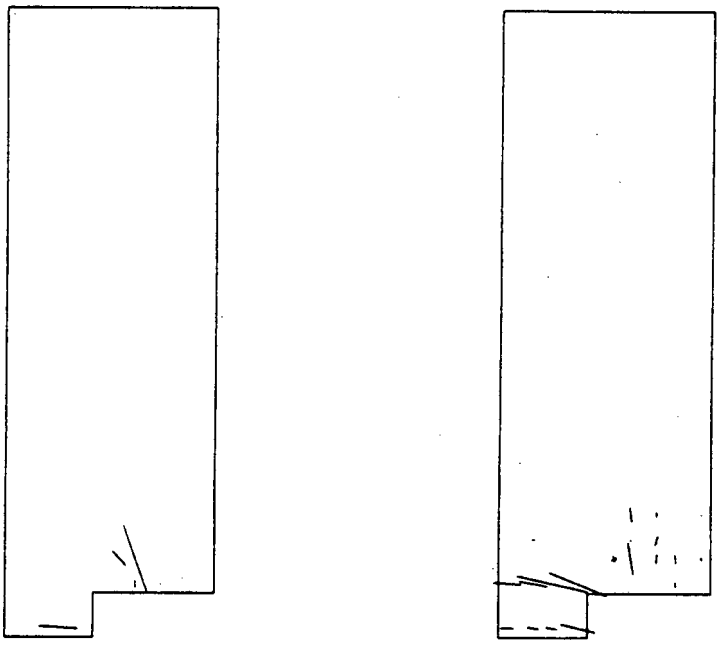

c) principal tensile stress vectors

Figure 6.22 : Norite pillar, deformed mesh, velocity vectors and principal tensile stress vectors - coarse mesh

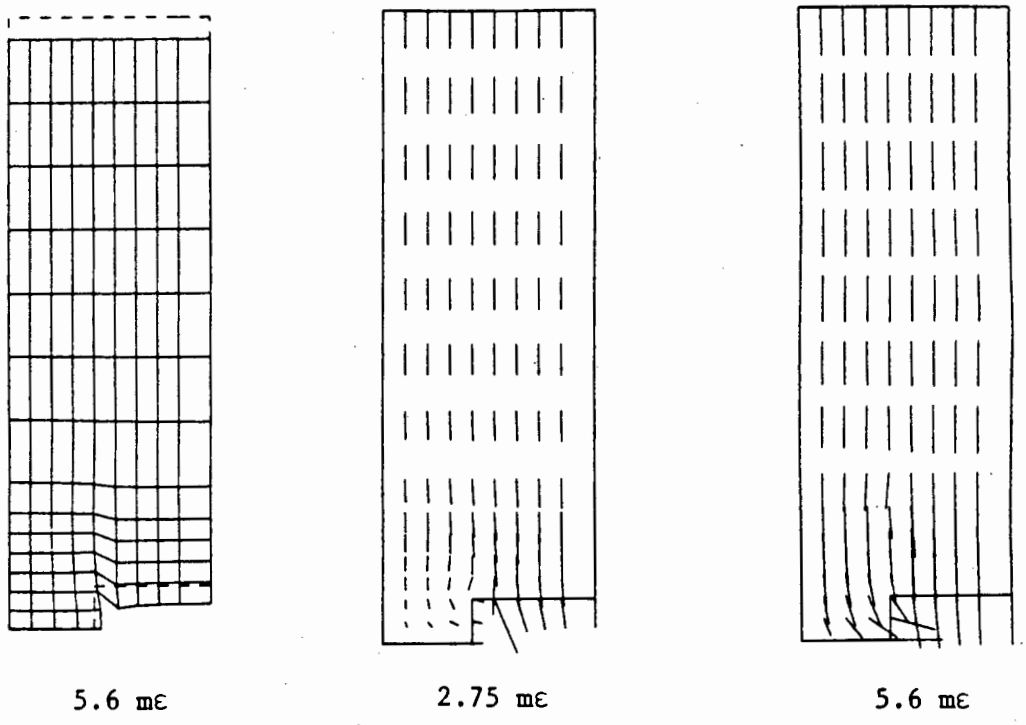

5.6 mε 2.75 mε 5.6 mε

a) displaced mesh

b) velocity vectors at the onset and completion of localization

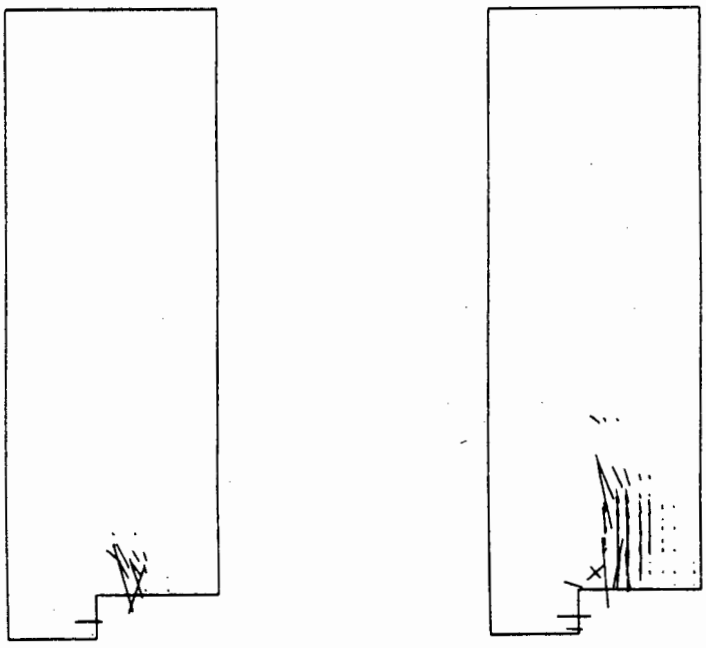

2.75 mε 5.6 mε

c) principal tensile stress vectors

Figure 6.23 : Norite pillar, deformed mesh, velocity vectors and principal tensile stress vectors - fine mesh

6.7 Localization in the Norite Borehole Spalling Problem

This is another problem that arises in the mining industry. In the mines, boreholes are drilled into the highly stressed rock for the installation of stress monitoring equipment. However, spalling often occurs making it impossible to use these boreholes, but the extent of the spalling can be used to estimate the stress levels of the surrounding rock. The Chamber of Mines Research Organization investigated the problem by experimenting with plain strain laboratory tests on norite specimens under various combinations of vertical and horizontal stress (σ_v and σ_h). Resende (1986) made finite element simulations of these experiments using the damage model in NOSTRUM.

The intention was to investigate the shape and size of the spalled zone so as to improve the stress-level estimation techniques. In this work, the focus is on spalling as a localization phenomenon and the aim was to determine the nature of the spalling as well as to assess the performance of the damage model.

Two different numerical tests were performed, both being reproductions of Resende's original tests. The first being the test with $\sigma_v/\sigma_h = 4/1$ and the second being $\sigma_v/\sigma_h = 1/1$. Figure 6.24 shows the borehole model which was a plain strain, quarter symmetrical model using 120 four-noded isoparametric elements.

The results show that the damage model does indeed predict spalling in the form of shear modes ($\varphi = 75°$) which causes a flaking of the borehole surface. The distribution, nature and progression of the

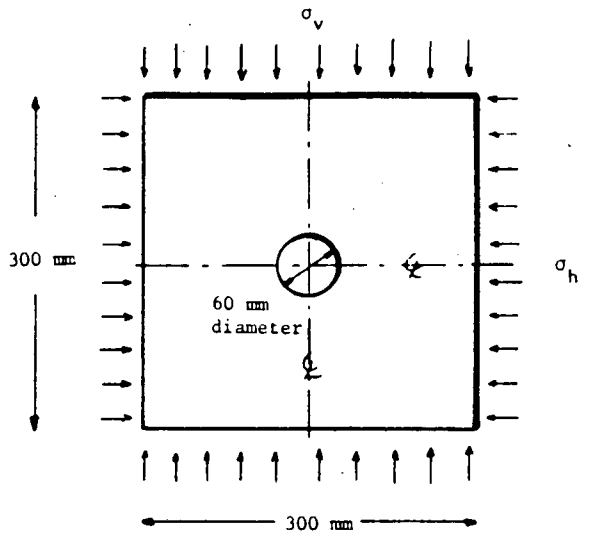

a) Borehole spalling experimental configuration

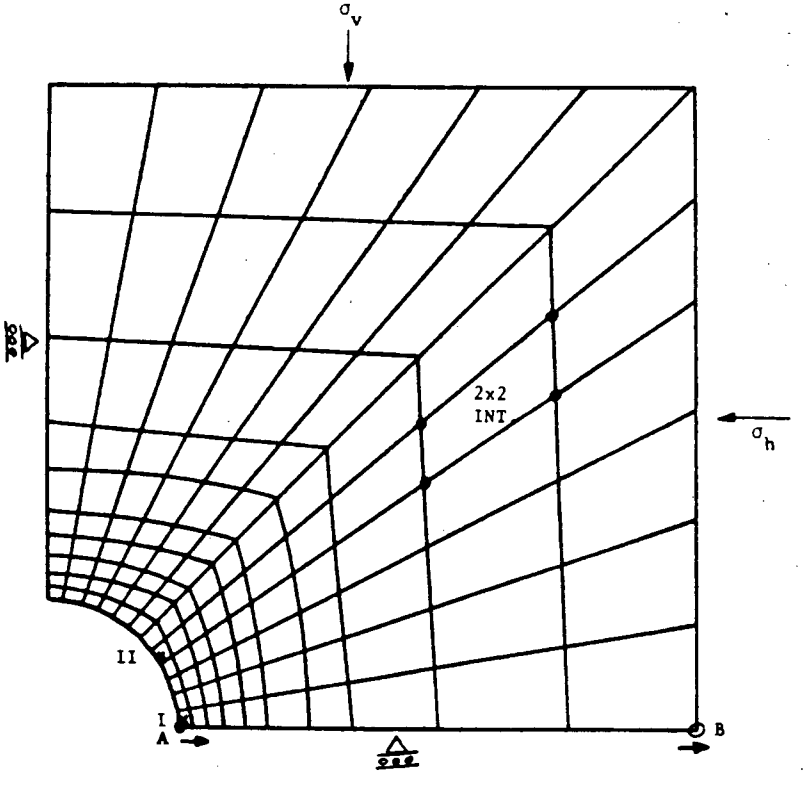

b) Finite element model consisting of 120 four-noded plane strain elements

Figure 6.24 : Norite borehole spalling problem, showing experimental and numerical setups - Resende (1986)

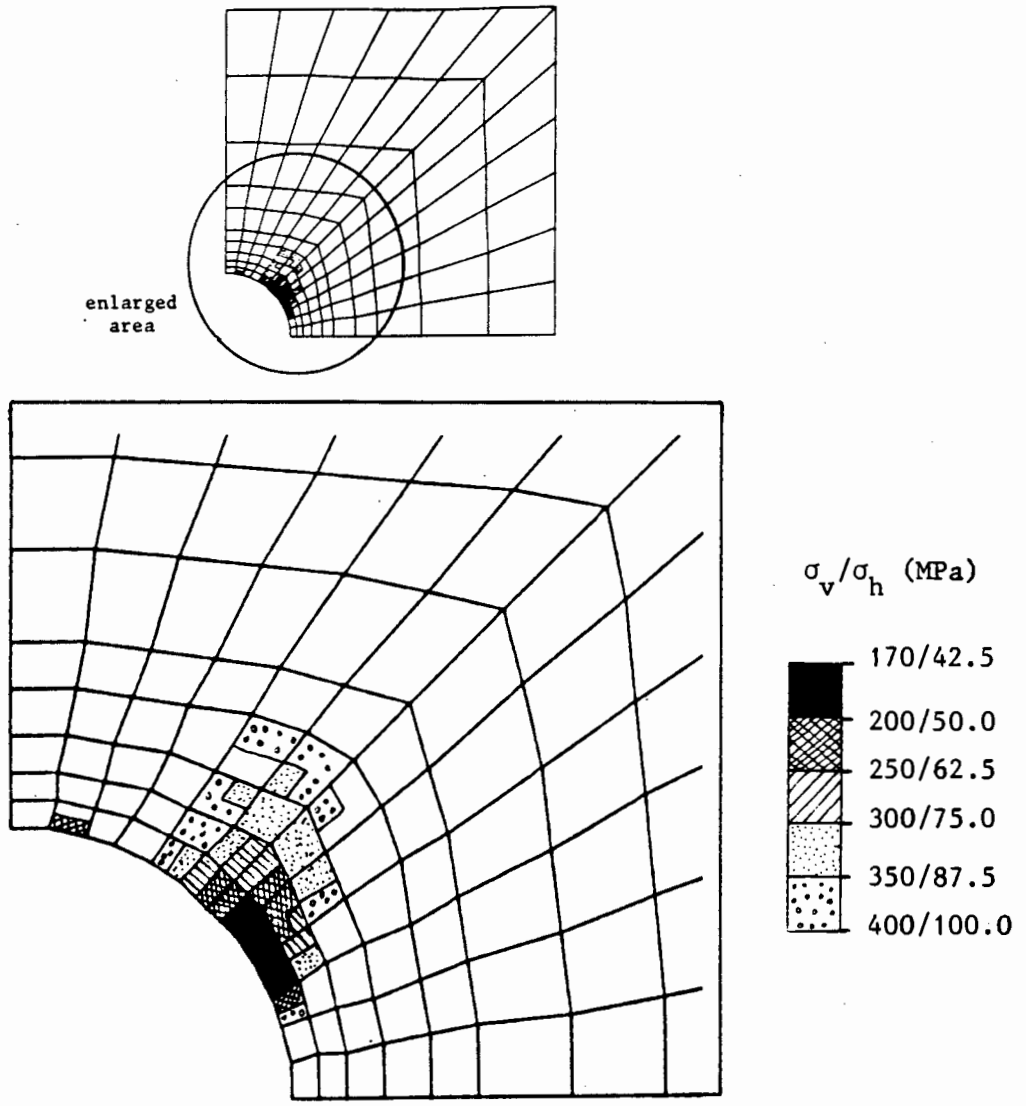

a) Progression of localization showing gauss points which have localized

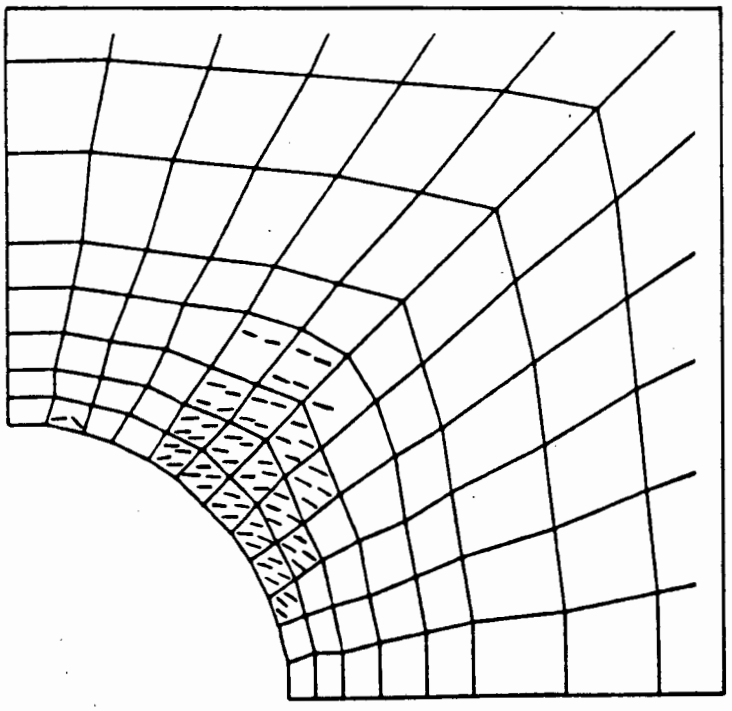

b) Localized failure band orientation

Figure 6.25 : Localization and localized failure modes in the borehole spalling problem, σ_v/σ_h = 4/1

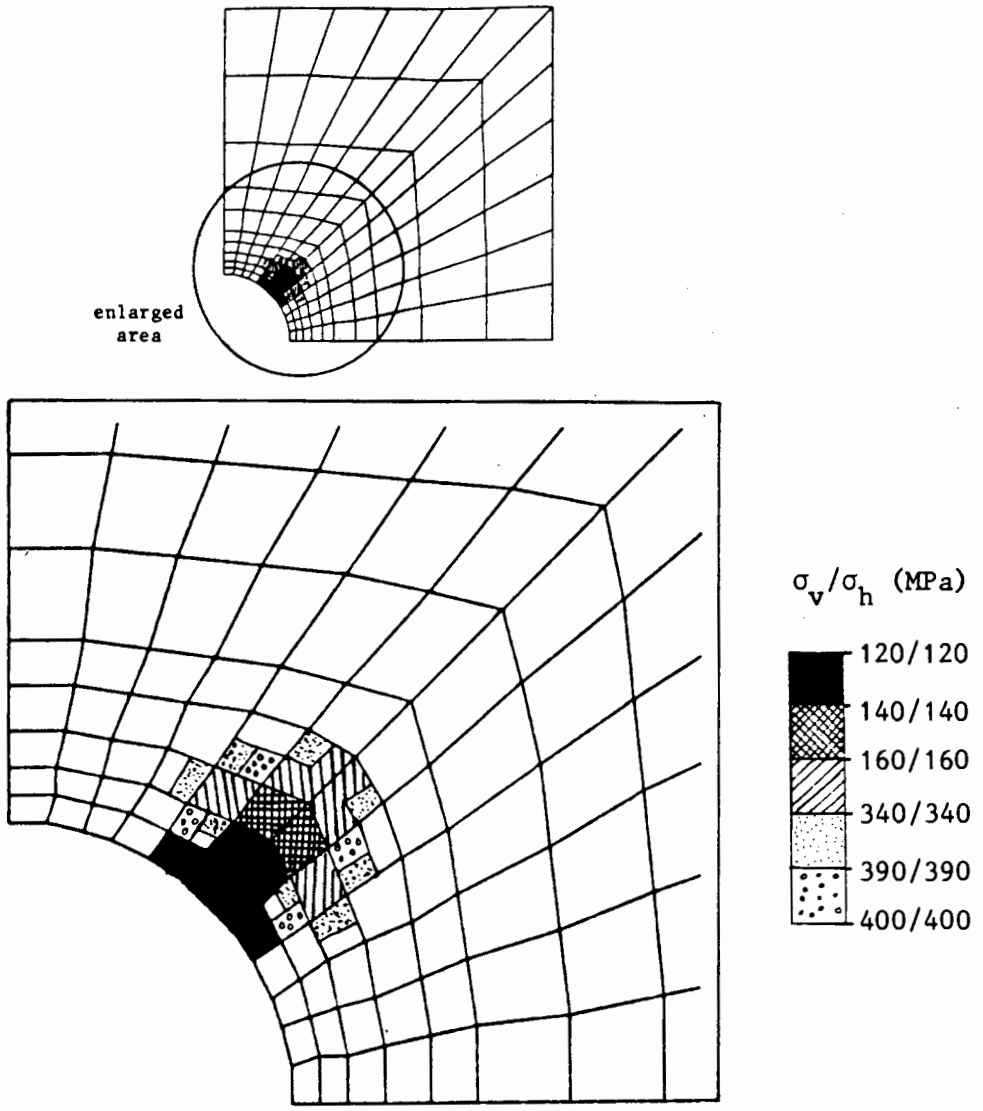

a) Progression of localization showing gauss points which have localized

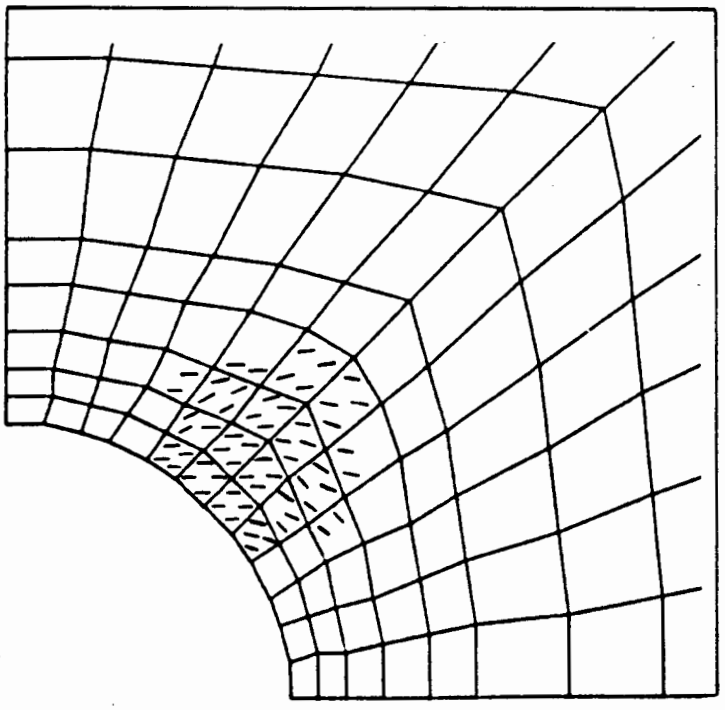

b) Localized failure band orientation

Figure 6.26 : Localization and localized failure modes in the borehole spalling problem, σ_v/σ_h = 1/1

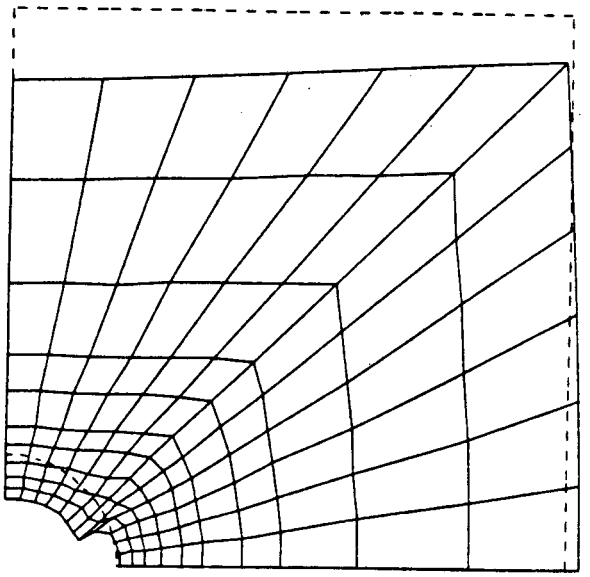

a) Displaced mesh at σ_v/σ_h = 370/92.5

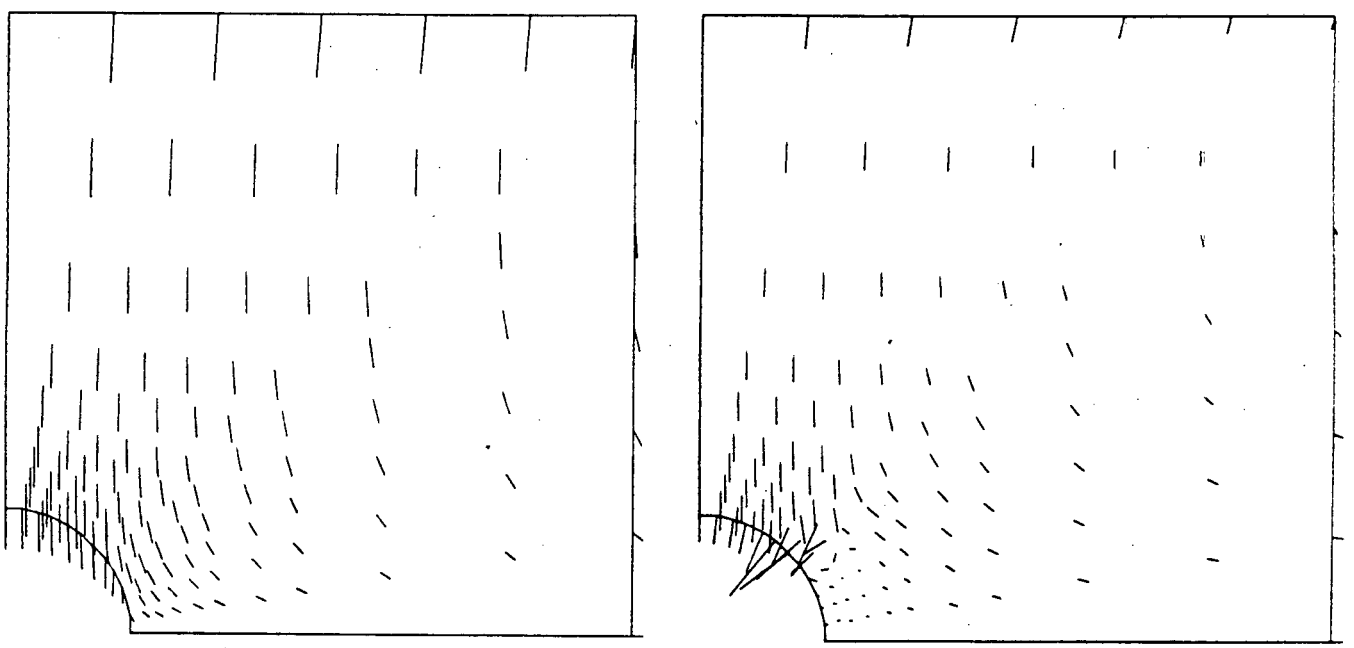

σ_v/σ_h = 170/42.5 σ_v/σ_h = 370/92.5

b) Velocity vectors at the onset and end of localization

Figure 6.27 : Displaced mesh and velocity vectors for the borehole spalling problem with σ_v/σ_h = 4/1

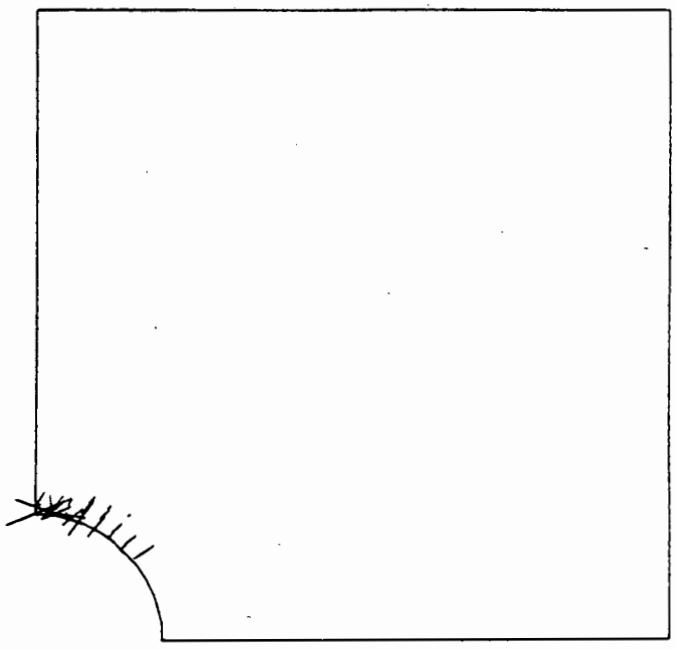

a) at the onset of localization, σ_v/σ_h = 170/42.5

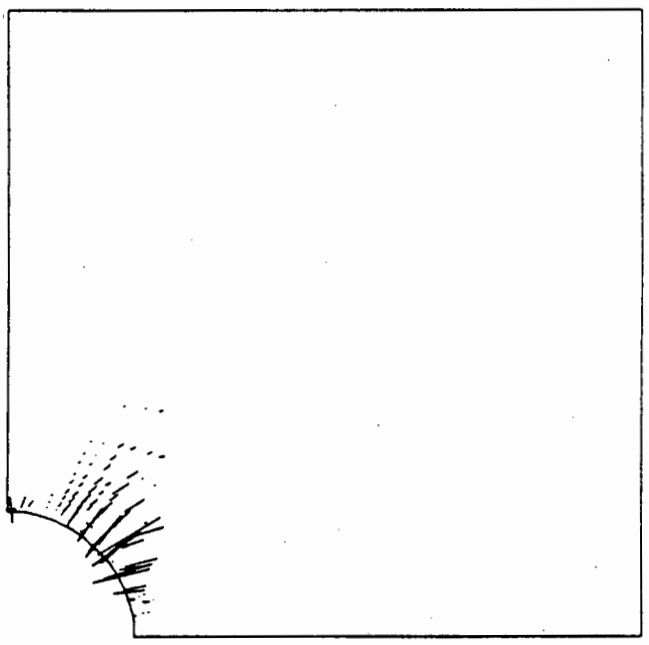

b) at the end of localization, σ_v/σ_h = 370/92.5

Figure 6.28 : Principal tensile stress vectors for the borehole spalling problem with σ_v/σ_h = 4/1

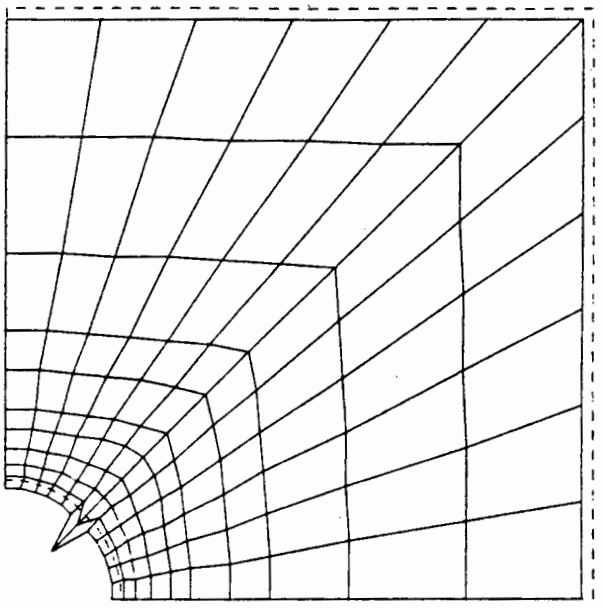

a) Displaced mesh at σ_v/σ_h = 400/400

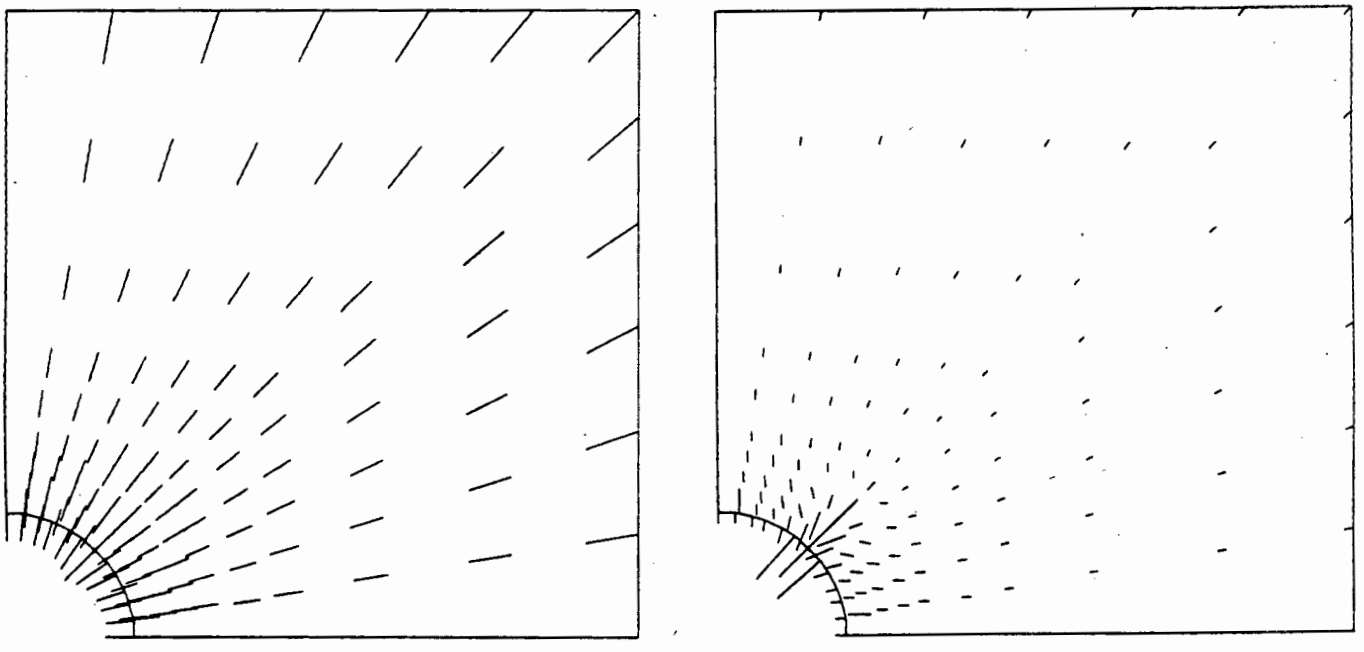

σ_v/σ_h = 120/120 σ_v/σ_h = 400/400

b) Velocity vectors at the onset and end of localization

Figure 6.29 : Displaced mesh and velocity vectors for the borehole spalling problem with σ_v/σ_h = 1/1

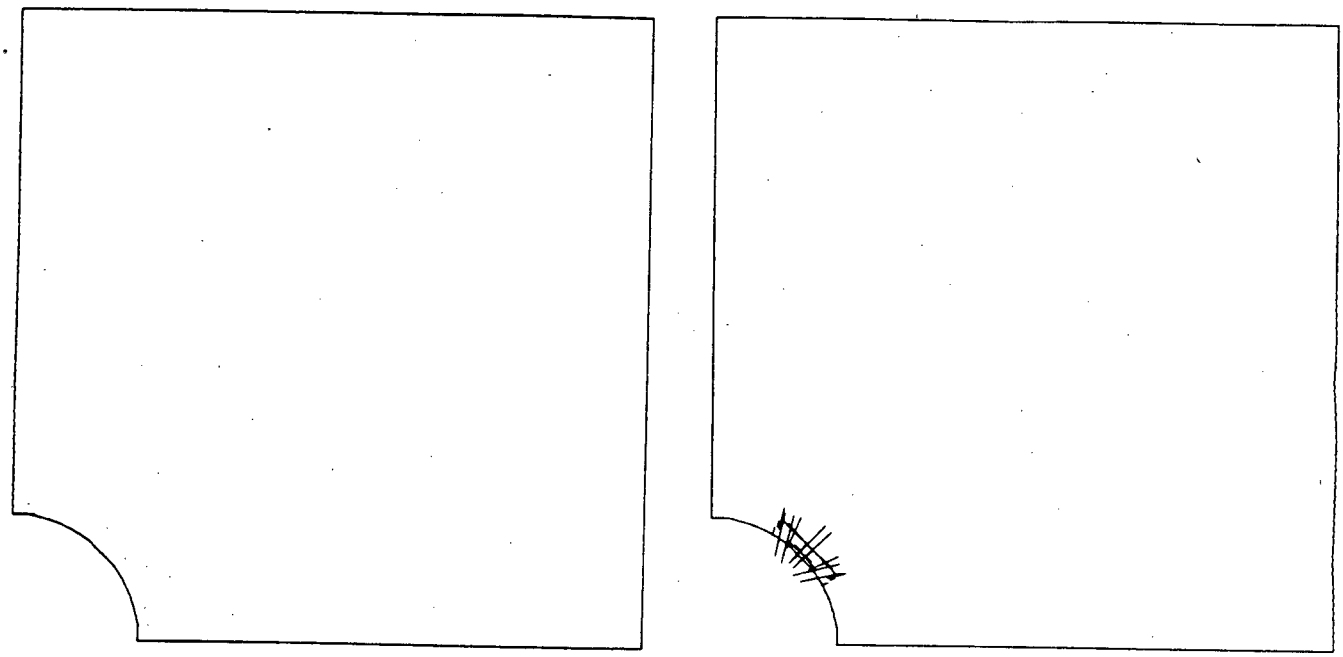

before, σ_v/σ_h = 120/120

after, σ_v/σ_h = 140/140

a) at the onset of localization

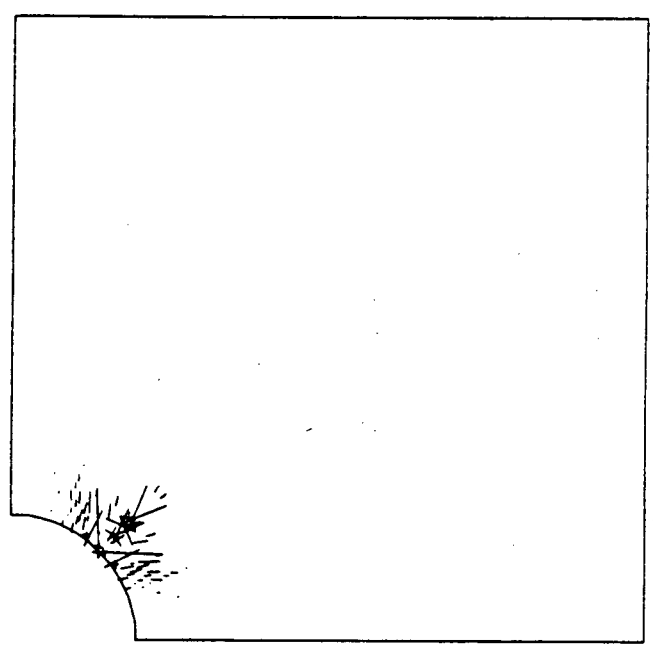

b) at the end of localization, σ_v/σ_h = 400/400

Figure 6.30 : Principal tensile stress vectors for the borehole spalling problem with σ_v/σ_h = 1/1

localized failure modes are shown in Figures 6.25 and 6.26 . These coincide with the areas of damage plotted by Resende (1986) and also agree with observations of the laboratory experiments. The spalling can be seen to be in the form of a wedge and is a result of the shear and damage mechanism. This is also evident in Figures 6.27 and 6.28 which show the principal tensile stress vectors. It is unclear at this stage why the spalling is more of a shear than a splitting process, since one intuitively expects splitting modes. However, Resende (1986) notes that spalling is caused by shear damage and shear failure which is supported by the above results namely $\psi = 75°$. The velocity vector plots of Figure 6.29 once again show how the deformations localize and show the need for a method to cope with the large strains within these failure zones.

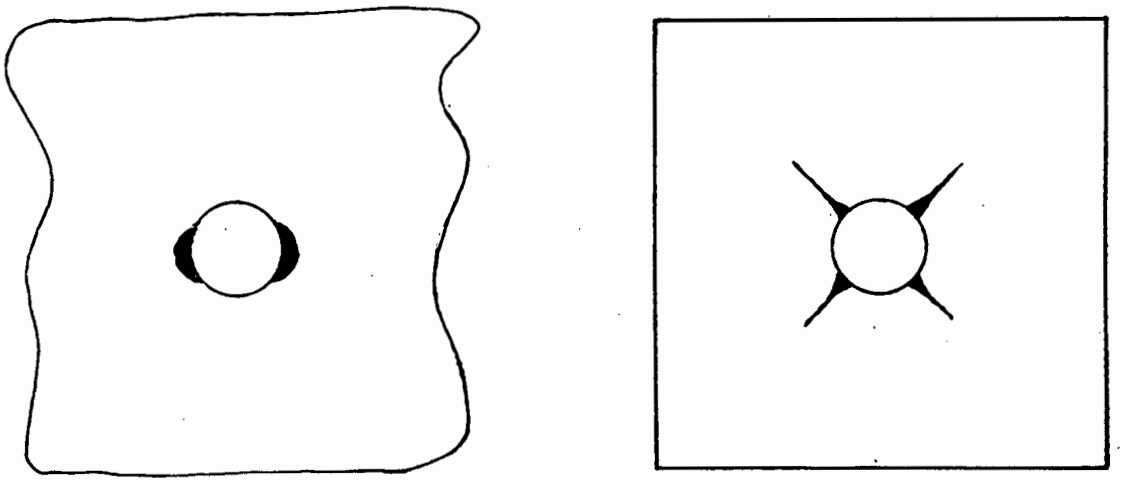

(a) Actual observations (b) Experimental observations

Figure 6.31 : Borehole spalling observations

Finally, it is interesting to compare the above results with the laboratory and the underground observations as depicted in Figure 6.31. From this it can be seen that the numerical results and laboratory experiments agree, but the underground observations show

that spalling occurs along a horizontal axis. The discrepencies here are believed to be due to time and temperature effects (i.e. of a visco-elastic creep nature). A further explanation is that of modelling effects. In the mine the borehole is surrounded by an extensive rock domain, whereas both the laboratory and numerical studies occur in a finite domain. Thus the numerical studies show good qualitative agreement with the laboratory observations.

CHAPTER 7

CONCLUSIONS

The method for the numerical analysis of the localization of deformations was reviewed and implemented in the finite element code NOSTRUM. The relevant isotropic continuous damage theory was reviewed and some aspects of bifurcation studies discussed. From the numerical results it was shown that the damage model provided a basis with which to analyse the localized failure modes of brittle materials. The method satisfactorily predicted the onset and the nature of the localized failure modes. However, the orientation of these modes was not accurately predicted. The reason for this is seen to be the damage model's assumption of a scalar, isotropic damage representation, whereas localization is the end result of directional, anisotropic damage processes. In the context of the present model, this is not seen as a problem, since the overall qualitative agreement was good. One must bear in mind that the damage model used was a simple one. However, if a quantitative agreement is required, the model would have to be upgraded to account for anisotropic damage.

The examples showed that localization techniques can be used to extend the predictive range of continuous damage theories by enabling discrete localized failure modes to be determined.

Problems were encountered with the inability of the isoparametric finite elements to resolve the deformation of the failure modes. The

propagation of these failure bands thus tended to follow the elemental discretisations. The solution to these problems is seen to be the use of enhanced elements. With this method, standard isoparametric elements are used up until the onset of localization, following which the enhanced elements would be used to resolve the discrete localization bands. For further improvement of results, adaptive mesh refinement could also be used.

Finally, one can note that for successful localization studies, a very fine mesh and very fine load increments must be used. These two factors result in localization techniques being very expensive in terms of computer time.

REFERENCES

ANAND, L and SPITZIG, W A
"Initiation of Localized Shear Bands in Plane Strain", J Mech Phys Solids, 28, 113-128, 1980.

BIENIAWSKI, Z I
"Mechanism of Brittle Fracture of Rock", Parts I, II and III, Int J Rock Mech Min Sci, 4, 395-430, 1967.

BIENIAWSKI, Z I, DENKHAUS, H G and VOGLER, U W
"Failure of Fractured Rock", Int J Rock Mech Min Sci, 6, 323-341, 1969.

CHANG, Y W and ASARO R J
"Lattice Rotations and Localized Shearing in Single Crystals", Arch Mech, 32, 369-388, 1980.

CHRISTOFFERSEN J and HUTCHINSON, J W
"A class of Phenomenological Corner Theories of Plasticity", J Mech Phys Solids, 27, 465-487, 1979.

DOUGILL, J W
"On Stable Progressively Fracturing Solids", J Appl Math and Physics, 127, 423-437, 1976.

DE BORST, R
"Nonlinear Analysis of Frictional Materials", PhD thesis, Delft University of Technology, Delft, 1986.

ELAM, C F
"Tensile Tests on Allow Crystals, Part I, Solid Solution Alloys of Aluminium and Zinc", Proc R Soc London, A115, 113-147, 1927.

HADAMARD, J
"Lecons sur la propagation des ondes et les equations de l'hydrodynamique", Librairie Scientifiqus A, Hermann, Paris, 1903.

HALLBAUER, D K, WAGNER, H and COOK, H G W
"Some Observations concerning the Microscopic and Mechanical Behaviour of Quartzite Specimens in stiff, triaxial compression tests", Int J Rock Mech Min Sci, 10, 713-726, 1973.

HEGEMIER, G A and READ, H E
"On some outstanding issues pertaining to the nonlinear static and dynamic response of Rock and Concrete", General lecture presented at the workshop on inelastic deformation amd failure modes, Northwestern University, Evanston, Illinois, 1984.

HILL, R
"Acceleration Waves in Solids", J Mech Phys Solids, 10, 1-16, 1962.

JANSON, J and HULT, J
"Fracture Mechanics and Damage Mechanics, a combined approach", J de Mecanique applique, 1, 69-84, 1977.

KOTSOVOS, M O
"Effects of Testing Techniques on the Post-Ultimate Behaviour of Concrete in Compression", Materials and Structures, RILEM, 16, No.91, 3-12, 1983.

KRAJCINOVIC, D and FONSEKA, G U
"The Continuous Damage Theory of Brittle Materials", Parts I and II, J Appl Mech, 48, 809-824, 1981.

KUPFER, H, HILLSDORF, H K and RUSCH, H
"Behaviour of Concrete under Biaxial Stresses", J ACI, 66, No.8, 656-666, 1969.

KUPFER, H and GERSTLE, K H
"Behaviour of Concrete under Biaxial Stresses", J Eng Mech Div, ASCE, 99, (EM4), 853, 1973.

LEMAITRE, J
"Coupled Elasto-plasticity and Damage Constitutive Equations", Computer Methods in Appl Mech and Eng, 51, 31-49, 1985.

LOLAND, K E
"Continuous Damage Model for Load-Response Estimation of Concrete", Cement and Concrete Research, 10, 395-402, 1980.

MAZARS, J and LEMAITRE, J
"Application of Continuous Damage Mechanics to Strain and Fracture Behaviour of Concrete", in Application of Fracture Mechanics to Continuous Composites. S Shad ed., USA, 375-388, 1984.

NEEDLEMAN, A and RICE, J R
"Limits to Ductility Set by Plastic Flow Localization", in Mechanics of Sheet Metal Forming, D P Koistinen and N M Wang eds., Plenum, New York, 237, 1978.

NEEDLEMAN, A and TVERGAARD, V
"Finite Element Analysis of Localization in Plasticity" in Finite Elements - special problems in solid mechanics, Oden J T and Carey G F eds., 5, 95-267, 1982.

NELISSEN, L J M
"Biaxial Testing of Normal Concrete", Heron, 18, No.1, 1-90, 1972.

NOSTRUM
"A Finite Element Program for Nonlinear Structural Mechanics", Applied Mechanics Research Unit, Technical Report No.18B, University of Cape Town, 1983.

ORTIZ, M
"A Constitutive Theory for the Inelastic Behaviour of Concrete", Mech of Material, 4, No.1, 67-93, 1985.

ORTIZ, M
"An Analytical Study of the Localized Failure Modes of Concrete", J Eng Mech ASCE (to appear) 1986.

ORTIZ, M
"An Overview of Localization Phenomena in Inelastic Solids", Lecture delivered at the University of Cape Town, January 1987.

ORTIZ, M, LEROY, Y and NEEDLEMAN, A
"A Finite Element Method for Localized Failure Analysis", Div of Eng, Brown University, 1986.

PEIRCE, D, ASARO, R J and NEEDLEMAN, A
"An Analysis of Nonuniform and Localized Deformation in Ductile Single Crystals", ACTA Metall, 1981.

READ, H E and HEGEMIER, G A
"Strain Softening of Rock, Soil and Concrete - a review article", Mech of Mat, 3, 271-296, 1984.

RESENDE, L
"A damage mechanics constitutive theory for the inelastic behaviour of concrete", Applied Mechanics Research Unit, Tech Rep No. 64, University of Cape Town, 1985.

RESENDE, L
"Applications of damage constitutive model to the solution of problems in rock mechanics", AMRU Tech Rep No. 70, University of Cape Town, 1986.

RESENDE, L
"Numerical Studies of Brittle Failure using a Damage Mechanics Approach", First World Congress on Computational Mechanics, Austin, Texas, September 1986.

RESENDE, L
"A Damage Mechanics Constitutive Theory for the Inelastic Behaviour of Concrete", Comp Meth Appl Mech Eng, 60, 57-93, 1987.

RESENDE, L and MARTIN, J B
"A Progressive Damage Continuum Model for Granular Materials", Comp Meth Appl Mech Eng, 42, 1-18, 1984.

RESENDE, L and MARTIN, J B
"Damage Constitutive Model for Geotechnical Applications" in Numerical Methods for Transient and Coupled Problems, R W Lewis, E Hinton, P Bettess and B A Schrefler eds., Pineridge Press, 475-496, 1984.

RESENDE, L and MARTIN, J B
"Formulation of Drucker-Prager Cap Model", J Eng Mech ASCE, 111, No.7, 855-881, 1985.

RESENDE, L and MARTIN, J B
"Parameter Identification in a Damage Model for Rock Mechanics", Int J Num Anal Meth Geomech (to appear) 1987.

RICE, J R
"The Localization of Plastic Deformation" in Koiter W Z (ed) Theoretical and Applied Mechanics, North Holland, 207-220, 1976.

RUDNICKI, J W and RICE, J R
"Conditions for the Localization of Deformation in Pressure-sensitive Dilatant Materials", J Mech Phys Solids, 23, 371-394, 1975.

SPOONER, D C and DOUGILL, J W
"A Quantitative Assessment of Damage Sustained in Concrete during Compressive Loading", Cement: Concrete Association, Magazine of Concrete Research, 27, No.92, 154-160, 1975.

STAVROPOULOU, V
"Constitutive Laws for Brittle Rocks", PhD thesis, University of the Witwatersrand, Johannesburg, 1982.

STURE, S and KO, H Y
"Strain Softening of Brittle Geologic Materials", J Num Anal Meth in Geomech, 2, 237-253, 1978.

THOMAS, T H
"Plastic Flow and Fracture in Solids", Academic Press, New York, 1961.

TVERGAARD, V, NEEDLEMAN, A and LO, K K
"Flow Localization in the Plain Strain Tensile Test", J Mech Phys Solids, 29, 115-142, 1981.

VAN MIER, J G M
"Strain-softening of Concrete under Multiaxial Loading Conditions" PhD thesis, De Technisch Hoegschool, Eindhoven, 1984.

VAN MIER, J G M
"Fracture of Concrete under Complex Stress", Heron, 31, No.3, 1-90, 1986.

VARDOULAKIS, I, GOLDSCHEIDER, M and GUDEHUS, G
"Formation of Shear Bands in Sand Bodies as a Bifurcation Problem", Int J N A M Geomech, 2, 99-128, 1978.

VARDOULAKIS, I
"Shear Band Inclination and Shear Modulus of Sand in Biaxial Tests", Int J N A M Geomech., 4, 103-119, 1980.

WILLAM, K J
"Experimental and Computational Aspects of Concrete Fracture", Proc Int Conf Computer Aided Analysis and Design of Concrete Structures, F Damjanic *et al* eds., Pineridge Press, Swansea, Part I, 33-70, 1984.

WILLAM, K J, BICANIC N and STURE, S
"Constitutive and Computational Aspects of Strain Softening and Localization in Solids" in Constitutive equations: Macro and Computational Aspects, K J Willam ed., Winter Annual Meeting, ASME, 1984.

APPENDIX A

Courses completed in partial fulfilment of the

M.Sc. Degree

Course		Date	Credits
CIV 540F	Finite Element Analysis	1986	4
CIV 504S	Structural Dynamics	1986	3
CIV 507B	Introduction to the Theory of Elasticity	1986	2
CIV 508S	Plates and Shells	1986	2
AMA 363F	Numerical Analysis	1986	3
AMA 367F	Continuum Mechanics	1986	3
AMA 368S	Numerical Solution to Differential Equations	1986	3
		TOTAL	20

Course Credits : 20

Thesis Credits : 20

TOTAL 40

Total credit requirements for the M.Sc. (Eng.) Degree : 40

COURSE DESCRIPTIONS

CIV 540F FINITE ELEMENT ANALYSIS

Generalised displacement method of analysis. Elastic energy theorems leading to basic procedures of the finite element method. Approximation and interpolation of functions. Isoparametric formulation of elements. 2-D and 3-D elements of structural mechanics. Equation solving in the computer and the structure of the finite element packages for practical applications. Some advanced topics in finite element analysis.

CIV504S STRUCTURAL DYNAMICS

Numerical procedures in dynamics including time stepping techniques for transient response and iterative methods for computation of eigen values and eigen vectors. Formulation of the equations of motion in the finite element framework. Applications of vibration theory to the analysis of earthquake and wind loaded structures.

CIV 507B INTRODUCTION TO THE THEORY OF ELASTICITY

Stress, strain, equilibrium, strain displacement relations. Elastic constants. Solutions of simple boundary value problems in plane stress and plane strain.

CIV 504S PLATES AND SHELLS

An introduction to the elastic theory of plates and shells. Differential equations of equilibrium. Variational methods in mechanics leading to the Ritz procedure and an introduction to the finite element method. Finite elements for plates and shells.

AMA 363F NUMERICAL ANALYSIS

Selected topics in numerical analysis are covered, with applications to modelling. Numerical methods for the solution of ordinary differential equations; approximation to functions; and eigenvalue methods are covered.

AMA 367F CONTINUUM MECHANICS

Tensor algebra is introduced, with applications to fluid mechanics and elasticity, including basic continuum mechanics; fluid and solid mechanics; Navier-Stokes equations; and partial differential equations of elasticity.

AMA 368S NUMERICAL SOLUTION OF DIFFERENTIAL EQUATIONS

Commonly used methods for solving partial differentiation equations numerically are introduced, including the collocation method; weighted residual methods; the Galerkin method; the finite element method; and finite difference methods.